Computational Modeling of Dynamic Electron Paramagnetic Resonance Spectra

Jeremy Lehner

A dissertation
submitted in partial fulfillment of the
requirements for the degree of

Doctor of Philosophy

University of Washington

2019

Reading Committee:

Stefan Stoll, Chair

Xiaosong Li

David Masiello

Cody Schlenker

Program Authorized to Offer Degree:
Chemistry

University of Washington

Abstract

Computational Modeling of Dynamic Electron Paramagnetic Resonance Spectra

Jeremy Lehner

Chair of the Supervisory Committee:
Associate Professor Stefan Stoll
Chemistry

A comprehensive method is laid out for the solution of the stochastic Liouville equation to simulate spectral lineshapes for continuous-wave EPR spectra. The method is presented in a general fashion so that the same implementation can be used to simulate general spin systems with any number and type of spin Hamiltonian interaction terms. A modification of the frequency-dependent spectral lineshape function to a field-dependent lineshape function is also presented for simulations of systems in which the field-sweep experiment must be accounted for explicitly. Simulations are presented for a $S = 1/2$ nitronyl nitroxide system with multiple magnetic nuclei and for a $S = 7/2$ gadolinium(III) system using the general solver over a range of rotational correlation times. CW EPR spectra are also measured for $S = 1/2$ copper(II)-EGTA over a range of temperatures to show the importance of performing explicit field sweep simulations in the slow-motion regime for spin systems with highly anisotropic g-tensors.

TABLE OF CONTENTS

ACKNOWLEDGMENTS

I would like to acknowledge everyone who supported me in this endeavor. First and foremost, I thank Dr. Stefan Stoll for his endless support, engagement, and patience. Thank you to all of the Stoll group members, past and present, who have provided invaluable input and camaraderie, in particular Dr. Ellen Hayes, Dr. Thomas Edwards, Dr. Eric Evans, Dr. Hannah DeBerg, Dr. Claudia Tait, Dr. Joscha Nehrkorn, Donald Mannikko, Lizzy Canarie, Sam Jahn, Sarah Sweger, and Saralyn Ogden. Thank you as well to the professors in the theoretical-chemistry division for helping me begin my graduate journey, in particular Dr. Xiaosong Li, Dr. David Masiello, and Dr. Lutz Maibaum, as well as their graduate students and postdocs. I would also like to acknowledge the Department of Chemistry administrative and support staff, all of whom work to make the department run smoothly and help to create a positive and vibrant department culture. Finally, I thank my committee members Dr. Kai-Mei Fu, Dr. Cody Schlenker, Dr. Xiaosong Li, and Dr. David Masiello for their time, attention, and guidance. And to all of my friends and family, thank you for all of your love and support in this endeavor and in all aspects of my life.

DEDICATION

To a better future – Kaito and Hinata.

Chapter 1

PRINCIPLES OF ELECTRON PARAMAGNETIC RESONANCE

1.1 Energy of the electron magnetic moment in an external magnetic field

Electrons, by virtue of their existence, have intrinsic angular momentum, which is called spin. The property of spin causes electrons to have a permanent magnetic dipole moment $\boldsymbol{\mu}$. In the absence of an external magnetic field, the energy of this magnetic moment has no orientational dependence. However, in the presence of an external magnetic field $\boldsymbol{B}$, the energy E of a magnetic dipole moment is

$$E = -\boldsymbol{\mu} \cdot \boldsymbol{B} = -\mu B \cos\theta \tag{1.1}$$

where μ and B are the magnitudes of $\boldsymbol{\mu}$ and $\boldsymbol{B}$, and θ is the angle between the direction of $\boldsymbol{\mu}$ and the direction of $\boldsymbol{B}$. According to equation 1.1, the energy is minimum when the magnetic moment is aligned parallel to the magnetic field ($\theta = 0°$) and the energy is maximum when the magnetic moment is aligned antiparallel to the magnetic field ($\theta = 180°$). This orientational energy difference of the magnetic moment in the presence of a magnetic field is the fundamental physical interaction that is probed in magnetic resonance spectroscopy.

Electron paramagnetic resonance (EPR), discovered in 1944, is the subfield of magnetic resonance that probes electronic spin state transitions [1, 2]. EPR experiments are used to obtain information about molecular structure and dynamics in a variety of fields [3] including medicine [4, 5], materials science [6, 7, 8], and quantum computing [9, 10, 11].

Considering the elementary charge e and the mass of an electron m_e, the magnetic moment of an electron is

$$\boldsymbol{\mu} = g_\mathrm{e} \frac{-e}{2m_\mathrm{e}} \boldsymbol{J} = -\frac{g_\mathrm{e}\mu_\mathrm{B}}{\hbar} \boldsymbol{J} \tag{1.2}$$

where $\mu_\mathrm{B} = e\hbar/2m_\mathrm{e}$ is the Bohr magneton, g_e is the free-electron g-factor required to correct the classical magnetic moment, and $\boldsymbol{J}$ is the total angular momentum of the electron, which includes both its orbital angular momentum $\boldsymbol{L}$ and its spin angular momentum $\boldsymbol{S}$. The

g-factor for a free electron that has no orbital angular momentum or interactions with any other fields or particles is $g_\mathrm{e} = 2.00231930436182(52)$ [12].

In EPR spectroscopy, we are primarily concerned with the spin angular momentum $\boldsymbol{S}$ and transitions between spin states of molecules in the electronic ground state. In such a case, the orientation of the electronic spin angular momentum changes upon absorption but the orbital angular momentum does not. Therefore, the electron magnetic moment can be expressed as

$$\boldsymbol{\mu} = -\frac{g_\mathrm{e}\mu_\mathrm{B}}{\hbar}\boldsymbol{S}. \tag{1.3}$$

According to equation 1.3, and considering $g_\mathrm{e} > 0$, the magnetic moment of the electron points in the opposite direction of the spin angular momentum. Therefore, the energy in equation 1.1 is minimum when $\boldsymbol{S}$ is aligned antiparallel to the magnetic field and the energy is maximum when $\boldsymbol{S}$ is aligned parallel to the field.

In real molecules, electrons almost always have some orbital angular momentum that couples with the spin angular momentum, through spin–orbit coupling. If the spin–orbit coupling is weak, then the effect of the spin–orbit coupling on the electron magnetic moment can be accounted for by using an effective g-factor in equation 1.3 that deviates from g_e. Greater spin–orbit coupling results in larger deviations from the free-electron g-value. Using the effective g-value, equation 1.3 becomes

$$\boldsymbol{\mu} = -\frac{g\mu_\mathrm{B}}{\hbar}\boldsymbol{S}. \tag{1.4}$$

Using equations 1.1 and 1.4, the energy of an electron magnetic moment in an external magnetic field can be expressed as

$$E = -\boldsymbol{\mu}\cdot\boldsymbol{B} = \frac{g\mu_\mathrm{B}}{\hbar}BS\cos\theta \tag{1.5}$$

where S is the magnitude of the spin angular momentum. However, the peculiarity of quantum mechanics allows us to know simultaneously only the magnitude of the spin angular momentum and its component along just one arbitrary spatial direction. The components of $\boldsymbol{S}$ in the plane perpendicular to the direction of the known component are uncertain. By convention, we label the direction that is parallel to the external magnetic field $\boldsymbol{B}$ as the z-axis and the component of $\boldsymbol{S}$ along z as S_z, which is the component of $\boldsymbol{S}$ along the external magnetic field. Therefore, in equation 1.5, $\cos\theta = S_z/S$ and the energy of the electron magnetic moment in a magnetic field is

$$E = -\boldsymbol{\mu} \cdot \boldsymbol{B} = \frac{g\mu_{\mathrm{B}}}{\hbar} B S_z. \tag{1.6}$$

1.2 Spin and spin states

The magnitude of the spin angular momentum $\boldsymbol{S}$ is

$$|\boldsymbol{S}| = S = \hbar\sqrt{s(s+1)} \tag{1.7}$$

where s is the maximum possible projection of $\boldsymbol{S}$ along $\boldsymbol{B}$. All electrons have $s = 1/2$ and therefore the magnitude of the spin angular momentum of a single electron is $S = \hbar\sqrt{3}/2$. The quantum nature of spin allows the projection of $\boldsymbol{S}$ along $\boldsymbol{B}$, denoted by $\hbar m_S$, to assume values of m_S only within the range of $-s$ to s in integer increments. The projection m_S is referred to as the spin state. A single electron can be in any superposition of the $+1/2$ and $-1/2$ spin states, but upon measurement can be found to be in only one of either the $+1/2$ or $-1/2$ spin states. The $+1/2$ spin state is also called the α state and the $-1/2$ spin state is called the β state. If two electrons are paired in the same spatial orbital, then one must be in the α state while the other one must be in the β state, in which case their magnetic moments cancel exactly and there is zero net spin angular momentum.

Regrettably, the conventional language and notation in the field of EPR can sometimes be ambiguous or misleading, as is the case when discussing electron spin. The convention in EPR is to refer to electrons as "spin-1/2" particles. However, this does not mean that the magnitude of the spin angular momentum S is $\hbar/2$ nor does it mean that the projection of $\boldsymbol{S}$ along $\boldsymbol{B}$ is always $\hbar/2$. In the literature, the spin of a system is usually denoted by S rather than s, but this should not be confused with the magnitude of the spin angular momentum $|\boldsymbol{S}|$. For example, a molecule with a single unpaired electron is usually described as a $S = 1/2$ system, which can be in either the α or β state and which has a constant magnitude of spin angular momentum of $\hbar\sqrt{3}/2$ regardless of its spin state. In general, molecules with multiple unpaired electrons are referred to as $S = n/2$ systems in their high-spin states, where n is the number of unpaired electrons. For example, a molecule that has two unpaired electrons and is in the triplet state is called a $S = 1$ or "spin-1" system.

1.3 Spin operator formalism

In quantum mechanics, physical observables of a system such as the energy, the magnetic moment, or the angular momentum, are represented by mathematical operators. The energy operator is the Hamiltonian $\hat{H}$, which is a scalar operator. The magnetic moment $\hat{\boldsymbol{\mu}}$ and spin angular momentum $\hat{\boldsymbol{S}}$ are vector operators and have the form $\hat{\boldsymbol{\mu}} = [\hat{\mu}_x\ \hat{\mu}_y\ \hat{\mu}_z]^{\mathrm{T}}$ and $\hat{\boldsymbol{S}} = \left[\hat{S}_x\ \hat{S}_y\ \hat{S}_z\right]^{\mathrm{T}}$ respectively. In this operator formalism, the energy of the magnetic moment in equation 1.6 is represented by the Hamiltonian operator

$$\hat{H} = \frac{g\mu_{\mathrm{B}}B}{\hbar}\hat{S}_z. \tag{1.8}$$

The state of a quantum system is represented by a function. The state functions can be chosen to be eigenfunctions of the operator that corresponds to the physical observable we wish to calculate so that, when operated on, we obtain the value of that observable. In EPR, we are concerned with transitions between electronic spin states, which are the states with different values of m_S that are allowed for a given total spin S. For a single electron, we may use Dirac bra-ket notation to represent these states as $|{+1/2}\rangle$ or $|\alpha\rangle$, which we call the spin-up state, and $|{-1/2}\rangle$ or $|\beta\rangle$, which we call the spin-down state. These states are simultaneously eigenfunctions of $\hat{\boldsymbol{S}}^2$ and $\hat{S}_z$, where $\hat{\boldsymbol{S}}^2$ is

$$\hat{\boldsymbol{S}}^2 = \hat{\boldsymbol{S}} \cdot \hat{\boldsymbol{S}} = \hat{S}_x^2 + \hat{S}_y^2 + \hat{S}_z^2 \tag{1.9}$$

which is the scalar product of the spin angular momentum with itself. For a general spin S in spin state m_S, operating with $\hat{\boldsymbol{S}}^2$ and $\hat{S}_z$ gives

$$\begin{aligned} \hat{\boldsymbol{S}}^2 |S, m_S\rangle &= \hbar^2 S(S+1) |S, m_S\rangle \\ \hat{S}_z |S, m_S\rangle &= \hbar m_S |S, m_S\rangle \end{aligned} \tag{1.10}$$

where the notation $|S, m_S\rangle$ denotes a state via the total spin quantum number S and the projection quantum number m_S. We see from equation 1.10 that the physical observable corresponding to $\hat{\boldsymbol{S}}^2$ is the square of the magnitude of the spin angular momentum, which is determined by the total spin S. The observable corresponding to $\hat{S}_z$ is the projection of $\hat{\boldsymbol{S}}$ onto $\boldsymbol{B}$, which is determined by the projection number m_S.

Because the spin states are eigenfunctions of $\hat{S}_z$, they are also eigenfunctions of the Hamiltonian operator. The energy of a spin state is obtained as the expectation value of the Hamiltonian in equation 1.8:

$$\langle m_S| \hat{H} |m_S\rangle = \frac{g\mu_{\mathrm{B}}B}{\hbar} \langle m_S| \hat{S}_z |m_S\rangle = \frac{g\mu_{\mathrm{B}}B\hbar m_S}{\hbar} \langle m_S|m_S\rangle = g\mu_{\mathrm{B}}Bm_S. \tag{1.11}$$

In the case of a single electron the energies of the spin-up and spin-down states are

$$\begin{aligned} \langle\alpha|\,\hat{H}\,|\alpha\rangle &= +\frac{g\mu_{\mathrm{B}}B}{2} \\ \langle\beta|\,\hat{H}\,|\beta\rangle &= -\frac{g\mu_{\mathrm{B}}B}{2}. \end{aligned} \tag{1.12}$$

1.4 The spin Hamiltonian

In EPR spectroscopy, the observed experimental spectra are due to transitions between spin states. The energies of these states, and therefore the lineshapes of the measured spectra, are modeled using the spin Hamiltonian. The spin Hamiltonian is an effective Hamiltonian, in that it includes explicitly only those physical interactions that contribute to the separation of the spin state energies observable in the EPR experiment [13, 14]. All other physical interactions are either included in an effective approximate manner or neglected entirely. For example, the full Hamiltonian for a molecule would include potential-energy terms for Coulombic interactions between all electrons and nuclei, kinetic-energy terms for electronic motion and nuclear vibrations and rotations, and many others [15]. Such interactions contribute to the overall energy of the molecule, but do not affect the relative energies of the spin states and so are not considered in the spin Hamiltonian. Even some interactions that do affect the separation of spin state energies are not included in the spin Hamiltonian explicitly. Rather, these interactions are often included in an effective manner. For example, the coupling of spin angular momentum and orbital angular momentum (i.e. spin–orbit coupling) is accounted for by using an effective g-factor rather than g_{e}, as discussed previously in this chapter.

The types of interactions that are typically included in the spin Hamiltonian are those between the external magnetic field B_0 and electronic or nuclear magnetic moments (Zeeman interactions), between electronic magnetic moments and nuclear magnetic moments (hyperfine interaction), between electron magnetic moments (zero-field splitting and exchange interactions), and between the nuclei and an electric field (nuclear quadrupole interaction). Each of these interactions will be discussed below. For more detail, there are a number of introductory and advanced texts available that offer a fuller treatment of spin Hamiltonian interactions and other basic principles of magnetic resonance [13, 14].

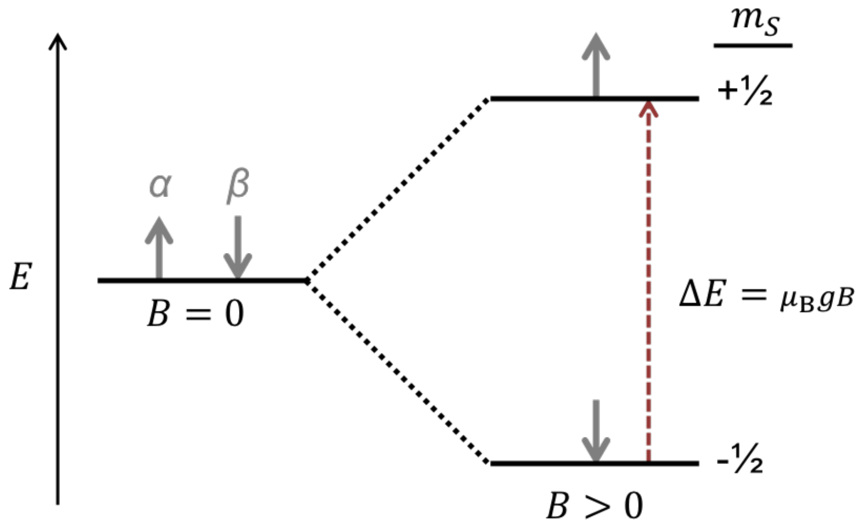

Figure 1.1: Energy level diagram of the electron Zeeman interaction for a single orientation of a $S = 1/2$ system in an external magnetic field B. The red arrow signifies an allowed spin state transition from the $|-1/2\rangle$ state to the $|+1/2\rangle$ state.

1.4.1 The Zeeman interaction

The Zeeman interaction, or Zeeman splitting, is the interaction of a spin magnetic moment with an external magnetic field. If the spin magnetic moment is that of an electron, then the interaction is called the electron Zeeman interaction and is represented by the following spin Hamiltonian term:

$$\hbar \hat{H}_{\mathrm{ez}} = \mu_{\mathrm{B}} \boldsymbol{B} \cdot g \cdot \hat{\boldsymbol{S}} \tag{1.13}$$

where the Hamiltonian $\hat{H}_{\mathrm{ez}}$ is in angular frequency units, which is the usual convention for the spin Hamiltonian in EPR. In equation 1.13, g is the g-tensor rather than the g-factor. The g-tensor is 3×3 Cartesian tensor with elements that define the g-factor for any possible orientation of the molecule within the external field. Therefore, in general, equation 1.13 has the form

$$\hbar \hat{H}_{\mathrm{ez}} = \mu_{\mathrm{B}} \begin{bmatrix} B_x & B_y & B_z \end{bmatrix}^{\mathrm{T}} \begin{bmatrix} g_{xx} & g_{xy} & g_{xz} \\ g_{yx} & g_{yy} & g_{yz} \\ g_{zx} & g_{zy} & g_{zz} \end{bmatrix} \begin{bmatrix} \hat{S}_x \\ \hat{S}_y \\ \hat{S}_z \end{bmatrix} . \tag{1.14}$$

The particular values of the vector and matrix elements in equation 1.14 depend on the coordinate system in which they are defined as well as on the physical properties of the molecule and the external magnetic field. An energy level diagram of Zeeman splitting for a $S = 1/2$ system is shown in figure 1.1.

Likewise, interaction of an external magnetic field with a nuclear spin magnetic moment is called the nuclear Zeeman interaction, which has the following spin Hamiltonian term:

$$\hbar \hat{H}_{\mathrm{nz}} = \mu_{\mathrm{n}} g_{\mathrm{n}} \boldsymbol{B} \cdot \hat{\boldsymbol{S}} \tag{1.15}$$

where μ_{n} is the nuclear magneton and g_{n} is the nuclear g-factor, which depends on the particular nucleus. The nuclear g-factor can usually be well-approximated as a scalar value rather than a Cartesian tensor because the interaction of the nuclear magnetic moment with the external field is essentially isotropic (orientation-independent).

The Zeeman interaction is the fundamental physical phenomenon in all magnetic resonance spectroscopy. In an external magnetic field, the electronic spin states have energies given by equation 1.6. EPR spectroscopy probes transitions between these electronic spin states. Therefore, the energy of an absorbed photon that induces this transition is

$$E_{\mathrm{photon}} = h\nu = E_{\alpha} - E_{\beta} = \frac{+\mu_{\mathrm{B}} g B}{2} - \frac{-\mu_{\mathrm{B}} g B}{2} = \mu_{\mathrm{B}} g B \tag{1.16}$$

where g in equation 1.16 is a single g-value that corresponds to whatever orientation the molecule has in the external field upon photon absorption. In the presence of an external field, all EPR spectra of paramagnetic compounds exhibit the splitting of spin state energies due to the electron Zeeman interaction. For a $S = 1/2$ system specifically, the Zeeman interaction produces a spectrum with a single peak.

1.4.2 The hyperfine interaction

The hyperfine interaction, or hyperfine splitting, is due to the interaction between electron and nuclear magnetic moments, and therefore occurs in paramagnetic systems that contain nuclear spins. The simplest example of this type of system is the hydrogen atom, with electron spin $S = 1/2$ and nuclear spin $I = 1/2$. An energy level diagram for this type of system is shown in figure 1.2. The spin Hamiltonian term for the hyperfine interaction is

$$\hbar \hat{H}_{\mathrm{hf}} = \hat{\boldsymbol{S}} \cdot A \cdot \hat{\boldsymbol{I}} \tag{1.17}$$

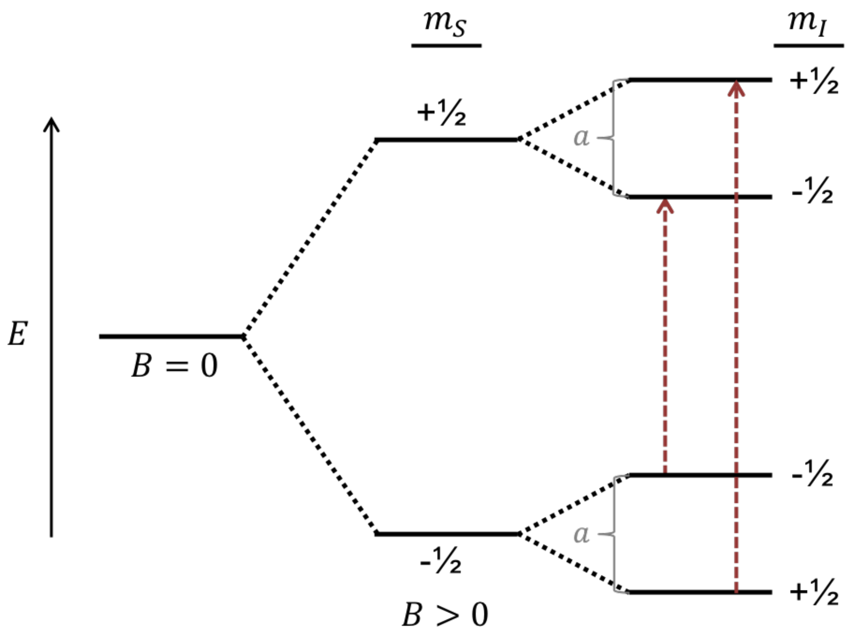

Figure 1.2: Energy level diagram for a single orientation of a $S = 1/2$ and $I = 1/2$ system with $A > 0$ in an external magnetic field B. The nuclear Zeeman interaction is neglected. The energy splittings labeled as a are the splittings due to the hyperfine interaction. The red arrows signify the allowed spin state transitions for which $\Delta m_S = \pm 1$ and $\Delta m_I = 0$.

where $\hat{\boldsymbol{I}} = [\hat{I}_x \;\; \hat{I}_y \;\; \hat{I}_z]^{\mathrm{T}}$ is the nuclear spin vector operator. As in equation 1.13, A in equation 1.17 is a 3×3 Cartesian tensor that accounts for the possible orientation dependence of the hyperfine interaction. If the spin system contains multiple magnetic nuclei, then there is a hyperfine term in the spin Hamiltonian for each nuclear spin. For example, for a system with N nuclear spins, the hyperfine component of the spin Hamiltonian is

$$\hbar \hat{H}_{\mathrm{hf}} = \hat{\boldsymbol{S}} \cdot \sum_{i=1}^{N_{\mathrm{nuc}}} A_i \cdot \hat{\boldsymbol{I}}_i \tag{1.18}$$

where each nuclear spin has its own A-tensor A_i and its own spin vector operator $\hat{\boldsymbol{I}}_i$.

The hyperfine interaction consists of two components: a dipolar component and a Fermi contact component. The dipolar component is a through-space anisotropic (orientation-dependent) interaction in which the electron magnetic moment interacts with the magnetic field due to the nuclear magnetic moment. The Fermi contact component is present when there is an unpaired electron that has nonzero electron density at the magnetic nucleus.

Because the nuclear volume is so small, the electron density is homogeneous over the entire nuclear volume. Therefore, the Fermi contact component of the hyperfine interaction is always isotropic.

The effect of the hyperfine interaction on an EPR spectrum is to split the Zeeman peaks into additional peaks separated in energy by the strength of the hyperfine coupling. The number of additional hyperfine peaks is determined by the spin of the magnetic nucleus. For example, the spin system ($S = 1/2$, $I = 1/2$) in figure 1.2 has two allowed EPR transitions ($\Delta m_S = \pm 1$, $\Delta m_I = 0$) with energies

$$\begin{aligned} E &= \mu_{\mathrm{B}} g B - a \\ E &= \mu_{\mathrm{B}} g B + a \end{aligned} \tag{1.19}$$

where a is the energy level splitting due to the hyperfine interaction as portrayed in figure 1.2. In general, for a nuclear spin $I = n/2$ each Zeeman peak is split into $n + 1$ peaks due to the hyperfine interaction.

1.4.3 Zero-field splitting

Zero-field splitting occurs in systems with multiple unpaired electrons ($S > 1/2$), also called high-spin systems. This interaction is termed "zero-field" because it causes the spin state energies to be lifted in degeneracy even in the absence of an external magnetic field. Rather, the field that breaks the spin state degeneracy is internal to the molecule itself and is the result of through-space dipolar spin-spin coupling and spin–orbit coupling between the unpaired electrons. The spin Hamiltonian term for zero-field splitting is

$$\hbar \hat{H}_{\mathrm{zfs}} = \hat{\boldsymbol{S}} \cdot D \cdot \hat{\boldsymbol{S}} \tag{1.20}$$

where D is the zero-field splitting tensor, which is a 3×3 Cartesian traceless dipolar tensor. In the frame in which D is diagonal, it has the form

$$D = \begin{bmatrix} D_x & 0 & 0 \\ 0 & D_y & 0 \\ 0 & 0 & D_z \end{bmatrix} = \begin{bmatrix} -\frac{D}{3} + E & 0 & 0 \\ 0 & -\frac{D}{3} - E & 0 \\ 0 & 0 & \frac{2D}{3} \end{bmatrix} \tag{1.21}$$

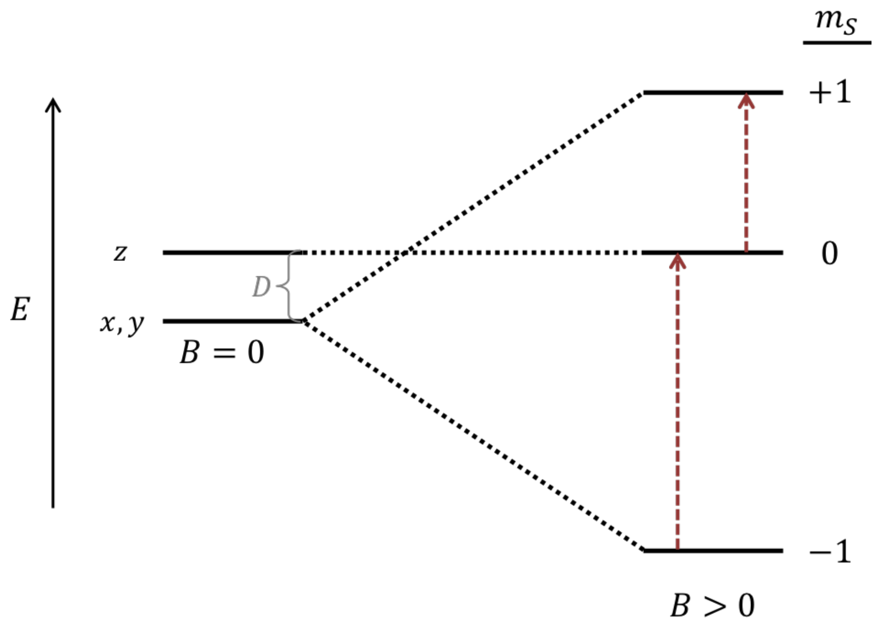

Figure 1.3: Energy level diagram for a single orientation of a triplet ($S = 1$) system with axial zero-field splitting D. When $B = 0$, the spin energies are not all degenerate due to the zero-field splitting. When $B > 0$, there are two allowed transitions of different energy. This diagram only shows energy levels at zero-field and high field.

where the zero-field splitting parameters D (axial) and E (rhombic) are defined by

$$D = \frac{3D_z}{2} \tag{1.22}$$

$$E = \frac{D_x - D_y}{2}.$$

Unfortunately, the convention for zero-field splitting in EPR is to use the symbol D to denote both the 3×3 Cartesian zero-field splitting tensor *and* the axial zero-field splitting parameter that appears on the diagonal of the matrix in equation 1.21. Usually, it is clear from context to which entity the symbol D is referring, but if there is the possibility of ambiguity then it will be the convention of this text to state the nature of D explicitly.

Note that the zero-field splitting interaction does not have an isotropic part as defined by the traceless tensor in equation 1.21. The isotropic component of the zero-field interaction in not conventionally included in the spin Hamiltonian because it shifts all the spin states by the same energy, which has no effect on the relative energies of the states. A molecule in which the unpaired electrons are distributed with perfect spherical symmetry would therefore not exhibit any zero-field splitting even though the spin states will be shifted in energy. A molecule with perfect axial symmetry, where $D_x = D_y$ and $E = 0$, would exhibit zero-field splitting like that illustrated in figure 1.3. As the molecular geometry deviates from axial ($D_x \neq D_y$), the zero-field splitting increases in rhombicity ($|E| > 0$).

In the absence of zero-field splitting, the EPR spectrum of a triplet like that in figure 1.3 would consist of a single peak, as both transitions ($|-1\rangle \leftrightarrow |0\rangle$ and $|0\rangle \leftrightarrow |+1\rangle$) would be the same energy, which is simply the energy level splitting due to the electron Zeeman interaction. However, due to axial zero-field splitting, the frequency-swept triplet spectrum will instead consist of two peaks with transition energies

$$\begin{aligned} E &= \mu_{\mathrm{B}} g B - D \qquad (1.23) \\ E &= \mu_{\mathrm{B}} g B + D \end{aligned}$$

where D is the energy level splitting in the absence of any external field, as portrayed in figure 1.3.

1.4.4 Other spin Hamiltonian interactions

The work to be presented in the later chapters of this text only includes systems in which the Zeeman, hyperfine, and/or zero-field splitting interactions are significant to the continuous wave (CW) EPR lineshape. However, there are other spin Hamiltonian interactions that may be relevant for certain systems under certain experimental conditions, such as the exchange interaction and the nuclear Zeeman and quadrupole interactions, which are discussed in detail in numerous EPR texts [13, 14, 16]. Briefly, the exchange interaction is an electron-electron interaction between different unpaired electron spins whereas the nuclear quadrupole interaction is a nuclear spin phenomenon due to the interaction of nuclei that have nonspherical charge distributions (i.e. $|I| > 1/2$) with the electric fields that are produced by electrons. Both of these spin Hamiltonian terms, as well as any other term, can be represented as a scalar product of two spin vector operators and a 3×3 Cartesian interaction tensor, just as in the spin Hamiltonian terms discussed above.

Chapter 2

THEORY OF EPR IN THE SLOW-MOTION REGIME

Continuous-wave (CW) experiments are ubiquitous in electron paramagnetic resonance (EPR) spectroscopy. CW EPR spectra can yield important information, such as spin Hamiltonian parameters, spin quantification, or dynamic properties. The CW EPR lineshape is highly sensitive to the spin rotational dynamics if the spin Hamiltonian has anisotropic interactions.

The rotational dynamics of a paramagnetic molecule in solution can be characterized by τ_c, the rotational correlation time, the details of which will be explained in this chapter. It is convenient to categorize rotational motion into regimes based on the rate of rotation relative to the spectral width $\Delta\omega$ of the spin system. In this case, there are four important motional regimes or limits. In the rigid limit, the EPR sample is a powder or frozen solution and there is essentially no rotational motion, so τ_c is very long and the lineshape is a weighted average of signals from all static orientations of the molecule. The other motional extreme is the isotropic limit in which rotational dynamics is so fast (τ_c very short) that any anisotropic interactions average out and the observed lineshape corresponds to a single isotropic signal. Between these two limits, lineshapes can be categorized in either the fast-motion or slow-motion regimes. In both cases, the rotational motion couples to the spin state energy levels, causing time-dependent modulations in the spin state energies, which manifest as changes in the observed CW EPR lineshape. In the fast-motion regime, the rotational coupling can be accounted for by using a computationally inexpensive perturbational approach, such as Redfield theory [17]. However, in the slow-motion regime, where τ_c^{-1} is on the order of the spectral width $\Delta\omega$, the rotational motion is coupled strongly to the spin state energies and therefore must be modelled explicitly. An example of the effect of rotational motion on the CW EPR lineshape for a $S = 1/2$ nitroxide spin system with hyperfine coupling to one nitrogen-14 nucleus with nuclear spin $I = 1$ is shown in figure 2.1.

Many methods have been developed to address the problem of simulating slow-motion CW EPR lineshapes, the most prominent being trajectory methods and stochastic methods. The stochastic Liouville equation (SLE) is a general theory of relaxation due to processes such as rotational motion or chemical exchange that can be used to simulate CW EPR lineshapes in any motional limit or regime via solution of a particular lineshape function rather than direct

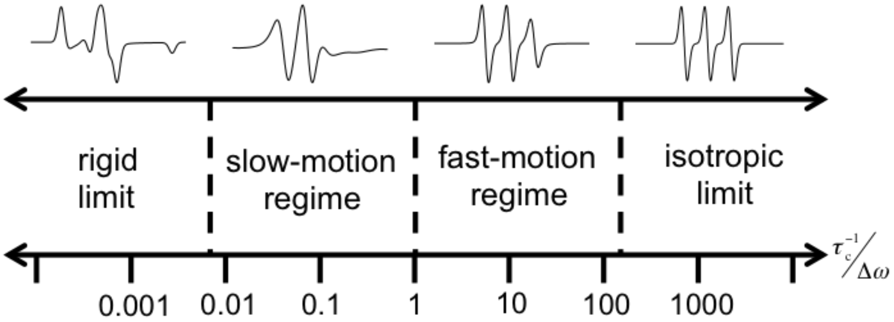

Figure 2.1: Simulated nitroxide spectra over a range of rotational correlation times τ_c. When the inverse of τ_c is on the same order as the spectral width $\Delta\omega$, then the spectrum enters the slow-motion regime and the spin state energies are coupled strongly to the rotational motion of the molecule. The spectral width is defined as the spread in resonance fields in the rigid limit spectrum.

solution of the Schrödinger equation [18, 19, 20, 21, 22]. This is the approach used in this work, the details of which will explained in this chapter. Trajectory methods such as molecular dynamics (MD) can also capture the effect of rotational dynamics across motional regimes by directly solving the time-dependent Schrödinger equation [23, 24]. While both methods can accurately simulate slow-motion EPR lineshapes, the SLE has been more widely used in magnetic resonance. The SLE has the advantage of significantly lower computational cost than MD simulations, and the SLE method does not require any knowledge about the actual structure of the paramagnetic species under study. Efficient numerical algorithms, such as the Lanczos algorithm with continued fraction expansion [25, 21], have also been developed to rapidly solve the SLE frequency-dependent lineshape function. In the implementation of the general SLE solver presented in this work, the Lanczos method is the default algorithm to calculate the CW EPR lineshape. The details of this method are discussed in appendix B.

When the SLE theory was first introduced for EPR, it was meant to address the problem of simulating CW EPR spectra for slow-tumbling nitroxides in solution [26, 20, 27]. The dominant spin Hamiltonian interactions in nitroxides include the electron Zeeman interaction for a single spin $S = 1/2$ and the hyperfine interaction with a single spin $I = 1$ nitrogen-14 nucleus. The expressions presented for the spin Hamiltonian elements were particular to nitroxides. Since the introduction of the SLE for EPR, the theory has been expanded to model spin systems other than nitroxides. For example, the program E-SpiRes can simulate systems with $S = 1/2$ and potentially any number of hyperfine interactions [28] and another program, Spinach, can solve the SLE for exceptionally large spin systems with various spin Hamiltonian interactions, given enough time and computational resources [29]. Simulation of slow-motion spectra for high-spin systems ($S > 1/2$) with zero-field splitting (ZFS) interaction have also been reported. For instance, slow-motion triplet spectra ($S = 1$) in the absence of hyperfine interactions have been simulated using a discrete jump approach [30, 31, 32] and the SLE has been used to simulate CW EPR linewidths for Gd(III) systems ($S = 7/2$) undergoing rotational and conformational dynamics [33]. However, to my current knowledge, an easy-to-use slow-motion simulation algorithm that could calculate the entire CW lineshape for any general spin system was not available before this work.

In this chapter, a general SLE solver is presented as implemented in the EasySpin software package [34] and the solution of the SLE for the simulation of CW EPR lineshapes is explicitly described. This general solver is novel in that it is general and applicable for any spin system with any number and type of spins and spin Hamiltonian interaction terms. (e.g. Zeeman interactions, hyperfine interactions, ZFS interactions, exchange interactions, etc.). Furthermore, the issue of calculating the SLE lineshape function for field-sweep experiments is addressed, which is the manner in which experimental CW EPR spectra are actually measured. Most SLE solvers actually output field-converted frequency-swept spectra in which the lineshape is simulated for a frequency-sweep experiment and then converted to a field sweep result. It is shown that this method is inappropriate for systems with highly anisotropic g-tensors. A method is presented to explicitly simulate field-swept spectra by converting the frequency-dependent SLE lineshape function into a field-dependent form.

2.1 Rotational diffusion

The problem of modeling the CW EPR lineshape of a spin system undergoing slow rotational motion essentially amounts to the problem of incorporating relaxation into the time-evolution of that spin system under a spin Hamiltonian that accounts for all of the relevant interactions. In this case, we are interested in relaxation due to the rotational motion of the paramagnetic molecules in an external magnetic field.

Consider an EPR sample that contains an ensemble of spin systems with some distribution of molecular orientations. The time evolution of this orientational distribution is given by the rotational Smoluchowski equation [35, 36]:

$$\frac{\partial}{\partial t}P(\boldsymbol{\Omega},t) = -\Gamma(\boldsymbol{\Omega})P(\boldsymbol{\Omega},t) \tag{2.1}$$

where $P(\boldsymbol{\Omega},t)$ is the time-dependent probability distribution of molecular orientations defined by a set of three Euler angles $\boldsymbol{\Omega} = [\alpha \;\; \beta \;\; \gamma]$, and $\mathit{\Gamma}(\boldsymbol{\Omega})$ is the rotational diffusion operator. Equation 2.1 describes classical Brownian rotational diffusion. The operator $\mathit{\Gamma}(\boldsymbol{\Omega})$ is a classical Markovian kinetic operator, meaning that it contains information about the probability of a molecule having orientation $\boldsymbol{\Omega}$ at time t given that it had some initial orientation at time zero. The rotational diffusion operator $\mathit{\Gamma}(\boldsymbol{\Omega})$ has the additional property [26, 20, 21]

$$\frac{\partial}{\partial t} P_{\mathrm{eq}}(\boldsymbol{\Omega}) = -\mathit{\Gamma}(\boldsymbol{\Omega}) P_{\mathrm{eq}}(\boldsymbol{\Omega}) = 0. \tag{2.2}$$

In equation 2.2, $P_{\mathrm{eq}}(\boldsymbol{\Omega})$ is the equilibrium orientational distribution, which is not time dependent. It has the form [20, 27]

$$P_{\mathrm{eq}}(\boldsymbol{\Omega}) = \frac{\mathrm{e}^{\frac{-U(\boldsymbol{\Omega})}{k_{\mathrm{B}}T}}}{\int \mathrm{d}\boldsymbol{\Omega}\, \mathrm{e}^{\frac{-U(\boldsymbol{\Omega})}{k_{\mathrm{B}}T}}} \tag{2.3}$$

where $U(\boldsymbol{\Omega})$ is the orienting potential, which, if present, describes any interactions that cause the system to have a preferred orientation or hindered rotational mobility.

Equation 2.2 means that operation by $\mathit{\Gamma}(\boldsymbol{\Omega})$ on $P(\boldsymbol{\Omega}, t)$ always moves the orientational distribution toward its equilibrium value.

2.1.1 The rotational diffusion operator

For hindered Brownian diffusion in an orienting potential, $\mathit{\Gamma}(\boldsymbol{\Omega})$ has the form [35, 27, 36, 37]

$$\begin{aligned} \mathit{\Gamma}(\boldsymbol{\Omega}) &= \boldsymbol{J}(\boldsymbol{\Omega}) R \left(\boldsymbol{J}(\boldsymbol{\Omega}) + \frac{1}{k_{\mathrm{B}}T} \left(\boldsymbol{J}(\boldsymbol{\Omega}) U(\boldsymbol{\Omega}) \right) \right) \\ &= \sum_{i,j=x,y,z} R_{ij} J_i(\boldsymbol{\Omega}) \left(J_j(\boldsymbol{\Omega}) + \frac{1}{k_{\mathrm{B}}T} \left(J_j(\boldsymbol{\Omega}) U(\boldsymbol{\Omega}) \right) \right) \end{aligned} \tag{2.4}$$

where $\boldsymbol{J} = [J_x \;\; J_y \;\; J_z]^{\mathrm{T}}$ is the angular momentum vector describing the rotation of the molecule, R is the rotational diffusion tensor, k_{B} is the Boltzmann factor, and T is the temperature of the system. The x, y, and z indices indicate the axes of a molecule-fixed frame. For brevity, the explicit orientation dependence of $\boldsymbol{J}(\boldsymbol{\Omega})$ and $U(\boldsymbol{\Omega})$ will be omitted from here on out. Equation 2.4 can be simplified by defining a scaled potential $u = U/k_{\mathrm{B}}T$, in which case the general expression for $\mathit{\Gamma}(\boldsymbol{\Omega})$ becomes

$$\mathit{\Gamma}(\boldsymbol{\Omega}) = \boldsymbol{J}R\left(\boldsymbol{J} + \boldsymbol{J}u\right) = \sum_{i,j=x,y,z} R_{ij} J_i \left(J_j + J_j u\right). \tag{2.5}$$

The diffusion tensor R is a second-rank 3×3 Cartesian tensor with scalar elements that describe the rotational dynamics of the molecule and is given by

$$R = \begin{bmatrix} R_{xx} & R_{xy} & R_{xz} \\ R_{yx} & R_{yy} & R_{yz} \\ R_{zx} & R_{zy} & R_{zz} \end{bmatrix} \tag{2.6}$$

for any general molecule-fixed frame of reference. In its eigenframe, R is diagonal and has the form

$$R = \begin{bmatrix} R_x & 0 & 0 \\ 0 & R_y & 0 \\ 0 & 0 & R_z \end{bmatrix}. \tag{2.7}$$

This molecule-fixed frame is usually referred to as the diffusion frame. In the diffusion frame, equation 2.5 simplifies to

$$\mathit{\Gamma}(\boldsymbol{\Omega}) = \sum_{i=x,y,z} R_i J_i \left(J_i + J_i u\right). \tag{2.8}$$

2.1.2 Symmetrization of the diffusion operator

The rotational diffusion operator of equation 2.5 and equation 2.8 describes the molecular rotational dynamics, but the operator is not Hermitian. Because we eventually wish to combine this classical rotational diffusion operator with a Hermitian quantum mechanical spin Hamiltonian operator, the solution of the SLE can be greatly simplified if $\mathit{\Gamma}(\boldsymbol{\Omega})$ were to be made Hermitian as well. The diffusion operator can be made Hermitian according to the following symmetrizing transformation of $\mathit{\Gamma}$ [20, 38, 25, 22]:

$$\tilde{\mathit{\Gamma}} = P_{\mathrm{eq}}^{-1/2} \mathit{\Gamma} P_{\mathrm{eq}}^{1/2} \tag{2.9}$$

where $\tilde{\mathit{\Gamma}}$ is Hermitian and is called the symmetrized rotational diffusion operator, and P_{eq} is the equilibrium orientational distribution of equation 2.3 [39]. For convenience, the explicit orientation dependence of $\varGamma(\boldsymbol{\Omega})$ and $P_{\mathrm{eq}}(\boldsymbol{\Omega})$ are omitted for this symmetrization discussion. Using a scaled population density $\tilde{P} = P_{\mathrm{eq}}^{-1/2}P$, we can write a symmetrized rotational Smoluchowski equation that is similar to equation 2.1:

$$\frac{\partial}{\partial t}\tilde{P} = -\tilde{\varGamma}\tilde{P} \tag{2.10}$$

where $\tilde{\varGamma}$ is Hermitian and is called the symmetrized rotational diffusion operator and $\tilde{P}$ is the above-mentioned scaled population density. Substitution of equation 2.9 into equation 2.10, after much operator algebra, results in the following expression for the symmetrized diffusion operator:

$$\tilde{\varGamma} = \left(\boldsymbol{J} - \frac{1}{2}\left(\boldsymbol{J}u\right)\right) R \left(\boldsymbol{J} + \frac{1}{2}\left(\boldsymbol{J}\boldsymbol{u}\right)\right) = \sum_{i,j=x,y,z} R_{ij}\left(J_iJ_j + \frac{1}{2}\left(J_i\left(J_ju\right)\right) - \frac{1}{4}\left(J_iu\right)\left(J_ju\right)\right). \tag{2.11}$$

The symmetrized diffusion operator of equation 2.11 is Hermitian and, as will be shown, can now be combined with the spin Hamiltonian to construct a Hermitian SLE matrix, which greatly simplifies the calculation of slow-motion CW EPR lineshapes in the SLE formalism. Equation 2.11 is further simplified by moving into the molecule-fixed diffusion frame where the diffusion tensor R is diagonal:

$$\tilde{\varGamma}(\boldsymbol{\Omega}) = \sum_{i=x,y,z} R_i\left[J_i^2 + \frac{1}{2}\left(J_i^2u\right) - \frac{1}{4}\left(J_iu\right)^2\right]. \tag{2.12}$$

For the remainder of this chapter, all further instances of the diffusion operator refer to the symmetrized Hermitian operator of equation 2.12, therefore the tilde will be dropped

2.2 Expansion of the diffusion operator in the orienting potential

In the diffusion frame of equation 2.12, the diffusion operator consists of three terms – one that is potential-independent, one that is linear in the potential, and one that is quadratic in the potential:

$$\varGamma(\boldsymbol{\Omega}) = \varGamma_0(\boldsymbol{\Omega}) + \varGamma_U(\boldsymbol{\Omega}) = \varGamma_0(\boldsymbol{\Omega}) + \frac{1}{2}\varGamma_1(\boldsymbol{\Omega}) - \frac{1}{4}\varGamma_2(\boldsymbol{\Omega}) \tag{2.13}$$

where $\mathit{\Gamma}_U(\boldsymbol{\Omega})$ is the potential-dependent part of the diffusion operator. In the following discussion of the components of $\mathit{\Gamma}(\boldsymbol{\Omega})$, it will be convenient to define new quantities of the diffusion tensor that are composed from linear combinations of the diagonal diffusion tensor components R_x, R_y, and R_z [27, 37, 40]:

$$R_{\mathrm{d}} = \frac{R_x - R_y}{4} \qquad R_{\perp} = \frac{R_x + R_y}{2} \qquad R_{\parallel} = R_z. \tag{2.14}$$

2.2.1 Potential-independent component

The potential-independent component of the diffusion operator $\mathit{\Gamma}_0$ is given by

$$\mathit{\Gamma}_0(\boldsymbol{\Omega}) = \sum_{i=x,y,z} R_i J_i^2 = R_x J_x^2 + R_y J_y^2 + R_z J_z^2. \tag{2.15}$$

Equation 2.15 can be rewritten in terms of the diffusion tensor components of equation 2.14 using the raising and lowering operators $J_+ = J_x + \mathrm{i}J_y$ and $J_- = J_x - \mathrm{i}J_y$:

$$\mathit{\Gamma}_0(\boldsymbol{\Omega}) = R_{\mathrm{d}}\left(J_+^2 + J_-^2\right) + R_{\perp}\left(\boldsymbol{J}^2 - J_z^2\right) + R_{\parallel} J_z^2. \tag{2.16}$$

2.2.2 Linear component

The component of the diffusion operator that is linear in the potential $\mathit{\Gamma}_1$ is given by

$$\mathit{\Gamma}_1(\boldsymbol{\Omega}) = \sum_{i=x,y,z} R_i\left(J_i^2 u\right) = R_x J_x^2 u + R_y J_y^2 u + R_z J_z^2 u. \tag{2.17}$$

In terms of the diffusion tensor components given in equation 2.14, $\mathit{\Gamma}_1(\boldsymbol{\Omega})$ is given by

$$\mathit{\Gamma}_1(\boldsymbol{\Omega}) = R_{\mathrm{d}}\left(J_+^2 + J_-^2\right) u + R_{\perp}\left(\boldsymbol{J}^2 - J_z^2\right) u + R_{\parallel} J_z^2 u. \tag{2.18}$$

2.2.3 Quadratic component

The component of the diffusion operator that is quadratic in the potential, $\mathit{\Gamma}_2$, is given by

$$\mathit{\Gamma}_2(\boldsymbol{\Omega}) = \sum_{i=x,y,z} R_i \left(J_i u\right)^2 = R_x \left(J_x u\right)^2 + R_y \left(J_y u\right)^2 + R_z \left(J_z u\right)^2 . \tag{2.19}$$

In terms of the diffusion tensor components of equation 2.14, equation 2.19 has the form

$$\mathit{\Gamma}_2(\boldsymbol{\Omega}) = R_\mathrm{d} \left[\left(J_+ u\right)^2 + \left(J_- u\right)^2\right] + R_\perp \left(J_+ u\right)\left(J_- u\right) + R_\parallel \left(J_z u\right)^2 . \tag{2.20}$$

2.3 The stochastic Liouville equation

2.3.1 The Liouville–von Neumann equation

The Liouville–von Neumann equation describes the time evolution of the state of a quantum system under a Hamiltonian that contains the relevant interactions within the system and between the system and its environment. In general, the Hamiltonian can be written in Hilbert space as

$$\hat{H}(t) = \hat{H}_0 + \hat{H}_1(t) \tag{2.21}$$

where $\hat{H}_0$ includes all the time-independent interactions in the system and $\hat{H}_1(t)$ includes any time-dependent interactions within the system or between the system and its environment. In a CW EPR experiment, $\hat{H}_0$ typically includes the internal system interactions such as the Zeeman interactions, hyperfine interactions, zero-field interactions, and so on. The time-dependent part, $\hat{H}_1(t)$, usually describes the interaction of the spin system with the B_1 magnetic field due to the incoming CW microwave radiation, which can be treated as a perturbation to $\hat{H}_0$ due to the low microwave power used in CW experiments (i.e. $B_1 \ll B_0$). In Hilbert space, where the eigenvectors of $\hat{H}(t)$ represent the spin states of the system and the eigenvalues of $\hat{H}(t)$ represent the spin state energies, the Liouville-von Neumann equation is

$$\frac{\partial}{\partial t}\hat{\rho}(t) = -\mathrm{i}\left[\hat{H}(t), \hat{\rho}(t)\right] \tag{2.22}$$

where $\hat{\rho}(t)$ is the time-dependent density operator and the right-hand side of equation 2.22 includes the commutator of the Hamiltonian and density operators. Note that equation 2.22 is in angular-frequency units (i.e. the Hamiltonian is scaled by $\hbar^{-1}$), which is the convention used throughout most of this text. In the Hilbert space representation of equation 2.22, both the Hamiltonian and the density operator have $n \times n$ matrix representations, where n is the number of spin states in the system. Because we will be dealing primarily with relaxation, and given that the commutator in equation 2.22 can be considered an operation on $\hat{\rho}(t)$, it is convenient to reformulate equation 2.22 in Liouville space as

$$\frac{\partial}{\partial t} \left|\hat{\rho}(t)\right\rangle = -\mathrm{i}\hat{\hat{H}}(t) \left|\hat{\rho}(t)\right\rangle \tag{2.23}$$

where $\left|\hat{\rho}(t)\right\rangle$ is a vector in Liouville space and $\hat{\hat{H}}(t)$ is the Hamiltonian commutation superoperator. In Liouville space, Hilbert-space operators are vectors and the operators in Liouville space, which operate on Hilbert-space operators, are referred to as superoperators. The Liouville-space vector $\left|\hat{\rho}(t)\right\rangle$ can be constructed from the Hilbert-space operator $\hat{\rho}(t)$ by stacking sequentially the columns of $\hat{\rho}(t)$. The Hamiltonian commutation superoperator $\hat{\hat{H}}(t)$ (or any Liouville space superoperator) can be constructed from the Hilbert-space Hamiltonian operator $\hat{H}(t)$ via the sum of direct products

$$\hat{\hat{H}} = \hat{1} \otimes \hat{H} - \hat{H}^{\mathrm{T}} \otimes \hat{1} \tag{2.24}$$

in which $\hat{1}$ is the unit operator with the same Hilbert space dimensions as the Hamiltonian [41]. In Liouville space, the eigenvalues of the Hamiltonian commutation superoperator are the transition energies between each pair of spin states in the system. Therefore, the dimension of $\left|\hat{\rho}(t)\right\rangle$ is $n^2 \times 1$ and the dimension of $\hat{\hat{H}}(t)$ is $n^2 \times n^2$ in Liouville space.

2.3.2 Derivation of the stochastic Liouville equation

In slowly tumbling anisotropic systems, the spin-state energies are strongly coupled to the rotational dynamics of the molecule due to the orientational dependence of the spin Hamiltonian interactions. Therefore, the effect of rotational motion on the time evolution of the density operator must be included in equation 2.23. The effect of rotation is to change the orientation $\boldsymbol{\Omega}$ of the molecule relative to the external magnetic field B_0 in a time-dependent fashion. The spin Hamiltonian depends on the orientation of the molecule, therefore the $\hat{\hat{H}}_0$ part of equation 2.23 can be written as

$$\frac{\partial}{\partial t} \left|\hat{\rho}(t)\right\rangle = -\mathrm{i}\hat{\hat{H}}(\boldsymbol{\Omega}(t)) \left|\hat{\rho}(t)\right\rangle \tag{2.25}$$

where the previously time-independent Hamiltonian now has an implicit time dependence due to the time dependence of the molecular orientation $\boldsymbol{\Omega}(t)$. At some arbitrary initial time $t = 0$, the time evolution of a spin system designated by $\hat{\rho}$ with initial orientation $\boldsymbol{\Omega}_0$ is

$$\frac{\partial}{\partial t} \left|\hat{\rho}(t|\boldsymbol{\Omega}_0)\right\rangle\rangle = -\mathrm{i}\hat{\hat{H}}(\boldsymbol{\Omega}(t)) \left|\hat{\rho}(t|\boldsymbol{\Omega}_0)\right\rangle\rangle \tag{2.26}$$

where the notation $\hat{\rho}(t|\boldsymbol{\Omega}_0)$ designates that $\hat{\rho}$ is a function of time t, but that the value of $\hat{\rho}$ at time t is dependent on the orientation of the molecule at time $t = 0$, which is $\boldsymbol{\Omega}_0$. In analogy with equation 2.2, equation 2.1 can be written as [42]

$$\frac{\partial}{\partial t} P(\boldsymbol{\Omega}, t|\boldsymbol{\Omega}_0, 0) = -\hat{\hat{\Gamma}}(\boldsymbol{\Omega}) P(\boldsymbol{\Omega}, t|\boldsymbol{\Omega}_0, 0) \tag{2.27}$$

where the notation $P(\boldsymbol{\Omega}, t|\boldsymbol{\Omega}_0, 0)$ denotes the probability that a molecule has orientation $\boldsymbol{\Omega}$ at some time t given that it had orientation $\boldsymbol{\Omega}_0$ at a previous initial time $t = 0$.

The stochastic Liouville equation results from combining the time evolution of the quantum mechanical spin system in equation 2.26 with the time evolution of the classical orientational distribution of equation 2.27. To do so, we may consider an ensemble average of density operators over all possible initial orientations $\boldsymbol{\Omega}_0$:

$$\left|\hat{\rho}(\boldsymbol{\Omega}, t)\right\rangle\rangle = \int \mathrm{d}\boldsymbol{\Omega}_0 \left|\hat{\rho}(t|\boldsymbol{\Omega}_0)\right\rangle\rangle\, P(\boldsymbol{\Omega}, t|\boldsymbol{\Omega}_0, 0) P(\boldsymbol{\Omega}_0, 0). \tag{2.28}$$

In equation 2.28, $P(\boldsymbol{\Omega}, t|\boldsymbol{\Omega}_0, 0)$ is the probability that a molecule with initial orientation $\boldsymbol{\Omega}_0$ at time $t = 0$ will have orientation $\boldsymbol{\Omega}$ at time t and $P(\boldsymbol{\Omega}_0, 0)$ is the probability that a molecule has the initial orientation $\boldsymbol{\Omega}_0$ at time $t = 0$. Integrating over all possible initial orientations $\boldsymbol{\Omega}_0$ gives all trajectories that result in $\left|\hat{\rho}(\boldsymbol{\Omega}, t)\right\rangle\rangle$, which is the spin state $\hat{\rho}$ with orientation $\boldsymbol{\Omega}$ at time t. The time evolution of $\left|\hat{\rho}(\boldsymbol{\Omega}, t)\right\rangle\rangle$ is given by

$$\begin{aligned} &\frac{\partial}{\partial t} \left|\hat{\rho}(\boldsymbol{\Omega}, t)\right\rangle\rangle = \\ &\int \mathrm{d}\boldsymbol{\Omega}_0 \Big[\left(\frac{\partial}{\partial t} \left|\hat{\rho}(t|\boldsymbol{\Omega}_0)\right\rangle\rangle\right) P(\boldsymbol{\Omega}, t|\boldsymbol{\Omega}_0, 0) + \left|\hat{\rho}(t|\boldsymbol{\Omega}_0)\right\rangle\rangle \left(\frac{\partial}{\partial t} P(\boldsymbol{\Omega}, t|\boldsymbol{\Omega}_0, 0)\right) \Big] P(\boldsymbol{\Omega}_0, 0). \end{aligned} \tag{2.29}$$

Note that the time evolutions of $\left|\hat{\rho}(t|\boldsymbol{\Omega}_0)\right\rangle\rangle$ and $P(\boldsymbol{\Omega}, t|\boldsymbol{\Omega}_0, 0)$ in equation 2.29 are defined above in equations 2.26 and 2.27, respectively. Substituting equations 2.26 and 2.27 into equation 2.29 gives

$$\begin{aligned}\frac{\partial}{\partial t}\left|\hat{\rho}(\boldsymbol{\Omega},t)\right\rangle &= \\ &\int \mathrm{d}\boldsymbol{\Omega}_0\Big[-\mathrm{i}\hat{\hat{H}}(\boldsymbol{\Omega})\left|\hat{\rho}(t|\boldsymbol{\Omega}_0)\right\rangle P(\boldsymbol{\Omega},t|\boldsymbol{\Omega}_0,0)-\left|\hat{\rho}(t|\boldsymbol{\Omega}_0)\right\rangle \hat{\hat{\Gamma}}(\boldsymbol{\Omega})P(\boldsymbol{\Omega},t|\boldsymbol{\Omega}_0,0)\Big]P(\boldsymbol{\Omega}_0,0).\end{aligned} \tag{2.30}$$

Because $\hat{\hat{H}}(\boldsymbol{\Omega})$ and $\hat{\hat{\Gamma}}(\boldsymbol{\Omega})$ do not depend on the initial orientation $\boldsymbol{\Omega}_0$, they can be factored out of the integral in equation 2.30 to give

$$\frac{\partial}{\partial t}\left|\hat{\rho}(\boldsymbol{\Omega},t)\right\rangle = \Big[-\mathrm{i}\hat{\hat{H}}(\boldsymbol{\Omega})-\hat{\hat{\Gamma}}(\boldsymbol{\Omega})\Big]\int \mathrm{d}\boldsymbol{\Omega}_0\left|\hat{\rho}(t|\boldsymbol{\Omega}_0)\right\rangle P(\boldsymbol{\Omega},t|\boldsymbol{\Omega}_0,0)P(\boldsymbol{\Omega}_0,0). \tag{2.31}$$

Finally, substituting equation 2.28 for the integral in equation 2.31 gives

$$\frac{\partial}{\partial t}\left|\hat{\rho}(\boldsymbol{\Omega},t)\right\rangle = -\Big[\mathrm{i}\hat{\hat{H}}(\boldsymbol{\Omega})+\hat{\hat{\Gamma}}(\boldsymbol{\Omega})\Big]\left|\hat{\rho}(\boldsymbol{\Omega},t)\right\rangle = -\mathrm{i}\hat{\hat{H}}(\boldsymbol{\Omega})\left|\hat{\rho}(\boldsymbol{\Omega},t)\right\rangle - \hat{\hat{\Gamma}}(\boldsymbol{\Omega})\left|\hat{\rho}(\boldsymbol{\Omega},t)\right\rangle. \tag{2.32}$$

Equation 2.32 is the stochastic Liouville equation (SLE). It is a semiclassical equation that describes the time evolution of a spin system propagated by a quantum mechanical Hamiltonian $\hat{\hat{H}}$ in which the spin state energy is coupled to the molecular rotational dynamics, which are propagated by the classical Markovian operator $\hat{\hat{\Gamma}}$. From the stochastic Liouville equation, a lineshape function can be derived to model the CW EPR lineshape for any general spin system.

2.4 The spectral lineshape function

Equation 2.32 is analogous to the density operator formalism of the time-dependent Schrödinger equation. However, the time propagator of $\hat{\rho}$ in the SLE is the Liouvillian operator $(-\mathrm{i}\hat{\hat{H}}+\hat{\hat{\Gamma}})$ rather than the Hamiltonian in the time-dependent Schrödinger equation. To simulate CW EPR spectra using the SLE, there is no need to calculate explicit trajectories for the density operator. Rather, a frequency-dependent lineshape function can be derived from equation 2.32 that can be used to simulate the CW EPR lineshape over a range of microwave frequencies.

In the lab frame, the z-direction is parallel to the direction of the external magnetic field B_0. If the direction of propagation of the incoming microwave radiation is defined to be the lab frame y-direction, then absorption by the EPR sample of that microwave radiation will cause an increase in magnetization from the sample along the lab x-direction. Therefore, the detection operator is $\hat{S}_x$ and the response of the sample to irradiation by the microwave B_1 field is

$$I(\omega) = \langle \hat{S}_x | \hat{\rho}(t) \rangle \tag{2.33}$$

where $I(\omega)$ is the free induction decay (FID) of the sample magnetization after interaction with the B_1 microwave field. Recall that $\hat{\hat{\mathit{\Gamma}}}(\boldsymbol{\mathit{\Omega}})$ in equation 2.32 is the symmetrized diffusion superoperator of equations 2.9 and 2.11, which was derived from the scaled orientational population density $\tilde{P} = P_{\mathrm{eq}}^{-1/2} P$ [20, 38, 25, 22]. Transforming $\hat{\rho}(t)$ in equation 2.33 accordingly gives

$$\hat{\rho}(t) = P_{\mathrm{eq}}^{1/2} \tilde{\rho}(t). \tag{2.34}$$

Considering that the Liouvillian is the time evolution operator, the scaled density operator in equation 2.34 can be rewritten as

$$\tilde{\rho}(t) = e^{-\left(\mathrm{i}\hat{\hat{H}} + \hat{\hat{\mathit{\Gamma}}}\right)t}\, \tilde{\rho}(0) = e^{-\left(\mathrm{i}\hat{\hat{H}} + \hat{\hat{\mathit{\Gamma}}}\right)t}\, P_{\mathrm{eq}}^{-1/2} \hat{\rho}(0) \tag{2.35}$$

where $\hat{\rho}(0)$ is the density operator of equation 2.33 immediately after interaction with the B_1 microwave field. Because the effect of B_1 on the spins is to flip them in the x-direction, $\hat{\rho}(0)$ can be represented by

$$\hat{\rho}(0) = \hat{S}_x P_{\mathrm{eq}} \tag{2.36}$$

where the S_x state is weighted by the orientational distribution P_{eq}. Substituting equation 2.36 into equation 2.35, and equation 2.35 in equation 2.34, yields the following expression for the time-dependent density operator:

$$\hat{\rho}(t) = P_{\mathrm{eq}}^{1/2}\, e^{-\left(\mathrm{i}\hat{\hat{H}} + \hat{\hat{\mathit{\Gamma}}}\right)t}\, P_{\mathrm{eq}}^{-1/2} \hat{S}_x P_{\mathrm{eq}} = P_{\mathrm{eq}}^{1/2}\, e^{-\left(\mathrm{i}\hat{\hat{H}} + \hat{\hat{\mathit{\Gamma}}}\right)t}\, P_{\mathrm{eq}}^{1/2} \hat{S}_x \tag{2.37}$$

where we have used the fact that $\hat{S}_x$ and P_{eq} commute to derive equation 2.37. Finally, substituting equation 2.37 into the FID of equation 2.33 yields the time-dependent lineshape function:

$$I(t) = \langle \hat{S}_x | \hat{\rho}(t) \rangle = \langle \hat{S}_x P_{\mathrm{eq}}^{1/2} |\, e^{-\left(\mathrm{i}\hat{\hat{H}} + \hat{\hat{\mathit{\Gamma}}}\right)t}\, | \hat{S}_x P_{\mathrm{eq}}^{1/2} \rangle\,. \tag{2.38}$$

Taking the Fourier transform of equation 2.38 yields

$$I(\omega) = \int_0^\infty I(t) e^{\left(\mathrm{i}\hat{\hat{H}} + \hat{\hat{\Gamma}}\right)t} \mathrm{d}t = \langle \hat{S}_x P_{\mathrm{eq}}^{1/2} | \left[-\mathrm{i}\hat{\hat{H}} - \hat{\hat{\Gamma}} - \mathrm{i}\omega \hat{\hat{1}} \right]^{-1} | \hat{S}_x P_{\mathrm{eq}}^{1/2} \rangle \tag{2.39}$$

where $\hat{\hat{1}}$ is the identity superoperator, and $\hat{S}_x P_{\mathrm{eq}}^{1/2}$, commonly called the "starting vector", represents the state of the spins in their equilibrium orientational distribution immediately after interaction with B_1. Equation 2.39 is the microwave frequency-dependent spectral lineshape function. The form of equation 2.39 is convenient for simulating slow-motion CW EPR spectra because CW experiments tend to be performed in the frequency (or field) domain rather than the time domain. The problem of simulating slow-motion lineshapes therefore amounts to the solution of equation 2.39 over a range of microwave frequencies for a given spin Hamiltonian and diffusion operator that describe the spin states and orientational distribution in the sample.

2.5 Basis states for matrix representations

2.5.1 Spin basis

In order to calculate the elements of the SLE matrix, a basis must be chosen that incorporates both the spin and spatial degrees of freedom. In Liouville space, the spin basis states, $|\sigma\rangle$, are a finite set of n^2 vectors of dimension $n^2 \times 1$, where n is the number of spin states in the system. The spin states can be chosen to be orthonormal such that

$$\langle \sigma_i | \sigma_j \rangle = \delta_{i,j} \tag{2.40}$$

where the Kronecker delta $\delta_{i,j}$ is equal to 0 if $i \neq j$ and equal to 1 if $i = j$. From these spin states, matrix representations of the spin vector operators may be constructed and, from those matrix elements, the Hamiltonian matrix elements can be calculated as will be shown.

The usual Zeeman, or high-field, states are a simple choice for the spin basis. For example, in this basis a spin $S = 1/2$ system has a complete Hilbert space basis of two 2-dimensional spin vectors with matrix representations

$$|1\rangle = \begin{bmatrix} 1 \\ 0 \end{bmatrix} \quad |2\rangle = \begin{bmatrix} 0 \\ 1 \end{bmatrix} \tag{2.41}$$

where the states $|1\rangle$ and $|2\rangle$ for a $S = 1/2$ system are usually called the $|\alpha\rangle$ and $|\beta\rangle$ states respectively. In Liouville space, the complete spin basis consists of four 4-dimensional spin vectors that are obtained from taking the direct product of each Hilbert space spin vector with the other Hilbert space vectors:

$$|\sigma_1\rangle = |1\rangle \otimes |1\rangle = \begin{bmatrix} 1 \\ 0 \\ 0 \\ 0 \end{bmatrix} \quad |\sigma_2\rangle = |1\rangle \otimes |2\rangle = \begin{bmatrix} 0 \\ 1 \\ 0 \\ 0 \end{bmatrix} \quad |\sigma_3\rangle = |2\rangle \otimes |1\rangle = \begin{bmatrix} 0 \\ 0 \\ 1 \\ 0 \end{bmatrix} \quad |\sigma_4\rangle = |2\rangle \otimes |2\rangle = \begin{bmatrix} 0 \\ 0 \\ 0 \\ 1 \end{bmatrix} . \tag{2.42}$$

In the spin basis of equation 2.41, the $S = 1/2$ Hilbert space spin vector operator $\hat{\boldsymbol{S}} = \left[\hat{S}_x \; \hat{S}_y \; \hat{S}_z\right]^T$ has the following familiar matrix representations (in angular-frequency units):

$$\hat{S}_x = \tfrac{1}{2} \begin{bmatrix} 0 & 1 \\ 1 & 0 \end{bmatrix} \qquad \hat{S}_y = \tfrac{\mathrm{i}}{2} \begin{bmatrix} 0 & 1 \\ -1 & 0 \end{bmatrix} \qquad \hat{S}_z = \tfrac{1}{2} \begin{bmatrix} 1 & 0 \\ 0 & -1 \end{bmatrix} \tag{2.43}$$

and in Liouville space, using equation 2.24, the spin operator matrix representations are

$$\hat{\hat{S}}_x = \tfrac{1}{2} \begin{bmatrix} 0 & 1 & -1 & 0 \\ 1 & 0 & 0 & -1 \\ -1 & 0 & 0 & 1 \\ 0 & -1 & 1 & 0 \end{bmatrix} \qquad \hat{\hat{S}}_y = \tfrac{\mathrm{i}}{2} \begin{bmatrix} 0 & 1 & 1 & 0 \\ -1 & 0 & 0 & 1 \\ -1 & 0 & 0 & 1 \\ 0 & -1 & -1 & 0 \end{bmatrix} \qquad \hat{\hat{S}}_z = \begin{bmatrix} 0 & 0 & 0 & 0 \\ 0 & -1 & 0 & 0 \\ 0 & 0 & 1 & 0 \\ 0 & 0 & 0 & 0 \end{bmatrix} . \tag{2.44}$$

The elements of the Hilbert space operators in equation 2.41 represent components of the spin angular momentum of the spin states $|1\rangle$ and $|2\rangle$ while the elements of the Liouville-space operators in equation 2.42 represent changes in the components of the spin angular momentum upon transistions between the states $|1\rangle$ and $|2\rangle$.

2.5.2 Spatial basis

A spatial basis must also be chosen to describe the rotational dynamics. Several methods exist, such as numerical grids, but we choose the often-used general spherical harmonics, or Wigner functions, which have the form [20]

$$|LMK\rangle = \sqrt{\frac{2L+1}{8\pi^2}} D^L_{MK}(\boldsymbol{\Omega}) \tag{2.45}$$

where D^L_{MK} is a Wigner function of rank L and projections M and K, and the prefactor ensures that the functions are orthonormal such that

$$\langle L_p M_p K_p | L_q M_q K_q \rangle = \delta_{L_p,L_q} \delta_{M_p,M_q} \delta_{K_p,K_q}. \tag{2.46}$$

The explicit form of the Wigner functions are

$$D^L_{MK}(\boldsymbol{\Omega}) = D^L_{MK}(\alpha, \beta, \gamma) = \mathrm{e}^{-\mathrm{i}M\alpha} d^L_{MK}(\beta) \mathrm{e}^{-\mathrm{i}K\gamma} \tag{2.47}$$

where the $d^L_{MK}(\beta)$ consist of products of cosines and their values depend on the values of L, M, and K. The Wigner functions are a convenient choice for the spatial basis because they are eigenfunctions of the angular-momentum operators with the following properties for a body-fixed frame [21, 22]:

$$\begin{aligned} \boldsymbol{J}^2 D^L_{MK} &= L(L+1) D^L_{MK} \\ J_z D^L_{MK} &= -K D^L_{MK} \\ J_z^2 D^L_{MK} &= K^2 D^L_{MK} \\ J_\pm D^L_{MK} &= \sqrt{L(L+1) - K(K \pm 1)} D^L_{MK} \\ J_\pm^2 D^L_{MK} &= \sqrt{(L \mp K - 1)(L \pm K + 1)(L \pm K + 2)} D^L_{MK}. \end{aligned} \tag{2.48}$$

The Wigner functions are also the coefficients for the transformation of the irreducible spherical tensor operators (ISTOs) between coordinate systems and a convenient basis in which the orienting potential $U(\boldsymbol{\Omega})$ can be expanded, as will be shown in the following sections. The normalized Wigner functions describe distributions in the vector space of all possible rotations, or SO(3), and have properties analogous to the spherical harmonic functions, which describe distributions on the surface of a unit sphere. In fact, when $K = 0$ the Wigner functions reduce to the spherical harmonics [20, 27]. Details about the properties of Wigner functions can be found in various texts [43, 44].

2.5.3 Direct product basis

The full basis states of the SLE are constructed in the direct product space of the spin states and orientational states:

$$|LMK\sigma\rangle = |LMK\rangle \otimes |\sigma\rangle \tag{2.49}$$

with n^2m direct product basis vectors of dimension $n^2m \times 1$, where m is the number of Wigner basis functions. Although the complete set of Wigner functions is infinite, in practice the basis can be truncated without loss of accuracy. Longer rotational correlation times and highly anisotropic systems require larger sets of Wigner functions to produce accurate simulations.

An alternative basis, called the K-symmetrized basis, may also be used to simplify numerical calculations by ensuring that the SLE matrix is complex symmetric if the orienting potential is absent or has axial symmetry [27, 21, 22, 37, 45, 46]. This is the default basis used in the general SLE solver. The K-symmetrized basis states can be obtained from the direct product basis states of equation 2.49 via a simple linear transformation. Details about the K-symmetrized basis are given in appendix A.

2.6 Irreducible spherical tensor operator expansion

For a given spin system, the spin Hamiltonian contains a term for each interaction in that system. These interaction terms consist of a scalar product between one spin vector operator and the product of an interaction tensor with another spin vector operator (except in the case of Zeeman interactions, then one of the vector operators is instead the external magnetic field vector). For example, the Hilbert-space spin Hamiltonian for a nitroxide with electron spin $S = 1/2$ and nitrogen-14 nuclear spin $I = 1$ can be written as

$$\hbar\hat{H} = \mu_{\mathrm{B}}\boldsymbol{B} \cdot g \cdot \hat{\boldsymbol{S}} - \mu_{\mathrm{N}}g_{\mathrm{N}}\boldsymbol{B} \cdot \hat{\boldsymbol{I}} + \hat{\boldsymbol{S}} \cdot A \cdot \hat{\boldsymbol{I}} \tag{2.50}$$

where $\boldsymbol{B}$ is the external magnetic field vector, μ_{B} and μ_{N} are the Bohr magneton and nuclear magneton, $\hat{\boldsymbol{S}}$ and $\hat{\boldsymbol{I}}$ are the electron and nuclear spin vector operators in units of $\hbar$, g_{N} is the nuclear g-factor, and g and A are the electron g-tensor and hyperfine tensor respectively. The first two terms are the electron and nuclear Zeeman terms, which describe the interaction of the electron and nuclear spins with the external magnetic field. The third term is the hyperfine term, which describes the interaction between the electron and nuclear spin. In general, the spin Hamiltonian can include other terms that may give a significant contribution to the spin state energies, such as a nuclear quadrupole term for nuclei with nonspherical charge distributions, or electron-electron interaction terms, such as zero-field splitting or exchange coupling for systems with multiple unpaired electrons.

The elements of the spin Hamiltonian of equation 2.50 are straightforward to calculate in a pure spin basis, but are more difficult to calculate in a combined direct product basis of spin and spatial orientation. Because of the choice of Wigner functions for the spatial basis, however, the problem is simplified by separating the Hamiltonian into a linear combination of products of irreducible spherical tensor operators (ISTOs) rather than as a sum of interaction terms as in equation 2.50. In the ISTO expansion, the Hamiltonian is written as

$$\hat{H} = \sum_{\mu} \sum_{l=0}^{2} \boldsymbol{F}^{(l)}_{\mu,\eta} \cdot \hat{\boldsymbol{T}}^{(l)}_{\mu,\eta} \tag{2.51}$$

where μ indicates a particular interaction (e.g. electron Zeeman, hyperfine, etc.), l is the rank of the spherical tensor, η indicates a particular coordinate system (e.g. lab frame, molecular frame, etc.), $\boldsymbol{F}$ is a spatial irreducible spherical tensor (IST) constructed from the elements of the interaction tensors (e.g. g, A, etc.), and $\hat{\boldsymbol{T}}$ is a spin irreducible spherical tensor operator constructed from the spin vector operators (e.g. $\hat{\boldsymbol{S}}$ and $\hat{\boldsymbol{I}}$). Only isotropic ($l = 0$) and anisotropic ($l = 2$) components contribute to the spin Hamiltonian. Each ISTO has $2l + 1$ components m that range from $-l$ to l in integer increments, therefore the expansion of equation 2.51 is

$$\hat{H} = \sum_{\mu} \left((F^{(0,0)}_{\mu,\eta})^* T^{(0,0)}_{\mu,\eta} + \sum_{m=-2}^{2} (-1)^l (F^{(2,m)}_{\mu,\eta})^* T^{(2,m)}_{\mu,\eta} \right) \tag{2.52}$$

where m is the projection number and the superscripts denote rank and projection as (l, m). In equation 2.50, each term in the Hamiltonian accounts for a specific interaction whereas in equations 2.51 and 2.52, the Hamiltonian is written as a sum of isotropic and anisotropic terms, with each term consisting of contributions from all the interaction terms in the equation 2.50 Hamiltonian. For a general spin Hamiltonian term $\hat{\boldsymbol{A}} \cdot C \cdot \hat{\boldsymbol{B}}$, with the interaction between $\hat{\boldsymbol{A}}$ and $\hat{\boldsymbol{B}}$ parameterized by the interaction tensor C, defined as

$$\hat{\boldsymbol{A}} = \begin{bmatrix} \hat{A}_x \\ \hat{A}_y \\ \hat{A}_z \end{bmatrix} \qquad \hat{\boldsymbol{B}} = \begin{bmatrix} \hat{B}_x \\ \hat{B}_y \\ \hat{B}_z \end{bmatrix} \qquad C = \begin{bmatrix} C_{xx} & C_{xy} & C_{xz} \\ C_{yx} & C_{yy} & C_{yz} \\ C_{zx} & C_{zy} & C_{zz} \end{bmatrix} \tag{2.53}$$

the ISTOs can be constructed in a straightforward fashion from the equation 2.53 spin vector operators $\hat{\boldsymbol{A}}$ and $\hat{\boldsymbol{B}}$, and interaction tensor C, according to table 2.6.

(l, m)	$F^{(l,m)}(C)$	$\hat{T}^{(l,m)}(\hat{\boldsymbol{A}}, \hat{\boldsymbol{B}})$
(0,0)	$-\frac{1}{\sqrt{3}}\left(C_{xx} + C_{yy} + C_{zz}\right)$	$-\frac{1}{\sqrt{3}}\left(\hat{A}_x\hat{B}_x + \hat{A}_y\hat{B}_y + \hat{A}_z\hat{B}_z\right)$
(1,1)	$-\frac{1}{2}\left(C_{zx} - C_{xz} + \mathrm{i}C_{zy} - C_{yz}\right)$	$-\frac{1}{2}\left(\hat{A}_x\hat{B}_z - \hat{A}_z\hat{B}_x + \mathrm{i}\hat{A}_y\hat{B}_z - \mathrm{i}\hat{A}_z\hat{B}_y\right)$
(1,0)	$-\frac{\mathrm{i}}{\sqrt{2}}\left(C_{xy} - C_{yx}\right)$	$-\frac{\mathrm{i}}{\sqrt{2}}\left(\hat{A}_{yx} - \hat{B}_{xy}\right)$
(1,-1)	$-\frac{1}{2}\left(C_{zx} - C_{xz} - \mathrm{i}C_{zy} + C_{yz}\right)$	$-\frac{1}{2}\left(\hat{A}_x\hat{B}_z - \hat{A}_z\hat{B}_x - \mathrm{i}\hat{A}_y\hat{B}_z + \mathrm{i}\hat{A}_z\hat{B}_y\right)$
(2,2)	$\frac{1}{2}\left(C_{xx} - C_{yy} + \mathrm{i}C_{xy} + \mathrm{i}C_{yx}\right)$	$\frac{1}{2}\left(\hat{A}_x\hat{B}_x - \hat{A}_y\hat{B}_y + \mathrm{i}\hat{A}_x\hat{B}_y + \mathrm{i}\hat{A}_y\hat{B}_x\right)$
(2,1)	$-\frac{1}{2}\left(C_{xz} + C_{zx} + \mathrm{i}C_{yz} + \mathrm{i}C_{zy}\right)$	$-\frac{1}{2}\left(\hat{A}_x\hat{B}_z + \hat{A}_z\hat{B}_x + \mathrm{i}\hat{A}_y\hat{B}_z + \mathrm{i}\hat{A}_z\hat{B}_y\right)$
(2,0)	$\frac{1}{\sqrt{6}}\left(2C_{zz} - C_{xx} - C_{yy}\right)$	$\frac{1}{\sqrt{6}}\left(2\hat{A}_z\hat{B}_z - \hat{A}_x\hat{B}_x - \hat{A}_y\hat{B}_y\right)$
(2,-1)	$\frac{1}{2}\left(C_{xz} + C_{zx} - \mathrm{i}C_{yz} - \mathrm{i}C_{zy}\right)$	$\frac{1}{2}\left(\hat{A}_x\hat{B}_z + \hat{A}_z\hat{B}_x - \mathrm{i}\hat{A}_y\hat{B}_z - \mathrm{i}\hat{A}_z\hat{B}_y\right)$
(2,-2)	$\frac{1}{2}\left(C_{xx} - C_{yy} - \mathrm{i}C_{xy} - \mathrm{i}C_{yx}\right)$	$\frac{1}{2}\left(\hat{A}_x\hat{B}_x - \hat{A}_y\hat{B}_y - \mathrm{i}\hat{A}_x\hat{B}_y - \mathrm{i}\hat{A}_y\hat{B}_x\right)$

Table 2.1: General expressions for the construction of the spin and spatial spherical tensors in terms of their more familiar Cartesian components.

2.6.1 Frames of reference

In the slow-motion problem, there are several frames of reference in which different tensors or operators are naturally defined. Figure 2.2 shows the important reference frames for the solution of the SLE. An advantage of the ISTO approach is that it allows for a simple transformation between the different coordinate systems in which the vector operators and interaction tensors have been constructed, with Wigner functions as the transformation coefficients.

The spatial IST $\boldsymbol{F}$ and spin ISTO $\hat{\boldsymbol{T}}$ in equation 2.51 must be represented in the same coordinate system, as indicated by the η subscript. Conveniently, ISTOs of the same rank transform from one coordinate system to another as linear combinations of themselves with Wigner function coefficients. For example, an ISTO of rank l and projection m in coordinate system η can be expanded as a linear combination of the ISTO projections of the same rank l in coordinate system η' as

$$\boldsymbol{F}_{\eta}^{(l)} = D^{(l)}\big(\boldsymbol{\Omega}_{\eta' \to \eta}\big)\boldsymbol{F}_{\eta'}^{(l)} \tag{2.54}$$

where $D^{(l)}\big(\boldsymbol{\Omega}_{\eta' \to \eta}\big)$ is the $(2l+1) \times (2l+1)$ Wigner transformation matrix that transforms the ISTs in coordinate system η' to ISTs in coordinate system η. Equation 2.54 is a matrix equation. The transformation of a single IST (i.e. a single element of $\boldsymbol{F}^{(l)}$) is

$$F_{\eta}^{(l,m)} = \sum_{m'=-l}^{l} D_{m,m'}^{l}\big(\boldsymbol{\Omega}_{\eta' \to \eta}\big)F_{\eta'}^{(l,m')}. \tag{2.55}$$

In general, the rotational motion can be accounted for by considering the time dependence of $\boldsymbol{\Omega}_{\mathrm{D,d}}$, which is the rotation that brings the (usually static) director frame (d) into the dynamic molecule-fixed diffusion frame (D), as shown in figure 2.2.

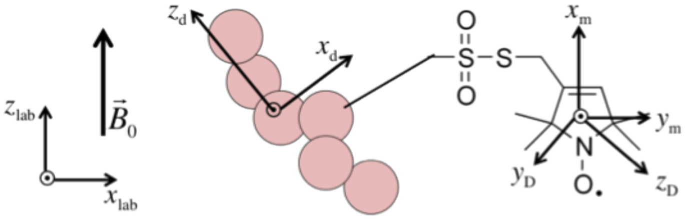

Figure 2.2: Important coordinate systems in the slow-motion problem. The lab frame (lab) is a static frame in which the z_{lab} direction is parallel to the B_0 field. The molecular frame (m) and diffusion frame (D) are dynamic molecule-fixed frames, usually in which the g-tensor and diffusion tensor are diagonal respectively. The director frame (d), present if the paramagnetic molecule is attached to some surface or host molecule, may be either static or dynamic. The time-dependent change in orientation between the static and dynamic frames account for the coupling of rotational motion with the spin state energy levels.

It is most convenient to calculate the Hamiltonian in the lab frame:

$$\hat{H}_{\mathrm{lab}} = \sum_{\mu}\sum_{l=0}^{2} \boldsymbol{F}_{\mu,\mathrm{lab}}^{(l)} \cdot \hat{\boldsymbol{T}}_{\mu,\mathrm{lab}}^{(l)} = \sum_{\mu}\sum_{l}\sum_{m} (-1)^{l}(F_{\mu,\mathrm{lab}}^{(l,m)})^{*}\hat{T}_{\mu,\mathrm{lab}}^{(l,m)}. \tag{2.56}$$

The spin vector ISTOs $\hat{\boldsymbol{T}}$ are already defined in the lab frame, but the spatial ISTs $\boldsymbol{F}$ are usually defined in the molecular frame and must be transformed into the laboratory frame.

In the case of isotropic rotational diffusion, the diffusion frame may be chosen to be colinear with the molecular frame so that the spatial ISTs $\boldsymbol{F}$ are identical in both frames. The transformation of the Hamiltonian to equation 2.56 can then be done sequentially from the diffusion frame to the director frame, and then from the director frame to the lab frame, according to equations 2.54 and 2.55 as

$$\begin{aligned}\hat{H}_{\text{lab}} &= \sum_{\mu}\sum_{l}\sum_{m,m',m''} D^{l}_{m,m'}\left(\boldsymbol{\Omega}_{\text{d}\to\text{lab}}\right) D^{l}_{m',m''}\left(\boldsymbol{\Omega}_{\text{D}\to\text{d}}\right) F^{*(l,m'')}_{\mu,\text{D}} \hat{T}^{(l,m)}_{\mu,\text{lab}} \\ &= \sum_{l}\sum_{m',m''} D^{l}_{m',m''}\left(\boldsymbol{\Omega}_{\text{D}\to\text{d}}\right)\left[\sum_{\mu}\sum_{m} D^{l}_{m,m'}\left(\boldsymbol{\Omega}_{\text{d}\to\text{lab}}\right) F^{*(l,m'')}_{\mu,\text{D}} \hat{T}^{(l,m)}_{\mu,\text{lab}}\right] \\ &= \sum_{l}\sum_{m',m''} D^{l}_{m',m''}\left(\boldsymbol{\Omega}_{\text{D}\to\text{d}}\right) \hat{Q}^{l}_{m',m''}\end{aligned} \tag{2.57}$$

where we have collected all time-independent quantities into the operators $\hat{Q}$, which we call the rotational basis operators (RBOs). The factor of $(-1)^l$ can be omitted because the sum only includes terms with even l. All of the time dependence is in the stochastically varying orientation $\boldsymbol{\Omega}_{\text{D,d}}$. Liouville space representations of the RBOs are easily constructed from the Hilbert space RBOs via the transformation of equation 2.24.

It is in the construction of the ISTOs and RBOs that we have shown how to generalize the problem of solving the SLE for any spin system. The ISTOs may be constructed in Hilbert space according to table 2.6 regardless of the number of interaction terms in the spin Hamiltonian or the nature of those terms. No matter how large or complex the spin system, all of the information about the system that is needed to solve the SLE is contained within just 26 RBOs, one rank-0 isotropic RBO and 25 rank-2 anisotropic RBOs. Each of the RBOs may then be transformed into Liouville space by use of equation 2.24 for calculation of the Liouville-space Hamiltonian superoperator matrix elements.

2.7 Matrix elements of the SLE superoperators

2.7.1 The Hamiltonian superoperator

In order to implement the SLE on a computer, matrix representations of the Hamiltonian and diffusion superoperator must be constructed. The Hamiltonian can be written as a linear combination of the RBOs:

$$\hat{\hat{H}} = \sum_{LMK} \hat{\hat{Q}}^L_{MK} D^L_{MK}. \tag{2.58}$$

In the direct product basis of equation 2.49, the matrix elements of the Hamiltonian are

$$H_{ip,jq} = \langle\sigma_i\chi_p| \hat{\hat{H}} |\sigma_j\chi_q\rangle = \sum_{LMK} \langle\sigma_i\chi_p| \hat{\hat{Q}}^L_{MK} D^L_{MK} |\sigma_j\chi_q\rangle = \sum_{LMK} \langle\sigma_i| \hat{\hat{Q}}^L_{MK} |\sigma_j\rangle \langle\chi_p| D^L_{MK} |\chi_q\rangle \tag{2.59}$$

where $|\chi_p\rangle = |L_pM_pK_p\rangle$ has been introduced as the shorthand notation for the Wigner basis functions. The indices i and j are spin basis function indices that each run from 1 to n^2 (where n is the number spin states in Hilbert space), and p and q are Wigner basis function indices that run from 1 to m (where m is the number of spatial basis functions). However, keep in mind that the matrix representation of the Hamiltonian superoperator is an $n^2m \times n^2m$ matrix therefore the combination indices ip and jq range from 1 to n^2m in the direct product basis.

Note that the orientational integration over the product of three Wigner functions in equation 2.59 can be separated from the spin state integration because the RBOs $\hat{\hat{Q}}^L_{MK}$ only operate on the spin part of the basis functions. Using the normalized Wigner functions of equation 2.45, the integral over $\boldsymbol{\Omega}_{\mathrm{D}\to\mathrm{d}}$ of the product of Wigner functions in equation 2.59 can be expressed as the following product of $3j$-symbols:

$$\begin{aligned} \langle\chi_p| D^L_{MK} |\chi_q\rangle &= \frac{\sqrt{2L_p+1}\sqrt{2L_q+1}}{8\pi^2} \int \mathrm{d}\boldsymbol{\Omega}_{\mathrm{D,d}} (D^{L_p}_{M_pK_p})^* D^L_{MK} D^{L_q}_{M_qK_q} \\ &= C_{pq}(-1)^L \begin{pmatrix} L_p & L & L_q \\ -M_p & M & M_q \end{pmatrix} \begin{pmatrix} L_p & L & L_q \\ -K_p & K & K_q \end{pmatrix} \end{aligned} \tag{2.60}$$

where $C_{pq} = (-1)^{K_p-M_p}\sqrt{2L_p+1}\sqrt{2L_q+1}$. The quantities in parentheses are called $3j$-symbols, which are numbers that are readily calculated according to the theory of coupling of angular momenta [44, 43]. Because the elements of the RBOs have already been calculated from the ISTOs, the spin integration simply gives the corresponding matrix element of $\hat{\hat{Q}}^L_{MK}$:

$$\langle\sigma_i| \hat{\hat{Q}}^L_{MK} |\sigma_j\rangle = (Q^L_{MK})_{i,j}. \tag{2.61}$$

Recall that there are only 26 RBOs, one rank-0 isotropic RBO and 25 rank-2 anisotropic RBOs. Therefore, the sum over LMK in equation 2.59 only includes $L = 0$ and $L = 2$.

Furthermore, from the properties of coupling of angular momenta [44, 43], the $3j$-symbols can only be nonzero when the following conditions are satisfied:

$$\begin{aligned} |L_p - L_q| &\leq L \\ -M_p + M_q + M &= 0 \\ -K_p + K_q + K &= 0. \end{aligned} \tag{2.62}$$

Combining equations 2.60 and 2.61 and using the nonzero condition 2.62 of the $3j$-symbols, only the following matrix elements of the Hamiltonian can be nonzero:

$$H_{ip,jq} = \langle \chi_p \sigma_i | \hat{\hat{H}} | \chi_q \sigma_j \rangle = C_{pq} \sum_{l=0,2} Q^l_{\Delta M \Delta K_{i,j}} \begin{pmatrix} L_p & l & L_q \\ -M_p & \Delta M & M_q \end{pmatrix} \begin{pmatrix} L_p & l & L_q \\ -K_p & \Delta K & K_q \end{pmatrix} \tag{2.63}$$

where $\Delta M = M_p - M_q$ and $\Delta K = K_p - K_q$.

2.7.2 The rotational diffusion superoperator

The rotational diffusion superoperator $\hat{\hat{\Gamma}}$ in the SLE of equation 2.32 accounts for relaxation due to rotational motion. It is essentially a kinetic operator with elements that describe the rate at which a molecule in a particular orientation at time t will be in some other orientation at time $t + \Delta t$. The kinetics are assumed to be Markovian, meaning that the orientational state of the system at time $t + \Delta t$ depends only on the state of the system at time t and not on the state of the system at any time prior to t [47, 18, 20].

The matrix elements of $\hat{\hat{\Gamma}}$ depend on the presence of the orienting potential $U(\boldsymbol{\Omega})$, which describes preferential orientations of the paramagnetic molecule, and on the diffusion tensor R, which describes the rotational dynamics of the molecule [27, 37]. To calculate the matrix elements of $\hat{\hat{\Gamma}}$, it is convenient to work in the molecule-fixed diffusion frame (d) in which the diffusion tensor R is diagonal, as in equation 2.7.

Now that the Wigner basis has been introduced in equation 2.45, the expressions for the potential-dependent parts of the rotational diffusion superoperator in equations 2.18 and 2.20 can be derived in the Wigner basis.

The orienting potential $U(\boldsymbol{\Omega})$, introduced as a component of the diffusion operator $\Gamma(\boldsymbol{\Omega})$ in equations 2.3 and 2.4, can be expanded in a basis of Wigner functions to construct any general potential [48]:

$$U(\boldsymbol{\Omega}) = -k_{\mathrm{B}}T \sum_{L,M,K} \lambda^L_{MK} D^L_{MK}(\boldsymbol{\Omega}) \tag{2.64}$$

where the λ^L_{MK} are complex expansion coefficients of the potential in the Wigner basis. The sum over L ranges from 0 to $L_{\max}$, where $L_{\max}$ is any nonnegative integer, and the sum over M and K range at most from $-L$ to L. The only restriction on the orienting potential is that it is everywhere real-valued:

$$U(\boldsymbol{\Omega}) = U^*(\boldsymbol{\Omega}). \tag{2.65}$$

Combining equations 2.64 and 2.65 gives

$$\sum_{L,M,K} \lambda^L_{MK} D^L_{MK} = (\lambda^L_{MK})^* (D^L_{MK})^* = \sum_{L,M,K} (-1)^{M-K} (\lambda^L_{MK})^* D^L_{-M-K} \tag{2.66}$$

where we have used the property of Wigner functions that $(D^L_{MK})^* = (-1)^{M-K} D^L_{MK}$. Because the sum over M and K range from $-L$ to L, we may replace M and K with $-M$ and $-K$ on the right-hand side of equation 2.66 so that the potential expansion becomes

$$\sum_{L,M,K} \lambda^L_{MK} D^L_{MK} = \sum_{L,M,K} (-1)^{K-M} (\lambda^L_{-M-K})^* D^L_{MK}. \tag{2.67}$$

The equality of equation 2.67 must hold for each term in the sum, therefore we arrive at the following property of the potential expansion coefficients:

$$\lambda^L_{MK} = (-1)^{K-M} (\lambda^L_{-M-K})^*. \tag{2.68}$$

Equation 2.68 shows that as a consequence of restricting the potential to be real-valued, there are only certain terms that are allowed in the expansion of equation 2.64. Specifically, the only terms that need to be considered are those with nonnegative M and those with nonnegative values of K when $M = 0$. Furthermore, equation 2.68 shows that all terms with $M = K = 0$ must have real-valued coefficients λ^L_{00}.

Substituting the potential expansion of equation 2.64 into equation 2.18, and using the results of operating on the Wigner functions with the angular momentum operators as given in equation 2.48, the linear term of the potential-dependent part of the diffusion operator is

$$\begin{aligned}\mathit{\Gamma}_1(\boldsymbol{\Omega}) = -\sum_{L,M,K} D^L_{MK}\Big[&R_\mathrm{d} N^+_{L,K-1} N^+_{L,K-2}\lambda^L_{M,K-2} \\ &+ R_\mathrm{d} N^+_{L,K+1} N^-_{L,K+2}\lambda^L_{M,K+2} \\ &+ \left[R_\perp(L(L+1)-K^2) + R_\parallel K^2\right]\lambda^L_{MK}\Big]\end{aligned} \tag{2.69}$$

where the $N^\pm_{L,K}$ constants are shorthand notation for the following [27, 37]:

$$N^\pm_{L,K} = \sqrt{(L \mp K)(L \pm K + 1)}. \tag{2.70}$$

Substitution of equation 2.64 into equation 2.20 allows for the derivation of the quadratic term of the potential-dependent part of the diffusion operator, which yields the expression

$$\begin{aligned}\mathit{\Gamma}_2(\boldsymbol{\Omega}) = &\sum_{L=|L_1-L_2|}^{L_1+L_2} (2L+1)(-1)^{K_1+K_2-M_1-M_2} D^L_{M_1+M_2,K_1+K_2} \\ &\times \sum_{L_1,M_1,K_1}\sum_{L_2,M_2,K_2} \lambda^{L_1}_{M_1,K_1}\lambda^{L_2}_{M_2,K_2}\begin{pmatrix} L_1 & L & L_2 \\ M_1 & -M & M_2\end{pmatrix} \\ &\times \Bigg[R_\mathrm{d} N^+_{L_1,K_1} N^+_{L_2,K_2}\begin{pmatrix} L_1 & L & L_2 \\ K_1+1 & -K & K_2+1\end{pmatrix} \\ &+ R_\mathrm{d} N^-_{L_1,K_1} N^-_{L_2,K_2}\begin{pmatrix} L_1 & L & L_2 \\ K_1-1 & -K & K_2-1\end{pmatrix} \\ &+ R_\perp N^+_{L_1,K_1} N^-_{L_2,K_2}\begin{pmatrix} L_1 & L & L_2 \\ K_1+1 & -K & K_2-1\end{pmatrix} \\ &+ R_\parallel K_1 K_2 \begin{pmatrix} L_1 & L & L_2 \\ K_1 & -K & K_2\end{pmatrix}\Bigg]\end{aligned} \tag{2.71}$$

.

The symmetrized rotational diffusion operator can be separated into a potential-independent term and potential-dependent term as in equation 2.13. Equations 2.17 to 2.20 express the potential-dependent components in terms of the total angular momentum operator and the elements of the rotational diffusion tensor. In the basis of Wigner functions, the potential-dependent part of the rotational diffusion superoperator can be expanded as

$$\hat{\hat{\mathit{\Gamma}}}_U = \sum_{LMK} X^L_{MK} D^L_{MK} \tag{2.72}$$

where the expansion coefficients X^L_{MK} are derived from the potential expansion coefficients λ^L_{MK} and the rotational diffusion tensor elements [27]. For a general orienting potential, the X^L_{MK} are

$$\begin{aligned}
X^L_{MK} = &-\frac{1}{2}\Big[R_{\mathrm{d}}\lambda^L_{M,K+2}N^-_{L,K+1}N^-_{L,K+2} + R_{\mathrm{d}}\lambda^L_{M,K-2}N^+_{L,K-1}N^+_{L,K-2} \\
&+ R_\perp\lambda^L_{MK}\left(L\left(L+1\right)-K^2\right) + R_\parallel\lambda^L_{MK}K^2\Big] \\
&- \frac{1}{4}\left(2L+1\right)\left(-1\right)^{K-M}\sum_{L_1,M_1,K_1}\sum_{L_2,M_2,K_2}\lambda^{L_1}_{M_1,K_1}\lambda^{L_2}_{M_2,K_2}\begin{pmatrix} L_1 & L & L_2 \\ M_1 & -M & M_2\end{pmatrix} \\
&\times\left[R_{\mathrm{d}}N^+_{L_1,K_1}N^+_{L_2,K_2}\begin{pmatrix} L_1 & L & L_2 \\ K_1+1 & -K & K_2+1\end{pmatrix}\right. \\
&+ R_{\mathrm{d}}N^-_{L_1,K_1}N^-_{L_2,K_2}\begin{pmatrix} L_1 & L & L_2 \\ K_1-1 & -K & K_2-1\end{pmatrix} \\
&+ R_\perp N^+_{L_1,K_1}N^-_{L_2,K_2}\begin{pmatrix} L_1 & L & L_2 \\ K_1+1 & -K & K_2-1\end{pmatrix} \\
&\left.+ R_\parallel K_1K_2\begin{pmatrix} L_1 & L & L_2 \\ K_1 & -K & K_2\end{pmatrix}\right]
\end{aligned} \tag{2.73}$$

where R_{d}, $R_\perp$, and $R_\parallel$ are defined in equation 2.14, and the constants $N^\pm_{L,K}$ are defined in equation 2.70.

Given the expansion in equation 2.72, the rotational diffusion superoperator can be written as

$$\hat{\hat{\Gamma}} = \hat{\hat{\Gamma}}_0 + \hat{\hat{\Gamma}}_U = \hat{\hat{\Gamma}}_0 + \sum_{LMK} X^L_{MK}D^L_{MK}. \tag{2.74}$$

In the direct product basis of equation 2.49, the matrix elements of the symmetrized rotational diffusion superoperator are then

$$\begin{aligned}
\hat{\hat{\Gamma}}_{ip,jq} = \langle\chi_p\sigma_i|\,\hat{\hat{\Gamma}}\,|\chi_q\sigma_j\rangle = \langle\sigma_i|\sigma_j\rangle &\left[\langle\chi_p|\,\hat{\hat{\Gamma}}_0\,|\chi_q\rangle + \sum_{LMK} X^L_{MK}\,\langle\chi_p|\,D^L_{MK}\,|\chi_q\rangle\right] \\
= \delta_{i,j}&\left[\langle\chi_p|\,\hat{\hat{\Gamma}}_0\,|\chi_q\rangle + \sum_{LMK} X^L_{MK}\,\langle\chi_p|\,D^L_{MK}\,|\chi_q\rangle\right].
\end{aligned} \tag{2.75}$$

Note that the diffusion superoperator does not operate on the spin component of the basis functions and therefore can only have nonzero elements when $\sigma_i = \sigma_j$.

Exact expressions for the matrix elements of $\hat{\hat{\Gamma}}$ can be derived using equations 2.16, 2.18, and 2.20 along with the angular momentum operator eigenfunction properties 2.48. The resulting expressions from these derivations are presented in equations 2.16, 2.69, and 2.71. The special case of isotropic rotational diffusion in the absence of an orienting potential is straightforward and will be discussed here because this case applies to a large portion of actual EPR samples in solution.

In the special case of isotropic rotational diffusion, the diffusion tensor is diagonal in any frame of reference and has the form

$$R = \begin{bmatrix} R & 0 & 0 \\ 0 & R & 0 \\ 0 & 0 & R \end{bmatrix} . \tag{2.76}$$

Therefore, the diffusion tensor can be reduced to a single diffusion constant R, which according to the Stokes-Einstein equation is

$$R = \frac{1}{l(l+1)\tau_\mathrm{c}} = \frac{1}{6\tau_\mathrm{c}} \tag{2.77}$$

where τ_c is the rank-2 ($l = 2$) rotational correlation time that parameterizes the effect of rotational motion on the CW EPR lineshape [17]. Given the diffusion constant of equation 2.77, for the case of isotropic rotational diffusion, the only nonzero matrix elements of $\hat{\hat{\Gamma}}$ are those in which $\chi_p = \chi_q$, or $L_p = L_q = L$, $M_p = M_q = M$, and $K_p = K_q = K$ [37]:

$$\langle LMK\sigma_i| \, \hat{\hat{\Gamma}} \, |LMK\sigma_j\rangle = RL(L+1)\delta_{\sigma_i,\sigma_j} . \tag{2.78}$$

2.7.3 The starting vector

In general, the elements of the starting vector are

$$\langle\chi\sigma|\hat{S}_x P_\mathrm{eq}^{1/2}\rangle = \langle\sigma|\hat{S}_x\rangle \, \langle\chi|P_\mathrm{eq}^{1/2}\rangle = \langle\sigma|\hat{S}_x\rangle \sqrt{\frac{2L+1}{8\pi^2}} \int \mathrm{d}\boldsymbol{\Omega}(D_{MK}^L)^* P_\mathrm{eq}^{1/2} \tag{2.79}$$

where P_{eq} is the orientation-dependent equilibrium orientational distribution of the molecules in the sample. Recall from equation 2.3 that the orientation-dependence of P_{eq} is due to the orienting potential $U(\boldsymbol{\Omega})$ which was defined in equation 2.64. In the absence of an orienting potential, the equilibrium orientational distribution is completely isotropic and the matrix elements of the starting vector can be easily constructed from the columns of the Hilbert space $\hat{S}_x$ operator. However, if the system has some orienting potential, then the starting vector elements are more complex and the integral in equation 2.79 is likely to require numerical calculation [27, 22].

With the expressions for the matrix elements of $\hat{\hat{H}}$ in equation 2.63, $\hat{\hat{\Gamma}}$ in equation 2.75, and $\hat{S}_x P_{\mathrm{eq}}^{1/2}$ in equation 2.79, the spectral lineshape function of equation 2.39 can be calculated to simulate slow-motion CW EPR spectra for general spin systems.

2.8 Frequency-to-field conversion

2.8.1 Separation of field-dependent interactions

The SLE lineshape $I(\omega)$ of equation 2.39 is expressed as a function of a sweep over the incoming microwave frequency ω, however in practice almost all CW EPR experiments are performed by irradiating the sample with a constant microwave frequency and sweeping the external B_0 field strength. The lineshape function could then be written as

$$I(B_0) = \langle \hat{S}_x P_{\mathrm{eq}}^{1/2} | \big(-\mathrm{i}\hat{\hat{H}}_0(B_0) - \omega_0 \hat{\hat{\mathrm{I}}} + \hat{\hat{\Gamma}} \big)^{-1} | \hat{S}_x P_{\mathrm{eq}}^{1/2} \rangle \tag{2.80}$$

where B_0 is the instantaneous external field strength and ω_0 is the microwave frequency. The frequency-dependent lineshape function of equation 2.39 is easier to calculate because it depends only on a single Hamiltonian whereas the field-dependent lineshape function must be calculated with a unique Hamiltonian at each field point. Various methods have been developed to quickly and accurately solve the frequency-dependent lineshape function, such as the tridiagonal Lanczos and conjugate gradient methods [25, 21, 22, 49]. In these methods, a single Hamiltonian is constructed using just one B_0 field value, usually chosen to be the resonance field that corresponds to the experimental microwave frequency and some chosen g-value. Using this single Hamiltonian, a frequency-sweep spectrum can be rapidly calculated according to one of the above methods. The frequency axis of this spectrum is then converted artificially to a field axis via the resonance condition

$$B = \frac{h\omega}{2\pi\mu_{\mathrm{B}}g_{\mathrm{con}}} \tag{2.81}$$

where g_{con} is a single g-value used for the frequency-to-field conversion, usually chosen to be the mean g-value of the sample, $\bar{g}$. This approximation of the field sweep experiment is reasonable for relatively narrow spectra such as nitroxides, but fails to adequately reproduce the correct line positions and spectral widths of systems with highly anisotropic g-tensors.

An explicit field sweep simulation can be performed simply by constructing the spin Hamiltonian for each field point and calculating the lineshape function for each Hamiltonian. However, the rapid numerical methods that solve the frequency-dependent lineshape function of equation 2.39 cannot be employed for the field-dependent lineshape function of equation 2.80 because the Hamiltonian is not constant. For small to moderately sized spin systems, the bottleneck of an explicit field sweep simulation can be in the calculation of the spin Hamiltonian elements rather than the solution of the lineshape function. However, the spin Hamiltonian need not be calculated from scratch for each field point. Instead, the Hamiltonian can be decomposed into two parts

$$\hat{\hat{H}}_0 = \hat{\hat{H}}_0^G + \hat{\hat{H}}_0^B \tag{2.82}$$

where H_0^G contains all the field-independent interactions (hyperfine, zero-field splitting, nuclear quadrupole, etc.) and H_0^B contains the field-dependent electron and nuclear Zeeman interactions. Both H_0^G and H_0^B need only be calculated once, with H_0^B being calculated in a per Tesla fashion. Then, for each unique field point, the overall spin Hamiltonian is simply

$$\hat{\hat{H}}_0(B) = \hat{\hat{H}}_0^G + B \cdot \hat{\hat{H}}_0^B. \tag{2.83}$$

In the general method for implementing the stochastic Liouville equation presented above, interaction with the external field B_0 is captured in the formation of the vector operator ISTOs $\hat{\boldsymbol{T}}^{(0)}$ and $\hat{\boldsymbol{T}}^{(2)}$ and subsequent construction of the RBOs. To separate the Hamiltonian into field-dependent and field-independent terms as in equation 2.83, the RBOs from which the Hamiltonian elements are calculated are separated into field-dependent and field-independent RBOs. Therefore there are 52 RBOs in total for an explicit field sweep simulation - 2 isotropic RBOs (one field-dependent and one field-independent) and 50 anisotropic RBOs (25 field-dependent and 25 field-independent).

2.8.2 Error due to the frequency-to-field conversion

In the frequency-to-field conversion process, only a single spin Hamiltonian is calculated, which corresponds to a single B_0 field value. The value of B_0 used to calculate the spin Hamiltonian $\hat{H}(B_{\text{calc}})$ is called B_{calc}. For a S = 1/2 spin system with only electron Zeeman interaction, the field value B_{calc} must be related to the true experimental microwave frequency ν_{mw} through some choice of g-value such that

$$B_{\text{calc}} = \frac{h\nu_{\text{mw}}}{\mu_{\text{B}} g_{\text{calc}}} = \frac{h\nu_{\text{res}}}{\mu_{\text{B}} g} \tag{2.84}$$

where g is the actual g-value that results in a resonance frequency at the field value B_{calc}. Therefore any potential resonance frequency can be related to the experimental microwave frequency via

$$\nu_{\text{res}} = \frac{g}{g_{\text{calc}}} \nu_{\text{mw}}. \tag{2.85}$$

For each value of ω that is used to calculate $I(\omega)$, if a resonance were to occur at that frequency, the error in the predicted resonance field compared to the actual resonance field is

$$\mathit{\Delta}_B = \tilde{B}_{\text{res}} - B_{\text{res}} \tag{2.86}$$

where $\tilde{B}_{\text{res}}$ is the field at which a resonance is predicted to occur and B_{res} is the field at which the resonance would truly occur. These two field values are given by

$$B_{\text{res}} = \frac{h\nu_{\text{mw}}}{\mu_{\text{B}}} \qquad \text{and} \qquad \tilde{B}_{\text{res}} = B_{\text{calc}} - \frac{\partial B_{\text{calc}}}{\partial \nu_{\text{res}}} \left(\nu_{\text{res}} - \nu_{\text{mw}}\right) \tag{2.87}$$

where we have used $\omega = 2\pi\nu$. Substituting equation 2.84 and the frequency derivative of equation 2.84 into equation 2.87 gives for the approximate resonance field:

$$\tilde{B}_{\text{res}} = \frac{h\nu_{\text{mw}}}{\mu_{\text{B}} g_{\text{calc}}} \left(2 - \frac{g}{g_{\text{calc}}}\right). \tag{2.88}$$

If the g-value used to convert ν_{res} to a field axis value is $g_{\text{con}} = g_{\text{calc}}$, then according to equation 2.86 the error in the predicted resonance field is

$$\varDelta_B = \frac{h\nu_{\mathrm{mw}}}{\mu_{\mathrm{B}} g_{\mathrm{calc}}}\left(2 - \frac{g}{g}\right) - \frac{h\nu_{\mathrm{mw}}}{\mu_{\mathrm{B}} g} = -\frac{h\nu_{\mathrm{mw}}}{\mu_{\mathrm{B}} g_{\mathrm{calc}}}\left(\frac{(g - g_{\mathrm{calc}})^2}{g g_{\mathrm{calc}}}\right) = -B_{\mathrm{calc}}\frac{\varDelta_g^2}{g g_{\mathrm{calc}}} \tag{2.89}$$

where $\varDelta_g = g - g_{\mathrm{calc}}$ is the difference between the g-value used to calculate the spin Hamiltonian and the actual g-value that the system would need to have in order to have a resonance at the desired field point given the experimental microwave frequency ν_{mw}. The field sweep error is quadratic in the g-value error, which becomes important for systems with highly anisotropic g-tensors that have resonances for orientations in which the corresponding g-values differ significantly from g_{calc}.

2.9 Conclusions

A procedure has been presented by which the SLE equation 2.32 and subsequent solution of the lineshape function equation 2.39 may be implemented in a general fashion for systems that have spin Hamiltonians with any number or nature of interaction terms. The key to this general implementation is in the construction of the ISTOs and RBOs from the familiarly defined lab frame spin vector operators and molecular frame Cartesian interaction tensors. From the RBOs and the choice of spatial basis (in this case, the generalized spherical harmonics) the elements of the Hamiltonian superoperator may be calculated. Given a choice of spatial basis and a rotational diffusion model, the elements of the rotational diffusion superoperator may also be calculated. Once the calculation of the elements of $\hat{\hat{H}}$ and $\hat{\hat{\varGamma}}$ is complete, the spectral lineshape function can be evaluated to simulate CW EPR lineshapes.

Chapter 3

MULTI-NUCLEAR SYSTEM: NITRONYL NITROXIDES

One of the initial applications of the general SLE solver was a collaboration with Dr. Joshua Biller from Dr. Sandra Eaton's lab at University of Denver in Colorado. The Eaton group studies the relaxation properties of nitronyl nitroxides [50, 51] for use as possible substitutes for nitroxides in pulse EPR experiments. Nitronyl nitroxides were first synthesized in the 1960s [52, 53, 54] and their magnetic properties and use as spin labels were studied soon thereafter [55, 56]. Nitronyl nitroxides are organic $S = 1/2$ systems in which the unpaired electron is delocalized over two separate NO bonds. The EPR spectra of nitronyl nitroxides are more complex than nitroxides because of the double hyperfine splitting from two nitrogen nuclei rather than one, but the longer relaxation times of nitronyl nitroxides can potentially allow for longer distance measurements in pulse EPR experiments [57, 58, 59, 60].

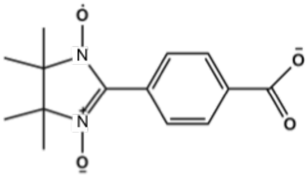

Figure 3.1: Structure of 2-(4-carboxy-phenyl)-4,4,5,5-tetramethylimidazoline-3-oxide-1-oxyl, the nitronyl nitroxide used to model multi-nuclear hyperfine effects on a slow-tumbling $S = 1/2$ system.

The nitronyl nitroxide shown in figure 3.1, 2-(4-carboxy-phenyl)-4,4,5,5-tetramethylimidazoline-3-oxide-1-oxyl (hereafter referred to as the nitronyl nitroxide), was synthesized by Dr. Biller and CW EPR spectra were measured by him at X-band and Q-band. Previous attempts at simulating experimental nitronyl nitroxide spectra in the slow-motion regime gave poor fits to the experimental data, therefore those fits could not be used to determine rotational correlation times for this compound. Dr. Biller wanted to know if the hyperfine splittings due to hydrogen atoms within the molecule were significant enough to warrant inclusion in the simulations in order to obtain good fits. Using the general SLE solver introduced in

Chapter 2, multiple hyperfine interactions from both nitrogen nuclei and hydrogen nuclei were able to be incorporated into simulations to investigate this question.

3.1 Nitronyl nitroxide spin system

Nitronyl nitroxides have a single unpaired electron with appreciable spin density on two nitrogen nuclei. In most cases, both nitrogens are the nitrogen-14 isotope. The spin Hamiltonian for a system with $S = 1/2$, $I_1 = 1$, and $I_2 = 1$ is

$$\hbar\hat{H} = \mu_{\mathrm{B}}\boldsymbol{B} \cdot g \cdot \hat{\boldsymbol{S}} \ + \ \hat{\boldsymbol{S}} \cdot A_1 \cdot \hat{\boldsymbol{I}}_1 \ + \ \hat{\boldsymbol{S}} \cdot A_2 \cdot \hat{\boldsymbol{I}}_2 \tag{3.1}$$

where the first term is the electron Zeeman interaction and the other two terms are the hyperfine interactions between the electron and each of the two nitrogen nuclei. The nuclear Zeeman interactions are negligible compared to the electron Zeeman and hyperfine interactions, so the nuclear Zeeman terms need not be explicitly included in the spin Hamiltonian of equation 3.1.

An energy diagram corresponding to the spin Hamiltonian in equation 3.1 is shown in figure 3.2. Due to the double hyperfine interaction with the $I = 1$ nuclei, there are 18 different spin states $|m_S, m_{I1}, m_{I2}\rangle$ and 9 allowed transitions in which $\Delta m_S = \pm 1$ and $\Delta\left(m_{I1} + m_{I2}\right) = 0$. If the hyperfine splitting due to each nitrogen-14 nucleus is equivalent, then within each electronic spin manifold ($m_S = +1/2$ and $m_S = -1/2$) there are degeneracies in the energies of states that have the same sum of nuclear spin states $m_{I1} + m_{I2}$. These degeneracies are listed in table 3.1.

Table 3.1: The number of degenerate spin states for all possible values of $m_{I1} + m_{I2}$ within a single electron spin manifold for a nitronyl nitroxide.

$m_{I1} + m_{I2}$	2	1	0	-1	-2
Degeneracy	1	2	3	2	1

As a result of the splitting pattern in figure 3.2, a typical liquid-state nitronyl nitroxide spectrum in the isotropic limit consists of 5 lines with a 1:2:3:2:1 intensity ratio pattern along the field sweep axis. The simulated isotropic nitronyl nitroxide spectrum in figure 3.3 illustrates this lineshape using a spin Hamiltonian like the one in equation 3.1.

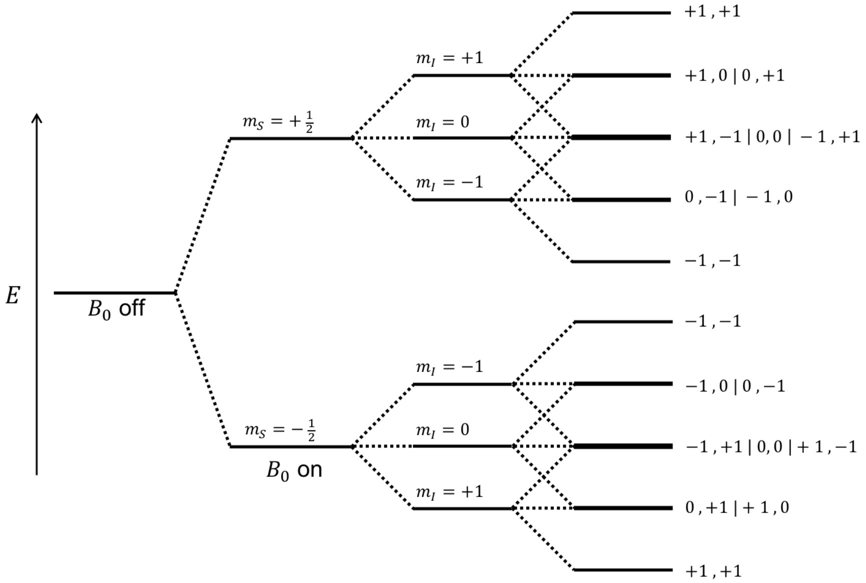

Figure 3.2: Energy level diagram for a single orientation of a nitronyl nitroxide radical ($S = 1/2$, $I_1 = 1$, $I_2 = 1$) with identical hyperfine splitting from each nitrogen-14 nucleus ($A_1 = A_2$). The nuclear Zeeman interaction is neglected, so the energy level splittings are due to the hyperfine interaction only. The labels to the right of the energy levels represent all combinations of m_{I1} and m_{I2} that result in a spin state at that energy. The splittings here are meant to be illustrative and not to scale.

3.2 CW EPR spectra

Two sets of experimental X-band and Q-band CW EPR data for the nitronyl nitroxide in figure 3.1 were provided by Dr. Joshua Biller from University of Denver (unpublished) for the purpose of fitting the spin Hamiltonian parameters and rotational correlation times using the general SLE solver. These sets of data will be referred to as data set 1 and data set 2, with the sets numbered in chronological order of measurement.

Data set 1, shown in figure 3.4, consists of both X-band and Q-band spectra measured over a range of temperatures to determine the effect of sample viscosity on the CW lineshape and, therefore, the predicted rotational correlation time. All samples in data set 1 were 0.25 mM in concentration of nitronyl nitroxide and were prepared in 1:1 glycerol:water by volume solutions. The data set includes frozen spectra as well as motional spectra, with frozen spectra indicated by blue temperature labels in figure 3.4 and motional spectra indicated by red

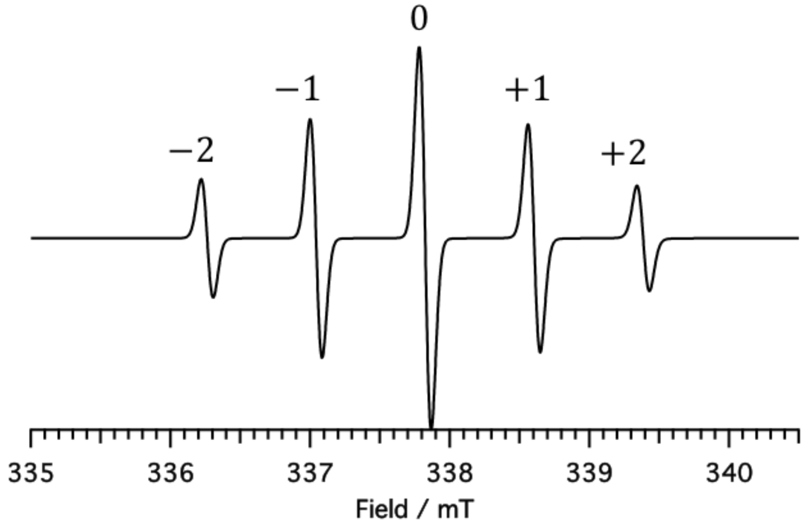

Figure 3.3: A simulated spectrum for a nitronyl nitroxide in the fast-motion limit ($\tau_\mathrm{c} = 10$ ps). There are five lines in a 1:2:3:2:1 intensity ratio. Labeled above each line is the sum of nuclear spin states $m_{I1} + m_{I2}$ for that transition. This sum must remain constant for the electronic spin state transition to be allowed (i.e. $\Delta\left(m_{I1} + m_{I2}\right) = 0$).

temperature labels. The frozen data was provided so that the g-tensor and A-tensor values in the spin Hamiltonian of equation 3.1 could be determined by fitting simulated powder lineshapes to the experimental spectra. Accurate values for spin Hamiltonian parameters are required if the τ_c values from slow-motion fits are to be reliable, but determination of spin Hamiltonian tensor values is difficult outside of the powder regime.

Many of the frozen spectra in data set 1 were unsuitable for accurate determination of the g-tensor and A-tensor values, as were the motional spectra for the determination of rotational correlation times. Many of the spectra were poorly phased, had baseline drifts and offsets, or appeared to exhibit saturation effects. Baseline correction is possible through data processing and phase offsets can be accounted for in powder simulations as an additional fit parameter, but saturation effects cannot be accounted for in my current implementation of the SLE model. Regardless, good raw data is preferable to processed data and introducing additional fit parameters in the model is undesirable. Evidence for baseline drift, improper microwave phasing, and saturation can be seen by constructing numerical integral plots of the measured spectra.

Figure 3.5 shows the processed data corresponding to the raw data shown in figure 3.4. To correct the baseline offset, the spectra in data set 1 were processed with a low-pass Savitsky-Golay filter using a window size of 20 to reduce noise and then linearly baseline-corrected using the the intensity values at the beginning and end of the field sweep. Any additional baseline drift in the integrals of the processed spectra (from baseline offset, for example) were then baseline-corrected directly in the integral plots in the same manner as the filtered data. The integral plots of the processed data in figure 3.5 are shown in figure 3.6. Integral plots of field-modulated CW EPR spectra are reminiscent of absorption spectra, and therefore, for a $S = 1/2$ system without any electron-electron spin effects, should have a zero baseline or linear baseline drift over the entire range of the field sweep. Most of the integral plots of the spectra in data set 1 do not exhibit this behavior.

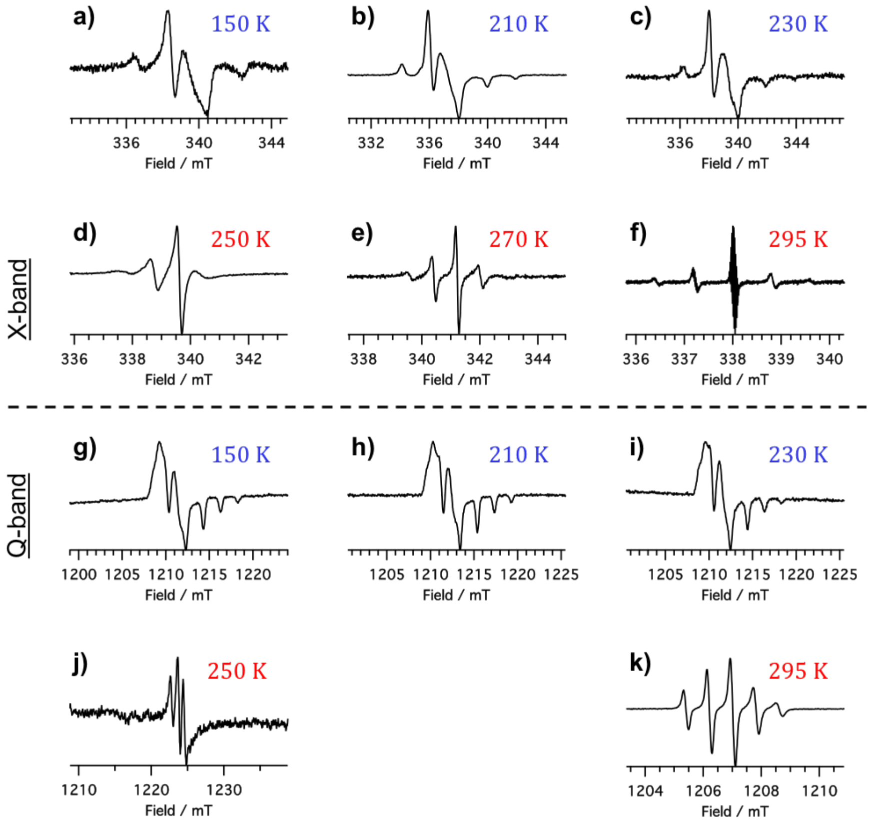

Figure 3.4: A set of experimental CW EPR spectra for the nitronyl nitroxide in figure 3.1. All samples were prepared in a 1:1 glycerol:water by volume solution and measured over a range of temperatures at both X-band and Q-band. Temperatures in blue indicate that the lineshape is that of a frozen sample. Red indicates that the lineshape is of a liquid sample and so is affected by rotational dynamics.

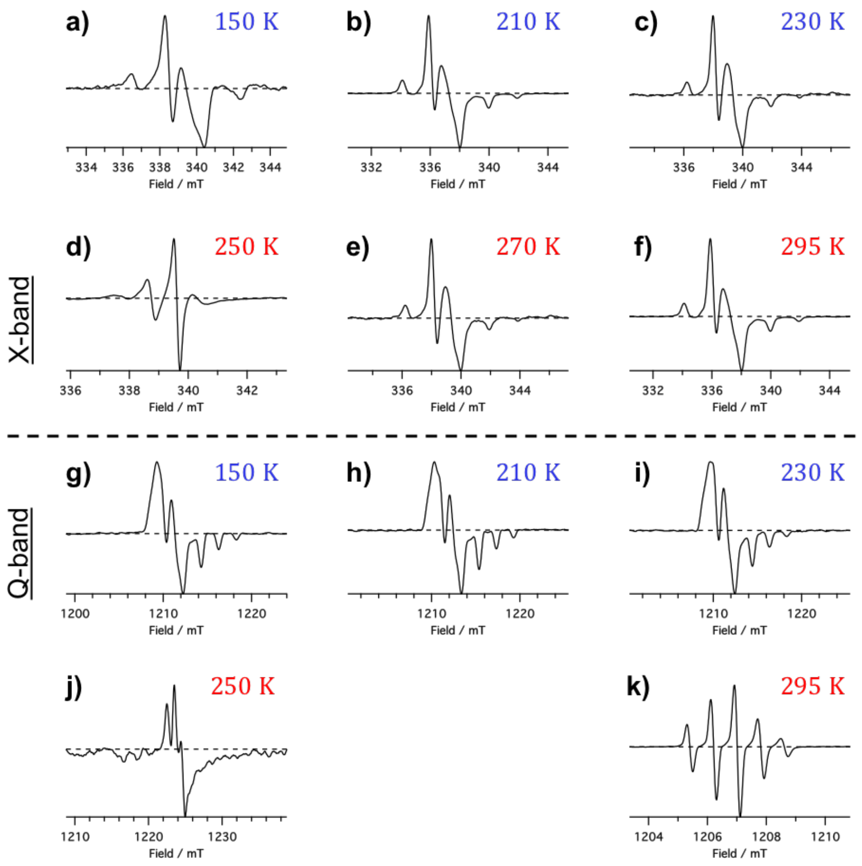

Figure 3.5: Processed spectra from data set 1. The spectra have been smoothed and baseline-corrected.

The processed integral plots in figure 3.6 suggest that, of the frozen spectra in data set 1, X-band spectrum **b** measured at 210 K and Q-band spectrum **i** measured at 230 K are good candidates for fitting accurate spin Hamiltonian parameters. Q-band spectra are preferable to X-band spectra for fitting g and A values because the higher fields at Q-band broaden the spectral width, which results in less overlap in the x, y, z components of the powder lineshape.

However, Q-band spectrum **i** exhibits some minor baseline drift and saturation or phasing issues while X-band spectrum **b** suffers only from an easily corrected baseline offset. Therefore, spectrum **b** was chosen to fit the powder lineshape according to the spin Hamiltonian in equation 3.1 in order to fit g-tensor and A-tensor values to use as parameters in the slow-motion simulations.

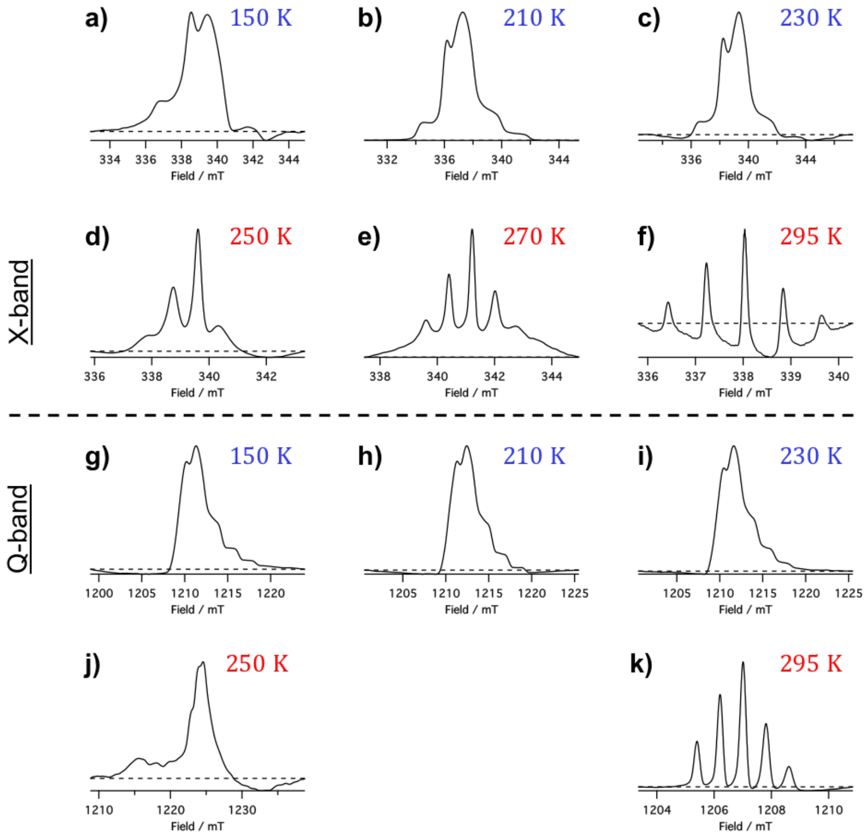

Figure 3.6: Data set 1 processed integrals. Many spectra have nonlinear baselines, which may be due to saturation or improper microwave phasing.

The integral plots of the motional spectra of data set 1 in figure 3.6 (spectra **d**, **e**, **f**, **j**, and **i**) all exhibit baseline, phasing, or saturation issues as well and are therefore not ideal for the fitting of rotational correlation times. To provide better data for fitting rotational correlation times to slow-motion lineshapes, a second data set was measured. The raw and processed spectra, as well as their integral plots, are shown in figure 3.7. Both spectra in data set 2 were the same concentration in nitronyl nitroxide (exact concentration not provided) and both were measured at room temperature at X-band. Viscosity was varied between the samples by adjusting the concentration of glycerol in the water-glycerol solvent. The sample corresponding to spectrum **a** was 75% glycerol by volume and the sample corresponding to spectrum **b** was 88% glycerol by volume.

The motional spectra in data set 2 are of very high quality, as evidenced by the integral plots of the unprocessed data, which are nearly identical to the processed integral plots. These spectra, along with spectrum **b** of data set 1, were sufficient to fit the spin Hamiltonian parameters and rotational correlation time X-band nitronyl nitroxide data.

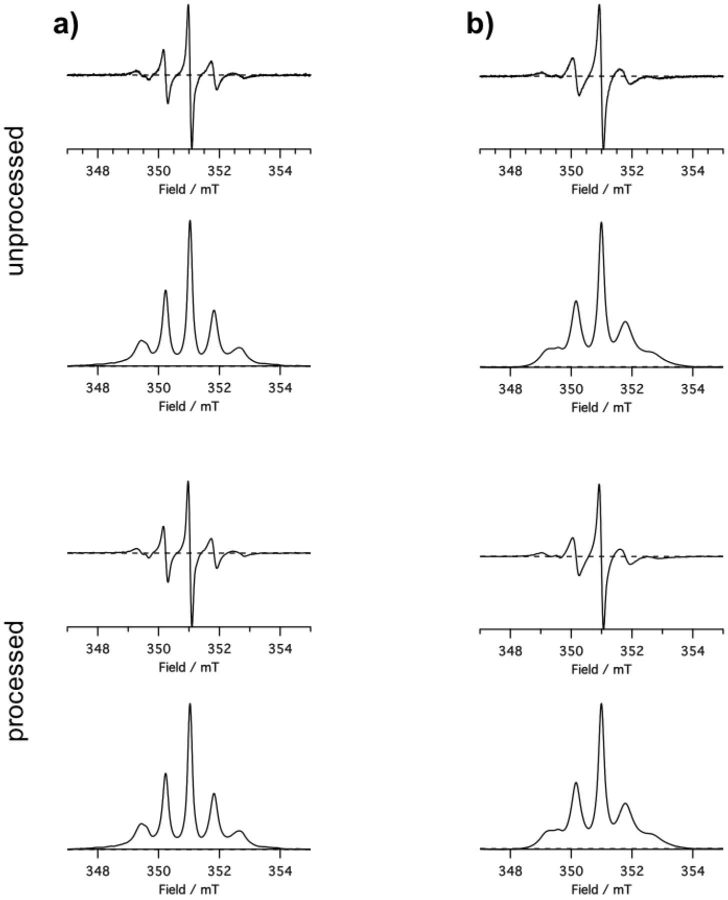

Figure 3.7: Data set 2, room temperature. a) 75% glycerol. b) 88% glycerol.

3.3 *Powder spectrum simulations*

3.3.1 Quantum chemistry calculations

Spin Hamiltonian models for ordinary nitroxides ($S = 1/2$, $I = 1$) usually assume that the electron Zeeman frame (or g-frame) and the hyperfine frame (or A-frame) are collinear (i.e. both tensors have the same eigenframe orientation), which is a good approximation for nitroxides. However, this is not the case for nitronyl nitroxides, which have two distinct A-frames, neither of which are collinear with the g-frame nor with each other [58].

In order to incorporate the relative orientations of these three molecular frames in the powder lineshape simulations, preliminary density functional theory (DFT) calculations were performed on the nitronyl nitroxide anion in figures 3.1 and 3.8 to provide an initial guess for the best-fit g-frame and A-frame orientations.

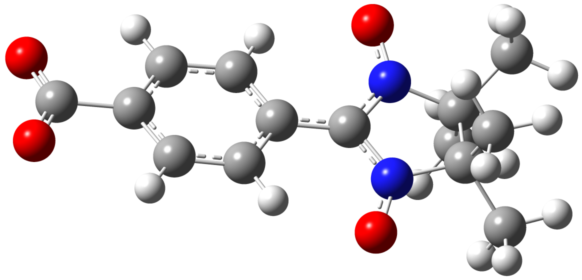

Figure 3.8: A view of the optimized geometry of the nitronyl nitroxide, calculated using Hartree-Fock theory with the 6-31+G(d,p) basis set. The two rings are essentially coplanar. Grey atoms represent carbons, white atoms represent hydrogens, red atoms represent oxygens, and blue atoms represent nitrogens.

An initial geometry optimization was done using the Gaussian 09 quantum chemistry software package at the Hartree-Fock level of theory with the 6-31+G(d,p) basis set [61]. The initial guess geometry had both rings coplanar. No solvent effects were included in the geometry optimization. The optimized geometry is shown in figure 3.8. The optimized atomic Cartesian coordinates from the structure in figure 3.8 were then used to calculate magnetic tensor properties using the ORCA version 3.0.1 quantum chemistry software package [62]. Magnetic tensor calculations in ORCA were performed using density functional theory (DFT) with the B3LYP functional and the same basis set used in the geometry optimization calculations, also without the incorporation of any solvent effects.

3.3.2 Best-fit simulation parameters

To fit the experimental slow-motion spectra, accurate estimates for the spin Hamiltonian interaction tensors g, A_1, and A_2 were needed for the nitronyl nitroxide under study. The standard method for obtaining these parameters for any compound is to measure a rigid-limit spectrum and then fit a simulated powder lineshape to that spectrum by varying the relevant spin Hamiltonian parameters until the misfit error is minimized. Spectrum **b** from data set 1 in figure 3.4 was used to fit the spin Hamiltonian parameters. Figure 3.9 shows the powder simulation fit to this spectrum.

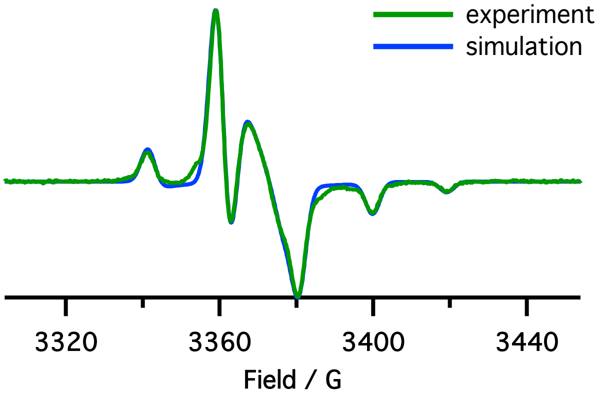

Figure 3.9: The g-values, A-values, and tilt angles between the g-frame and A-frame for the slow-motion fits of the nitronyl nitroxide were obtained by fitting a simulated powder spectrum to frozen X-band spectrum **b** from data set 1. The magnetic field is in units of gauss (10 G = 1 mT).

The powder simulation in figure 3.9 has the spin Hamiltonian of equation 3.1 and incorporates g- and A-tensors that are tilted with respect to each other. Initial values for the tensors were obtained from a text on the properties of imidazole nitroxides [63] and initial values for the tensor orientations were obtained from the ORCA quantum chemistry calculations as discussed above. The principal values of each A-tensor were assumed to be equivalent due to the symmetry of the imidazole ring and delocalization of the unpaired electron over both NO bonds. A convolutional Gaussian line broadening was also included to match the experimental linewidths, which can be attributed to unresolved hyperfine couplings with other magnetic nuclei in the molecule and in the solvent. The best-fit parameters are listed in tables 3.2 and 3.3. The g-values of the nitronyl nitroxide are similar to those for nitroxides. However, the hyperfine splitting in nitronyl nitroxides is about half as strong as that typically observed for nitroxide radicals, which is due to delocalization of the unpaired electron over two NO bonds rather than being localized on a single NO bond.

Table 3.2: EPR properties of the nitronyl nitroxide obtained from the powder fit to X-band spectrum **b** from data set 1. The A-values are identical for both hyperfine tensors (i.e. $A_1 = A_2 = A$). These parameters were used in the slow-motion simulations to fit rotational correlation times for this compound.

g_x	g_y	g_z	A_x / MHz	A_y / MHz	A_z / MHz	linewidth / mT
2.0113	2.0069	2.0025	2.23	4.97	54.39	0.427

Table 3.3: Best-fit tensor orientation angles, in radians. The angles define an Euler rotation that brings an origin reference frame into the frame in which the respective tensors are diagonal. The origin is the molecular frame, which has the z-axis in the plane of the two rings and the x- and y-axes perpendicular to that plane.

	g	A_1	A_2
α	1.100	1.376	1.129
β	0.142	1.630	1.483
γ	2.101	-3.076	-0.164

3.4 *Slow-motion spectrum simulations*

3.4.1 Modeling hydrogen hyperfine interactions

Given the experimentally determined nitronyl nitroxide EPR properties listed in tables 3.2 and 3.3, the general SLE solver made it possible to attempt to answer questions about nitronyl nitroxides in the slow-motion regime that could not previously be investigated. In particular, nitronyl nitroxides pose the problem of having multiple significant hyperfine interactions - at least two due to the nitrogen nuclei and more if hyperfine interactions with any of the hydrogen nuclei are to be explicitly accounted for. In this case, previous slow-motion fits were poor due to the lack of a slow-motion model that could incorporate hyperfine interactions with multiple magnetic nuclei. We were interested in whether hyperfine interactions with hydrogen nuclei on the phenyl ring could be contributing to the slow-motion lineshape even though those hyperfine splittings are not resolved in the frozen spectrum. The general SLE solver was well-suited to study this because it can accommodate any number of spin Hamiltonian interactions (within computational feasibility).

The slow-motion spectra provided in data set 2 were used to investigate the effect of hydrogen hyperfine coupling on the slow-motion lineshape as well as to compare rotational correlation times in solutions of differing viscosity. These spectra are shown again in figure 3.10.

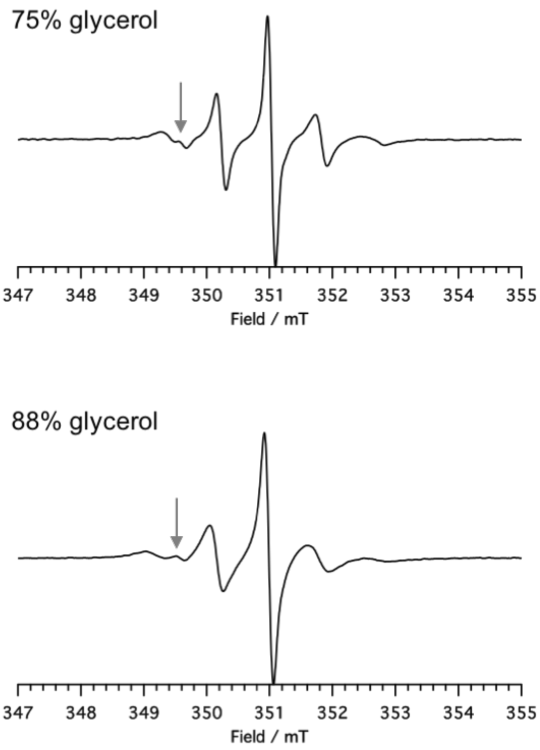

Figure 3.10: Slow-motion X-band nitronyl nitroxide spectra. Both samples were measured at room temperature in glycerol:water solutions. The top spectrum is in 75% glycerol and the bottom spectrum is in 88% percent glycerol. Both spectra have an unexpected low-field feature at about 349.5 mT, which is labeled with the grey arrows.

Both spectra in figure 3.10 exhibit an unexpected low-field feature that should not appear given the nitronyl nitroxide spin Hamiltonian of equation 3.1. However, although of poor quality, the motional spectra from data set 1 in figures 3.4 and 3.5 do not have this feature. The nature of this feature was also explored.

A slow-motion fit of the 75% glycerol spectrum using the properties in tables 3.2 and 3.3 that include only the two nitrogen hyperfine interactions are shown in figure 3.11. The rotational correlation time of the fit τ_c is 0.623 ns. Other than the low-field feature, the fit is quite good even without explicit modeling of any of the hydrogen hyperfine interactions.

To model the hydrogen hyperfine interactions, additional hyperfine terms for the hydrogen nuclei were explicitly included in the spin Hamiltonian and the generic Gaussian convolutional broadening omitted from the simulations so as not to doubly account for possible broadening due to hydrogen hyperfine interactions. A series of simulations was performed in which hydrogen hyperfine terms were included in the spin Hamiltonian, from no hydrogens to as many as three hydrogens. Including the hydrogen hyperfine interactions in the spin Hamiltonian gives the Hamiltonian the following form:

$$\hbar \hat{H}_{n\mathrm{H}} = \mu_{\mathrm{B}} \boldsymbol{B} \cdot g \cdot \hat{\boldsymbol{S}} \; + \; \hat{\boldsymbol{S}} \cdot A_{\mathrm{N}_1} \cdot \hat{\boldsymbol{I}}_{\mathrm{N}_1} \; + \; \hat{\boldsymbol{S}} \cdot A_{\mathrm{N}_2} \cdot \hat{\boldsymbol{I}}_{\mathrm{N}_2} \; + \; \hat{\boldsymbol{S}} \cdot \sum_{i=0}^{n} A_{\mathrm{H}_n} \cdot \hat{\boldsymbol{I}}_{\mathrm{H}_n} \tag{3.2}$$

where n is the number of hydrogens that were explicitly included in the simulation. Beyond three hydrogens, the dimensionality of the SLE grows too high to complete the calculations in a reasonable amount of time due to the large size the direct product basis set.

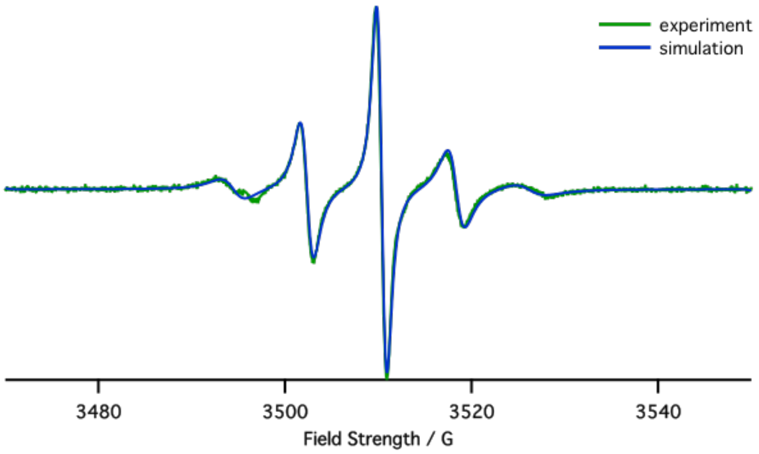

Figure 3.11: Nitronyl nitroxide slow-motion fit obtained from the general SLE solver. The simulation parameters include those listed in tables 3.2 and 3.3 as well as a best-fit rotational correlation time $\tau_{\mathrm{c}} = 0.623$ ns.

According to the structure of the nitronyl nitroxide in figure 3.1, there are three distinct types of hydrogen nuclei in the molecule: twelve methyl hydrogens, two *ortho*- phenyl hydrogens, and two *meta*- phenyl hydrogens. Each of these types of hydrogen nuclei were included sequentially in the simulations. Figure 3.12 shows how the lineshape changes as hydrogens are added to the simulation. A simulation with a Gaussian convolutional broadening of 2.35 MHz in lieu of explicit hydrogen hyperfine interaction terms is also shown for comparison.

From relaxation studies done by Dr. Joshua Biller, the hyperfine splittings from the hydrogen nuclei are estimated to be on the order of 1 to 2 MHz (unpublished, personal correspondence), with the *ortho*- hydrogens having the strongest couplings and the the methyl hydrogens having the weakest couplings. The trend in figure 3.12 shows a progressive line broadening of the nitrogen peaks as more hydrogen nuclei are included in the spin Hamiltonian. Individual hydrogen peaks are not resolved and so can be accounted for in an approximate fashion with convolutional Gaussian line broadening, as evidenced by the good fit of the 2.35 MHz Gaussian linewidth convolutional broadening simulation. According to the simulations, the low-field feature also is not accounted for by hydrogen hyperfine splitting.

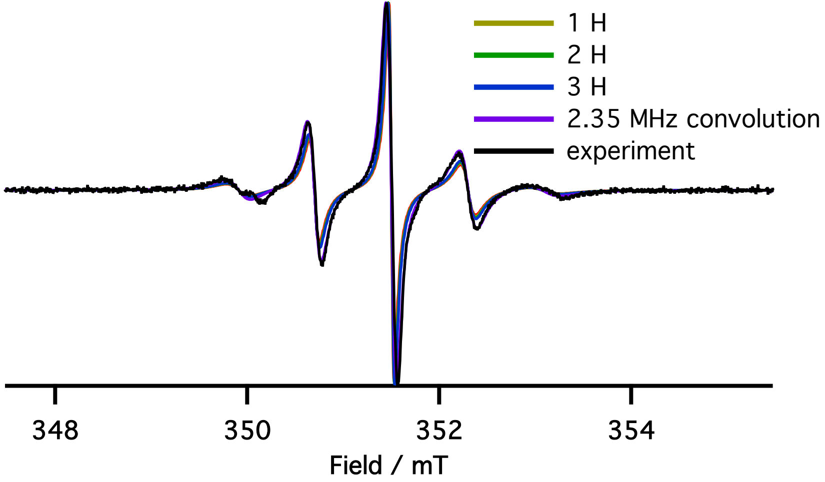

Figure 3.12: Slow-motion simulation fits to the nitronyl nitroxide X-band spectrum in 75% glycerol from data set 2. Simulations that included only the two nitrogen-14 nuclei were unable to reproduce the low-field feature. Explicit simulation of the proton hyperfine interactions suggests that the low-field feature is not due to proton hyperfine coupling. The 1-H simulation includes an *ortho*- hydrogen, the 2-H simulation additionally includes a *meta*- hydrogen, and the 3-H simulation also includes a methyl hydrogen. Hydrogen hyperfine couplings are not resolved in this slow-motion spectrum.

3.4.2 Two-component analysis

The unexpected low-field feature in the slow-motion spectra from data set 2 appears not to be due to hydrogen hyperfine interactions within the nitronyl nitroxide, based on the simulations in figure 3.12. In contrast to data set 2, the motional spectra from data set 1 do not exhibit this low-field feature. The spectra in data set 1 were measured with samples in 50% glycerol while the spectra in data set 2 were of much higher glycerol concentration, so perhaps the origin of the low-field feature is related to solvent conditions. If the different solvent environment of high glycerol concentration caused some population of the nitronyl nitroxide molecules to adopt a stable conformation that differed from that in lower glycerol solvent, then that new conformation could have different g- or A-values. Alternatively, perhaps the ensemble of nitronyl nitroxide molecules has multiple stable conformations in any solvent, but interconversion between conformations is too rapid to observe the distinct spectral fingerprint of each conformation in lower viscosity solvents.

A simple two-component model was used to fit slow-motion simulations to the 75% glycerol spectrum from data set 2 in order to determine if the presence of the low-field feature could be due to the presence of multiple nitronyl nitroxide conformers in the high-viscosity samples. The model assumes that there are two conformational populations and that the two conformations differ primarily in their hyperfine tensors. To determine reasonable hyperfine couplings for different conformations of the nitronyl nitroxide, ORCA was used to calculate EPR parameters for different geometries in the same manner as explained earlier in this chapter [62]. A comparison of two conformations, planar and twist, along with their calculated hyperfine couplings are shown in figure 3.13. In the planar conformation, both the phenyl and the imidazole rings are coplanar whereas in the twist conformation the rings are rotated 90° so that the plane of one ring is perpendicular to the plane of the other. The x- and y-components of the hyperfine tensors are weak and nearly the same in each conformation, but the z-components differ by about 10%, which would result in an observable difference in the splittings of peaks in the spectra of each conformer. In particular, because the low-field peaks narrow toward the isotropic limit at higher rotational correlation times than the high-field peaks, differences in peak splittings should be more apparent in the low-field region than the high-field region in the slow-motion regime.

A comparison of the one-component fit in figure 3.11 and the two-component fit are shown in figure 3.14. For the two-component fit, the general SLE solver was used simulate each component separately, with the overall fit in figure 3.14 being a weighted average of the two individual simulations. The weights correspond to the relative populations of each component in the sample ensemble. The simulation of the second component is identical to the first component except that the nitrogen A_z values are scaled relative to the first component by some factor. This scaling, along with the relative weights of each component, were varied until the two-component fit reproduced the low-field feature in the data while minimizing the misfit in the rest of the spectrum. The second component in the fit shown in figure 3.14 has an A_z that is 86% of that in the first component and the relative populations of the two components is 3:1, with the first component being the dominant population.

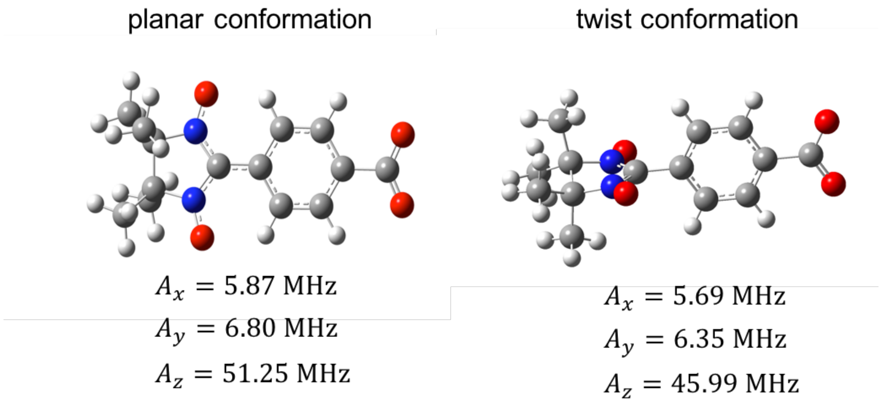

Figure 3.13: Nitrogen hyperfine splittings calculated for two potential conformations of the nitronyl nitroxide. The z-component of the hyperfine coupling of the twist conformation on the right is about 10% less than that of the lower energy planar conformation on the left.

With the two-component model used to fit the 75% glycerol spectrum in figure 3.14, the low-field feature can somewhat be accounted for. However, fitting this feature results in a poorer fit across the rest of the lineshape compared to the one-component model. In fact, for this two-component model, the minimal fit error occurs when the populational weight of the twist conformation is zero, which suggests that there is only one significant conformer that gives the lineshapes observed in data set 2. The origin of the additional low-field feature is therefore likely due to some other aspect of the sample, perhaps contamination by other paramagnetic species due to side products in the synthesis of the nitronyl nitroxide.

3.5 Conclusions

Nitronyl nitroxides are good spin systems for slow-motion CW EPR lineshape analysis using the general SLE solver because of the multiple hyperfine interactions in these compounds — at least two hyperfine interactions with the nitrogen nuclei and additional hyperfine interactions with other magnetic nuclei that may be important to model. The simulations in this chapter illustrate that the general SLE solver is suitable for slow-motion analysis of $S = 1/2$ systems with multiple magnetic nuclei. The fits are good and rotational correlation times can be extracted from them.

For nitronyl nitroxides in particular, good fits to experimental spectra require that the relative orientations of the g-tensors and A-tensors be taken into account. As with the tensor

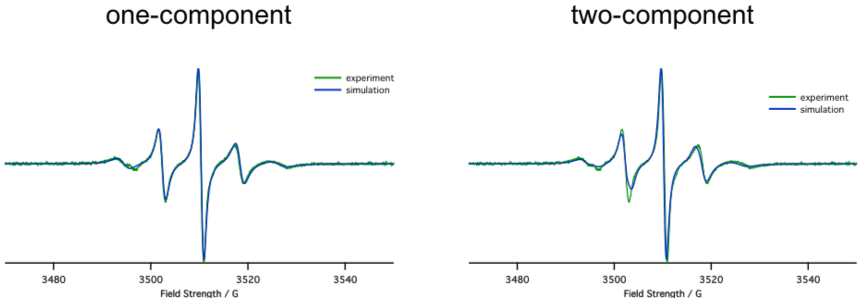

Figure 3.14: Nitrogen hyperfine splittings calculated for two potential conformations of the nitronyl nitroxide. The z-component of the hyperfine coupling of the twist conformation is 86% of that of the lower energy planar conformation. The relative populations of planar:twist conformers is 3:1.

principle values, good estimates of the tensor orientations can be obtained by fits to frozen spectra. Quantum chemistry calculations of EPR parameters are useful for obtaining initial guesses for tensor orientations.

The slow-motion spectra of data set 2 in figure 3.7 were simulated using best-fit parameters from simulations of the frozen spectrum **b** of data set 1 in figure 3.4. The additional low-field feature in the slow-motion spectra of data set 2 could not be fit well either by including explicit hydrogen hyperfine couplings in the spin Hamiltonian or by using a two-component model for the simulations.

Although the general SLE solver can, in principle, be used to simulate slow-motion CW EPR spectra for compounds with any number of hyperfine interactions, there is still the practical limitation of computational cost that prevents simulations of very large spin systems. Further developments for algorithmic optimization are likely possible. For example, calculation of the matrix elements of the Hamiltonian and rotational diffusion superoperator should be parallelizable because all of the matrix element evaluations are independent of each other.

Chapter 4

LARGE G-ANISOTROPY: COPPER-EGTA

4.1 Copper(II) spin system

Copper(II) is a $S = 1/2$ EPR-active d^9 transition metal ion with a single unpaired electron. Natural copper consists entirely of copper-63 (69.15% abundance) and copper-65 (30.85% abundance), with both isotopes having a nuclear spin $I = 3/2$. Therefore, each electronic manifold ($m_S = +1/2$ and $m_S = -1/2$) is split into four additional states due to the hyperfine interaction with the copper nucleus, as shown in figure 4.1. Copper(II) compounds usually have highly anisotropic and nearly axial g-tensors and A-tensors due to the d^9 electron configuration resulting in uneven sharing of electrons between axial versus equatorial ligands [64, 65].

A typical spin Hamiltonian for a copper(II) compound is

$$\hat{H} = \mu_{\mathrm{B}} \boldsymbol{B} \cdot g \cdot \hat{\boldsymbol{S}} + \hat{\boldsymbol{S}} \cdot A \cdot \hat{\boldsymbol{I}} \tag{4.1}$$

where the first term is the electron Zeeman interaction between the unpaired electron and the external magnetic field and the second term is the hyperfine interaction between the $I = 3/2$ copper nucleus and the unpaired electron. The nuclear Zeeman term has been omitted because it is typically negligible compared to the electron Zeeman and hyperfine interactions [64, 66, 67]. In some copper(II) compounds, and under certain experimental conditions, additional spin Hamiltonian terms may be included if there are significant hyperfine or nuclear quadrupole interactions with ligand nuclei that affect the observed lineshape [68, 69].

I chose to measure CW lineshapes of copper(II) compounds in order to investigate the validity of the frequency-to-field conversion approximation, which allows the SLE lineshape to be rapidly calculated using numerical techniques such as the Lanczos method [21, 22, 49]. The high g-anisotropy of copper(II) compounds results in much broader spectral lineshapes than organic radicals like nitroxides, so copper is better suited to reveal experimental conditions

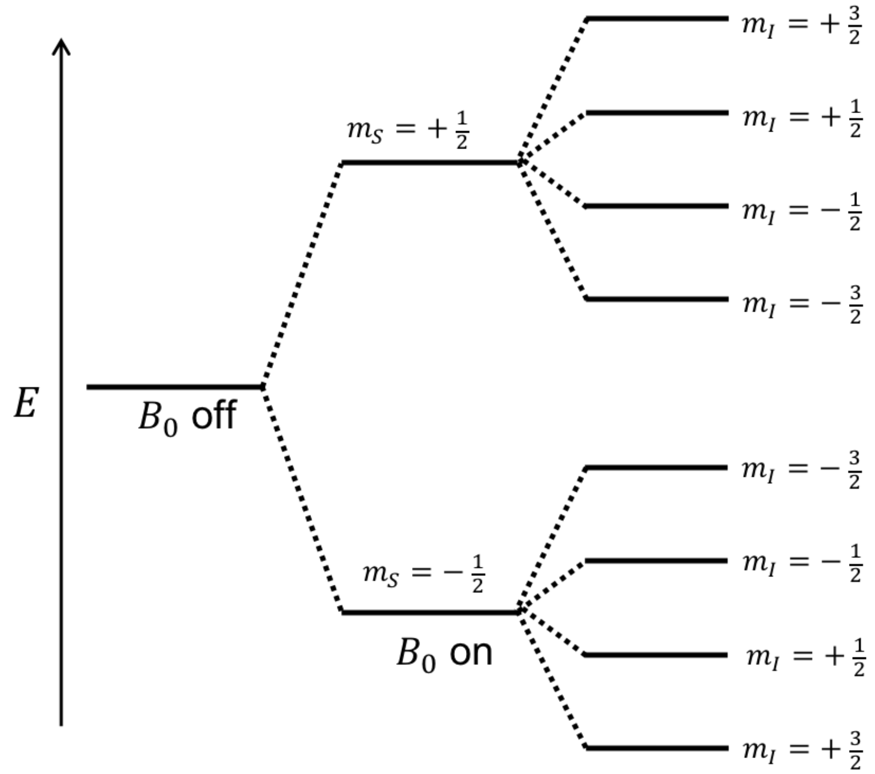

Figure 4.1: Energy level diagram for the spin states of a single orientation of an axial copper(II) compound without ligand spin Hamiltonian interactions. The nuclear Zeeman interaction is neglected, so the energy level splittings are due to the hyperfine interaction with the copper nucleus.

in which the frequency-to-field conversion approximation may become invalid. Furthermore, copper(II) compounds serve as good model systems for investigating the conversion error because these systems are $S = 1/2$, which means they do not have the additional simulation complexities that can arise due to electron-electron spin interactions.

4.2 Lineshapes of copper(II) compounds

4.2.1 Rigid-limit lineshape

The rigid-limit CW lineshape of most copper(II) compounds consists of two well-separated regions, a parallel region and a perpendicular region, as shown in the simulation of figure 4.2.

The parallel region is due to the z-components of the g- and A-tensors and the parallel region is due to the xy-components of these tensors. Due to the large g-anisotropy, the spectral width of this simulated rigid-limit spectrum is more than 60 mT, which is over an order of magnitude broader than a typical nitroxide spectrum.

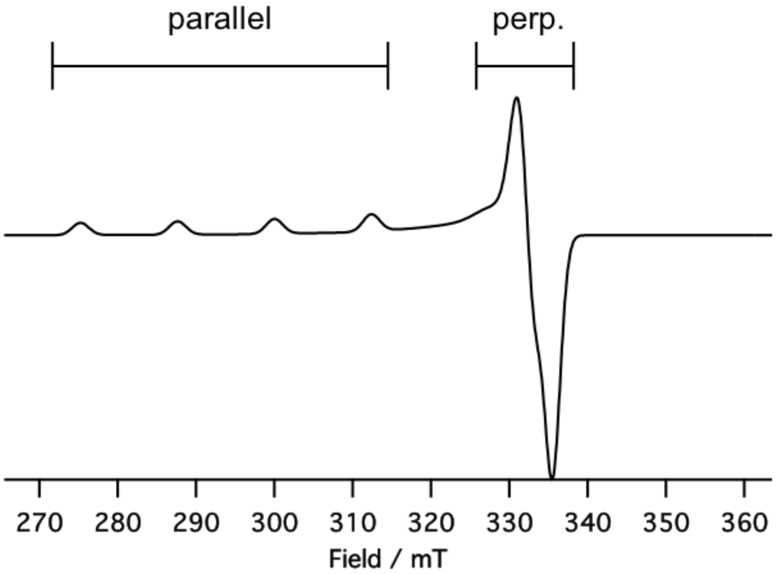

Figure 4.2: Simulated rigid limit CW lineshape of a typical axial copper(II) compound at a microwave frequency of 9.5 GHz. The tensor principle values are $g_{||} = 2.31$, $g_{\perp} = 2.04$, $A_{||} = 400$ MHz, and $A_{\perp} = 100$ MHz. The spectrum is convolved with a 2.5 mT FWHM Gaussian broadening.

4.2.2 Isotropic-limit lineshape

In the isotropic limit, the CW lineshape of copper(II) compounds consists of four lines centered about g_{iso} and separated by A_{iso}, where the isotropic values are the average of the three principle values of each tensor. The simulation in figure 4.3 shows a simulation of the same copper(II) system shown in figure 4.2, but in the near-isotropic limit with a rotational correlation time τ_{c} of 5 ps.

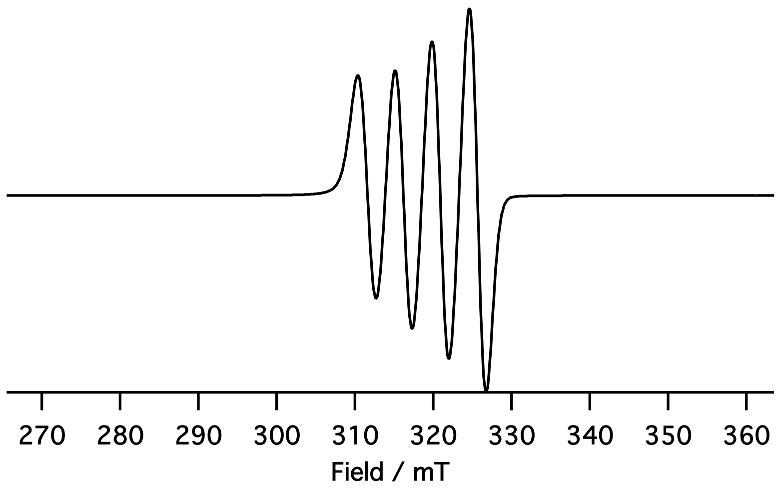

Figure 4.3: Simulated near-isotropic limit CW lineshape of a typical axial copper(II) compound at a microwave frequency of 9.5 GHz. The tensor principle values are $g_{\|} = 2.31$, $g_{\perp} = 2.04$, $A_{\|} = 400$ MHz, and $A_{\perp} = 100$ MHz. The spectrum is convolved with a 2.5 mT FWHM Gaussian broadening and $\tau_{\mathrm{c}} = 5$ ps.

4.3 Sweep method simulation error

The frequency-to-field conversion sweep approximation introduced in chapter 2, which calculates the lineshape using a spin Hamiltonian defined at a single B_0 field value, is not appropriate for spin systems with broad spectral lineshapes due to g-anisotropy.

This situation is shown in figure 4.4 by comparing exact lineshape powder simulations to rigid-limit SLE simulations using both the field-converted frequency sweep method and the explicit field sweep method. The simulated copper(II) system has axial g-tensor values $g_{\|} = 2.2$ and $g_{\perp} = 2.05$ and axial hyperfine splitting $A_{\|} = 100$ MHz and $A_{\perp} = 20$ MHz, with electronic spin $S = 1/2$ and a copper-63 nuclear spin $I = 3/2$. In figure 4.4**a**, it is clear that the explicit field sweep SLE simulation gives the same result as the exact lineshape powder simulation, but the approximate field sweep method gives incorrect line positions and incorrect overall spectral width. Although slow-motion SLE simulations of copper compounds have been performed, these simulations used the frequency-dependent lineshape function in equation 2.39 [66, 67, 70, 69]. To my knowledge, the validity of the frequency-to-field conversion approximation has not been previously explored for copper spectra.

Figure 4.4**b** shows the same type of simulations as in 4.4**a**, but for a narrow nitroxide spectrum with slightly rhombic g-tensor principle values $g_x = 2.009$, $g_y = 2.006$, and $g_z = 2.0025$ and axial hyperfine splitting $A_{\|} = 90$ MHz and $A_{\perp} = 15$ MHz, with electronic spin $S = 1/2$ and nitrogen-14 nuclear spin $I = 1$. For such a narrow spectral width, both the approximate field sweep method and the explicit field sweep method yield simulations that agree with the exact lineshape powder simulation. The copper simulations in figure 4.4**a** were convolved with 1 mT FWHM Gaussian inhomogeneous line broadening and the nitroxide simulations in figure 4.4**b** were convolved with 0.5 mT FWHM Gaussian broadening.

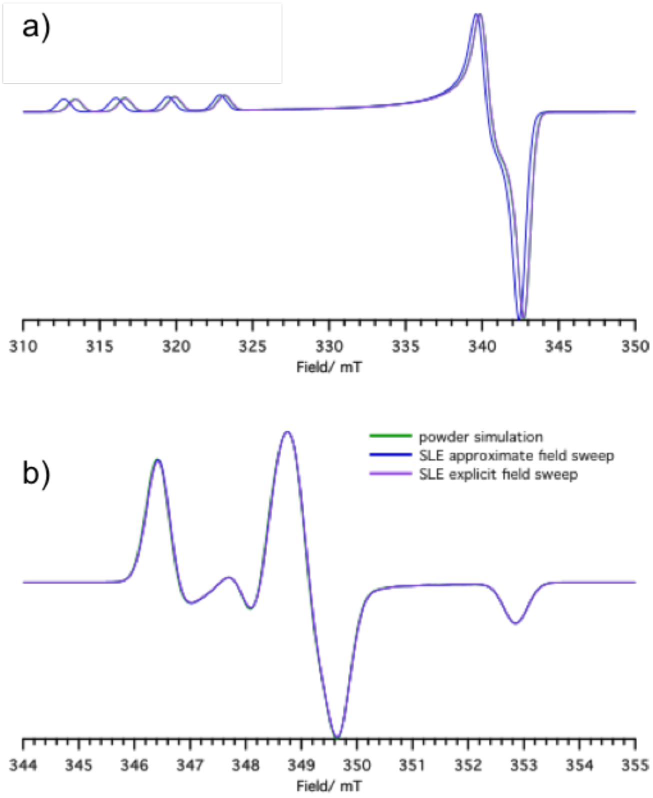

Figure 4.4: Copper (a) and nitroxide (b) simulations comparing SLE simulations in the rigid limit ($\tau_c = 1\,\mu$s) to full powder simulations. For a narrow spectrum such as the nitroxide, an approximate field sweep is sufficient to capture the correct line positions and spectral width in the rigid limit. For a copper system with highly anisotropic g-tensor, the approximate field sweep does not accurately simulate the spectral width and peak positions of the rigid limit spectrum.

Figure 4.5 shows a series of copper(II) simulations over a range of rotational correlation times using the same parameters as the system in figure 4.4**a**, except that no convolutional inhomogeneous broadening has been incorporated into the lineshape. Approximate and explicit field sweep simulations are compared for each rotational correlation time. For this simulated copper(II) system, even in the slow motion regime there are discrepancies between the approximate and explicit field sweep simulation methods. For faster rotational correlation times the spectrum becomes more isotropic and the g-anisotropy that contributes to the error in the approximate field sweep simulation is no longer relevant. However, as the rotational correlation time increases and approaches the rigid limit, the simulations suggest that approximate field sweeps are no longer appropriate for this system.

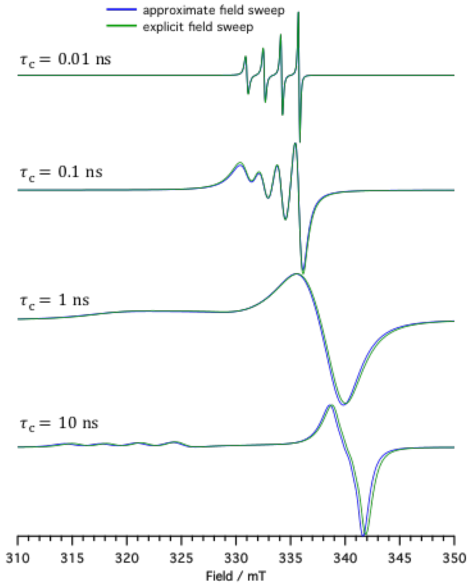

Figure 4.5: A series of motional copper spectra simulated using the general SLE solver. For each rotational correlation time, lineshapes obtained from both the approximate and explicit field sweep methods are compared. As the molecule tumbles more slowly, the discrepancy between the two simulation methods becomes more apparent.

4.4 Investigation of model copper(II) complexes

X-band CW EPR spectra were measured for four different copper(II) compounds in order to choose a promising model system for a temperature series measurement to investigate how the lineshape depends on rotational correlation time and to determine the motional regime in which the frequency-to-field approximation may be invalid for fitting slow-motion copper(II) simulations to experimental spectra. The four compounds that were synthesized and investigated were copper(II) histidine (Cu-His), copper(II) imidazole (Cu-Imid), copper(II) EDTA (Cu-EDTA), and copper(II) EGTA (Cu-EGTA). Frozen X-band spectra were measured at 200 K for each of these four copper(II) compounds, as shown in figure 4.6.

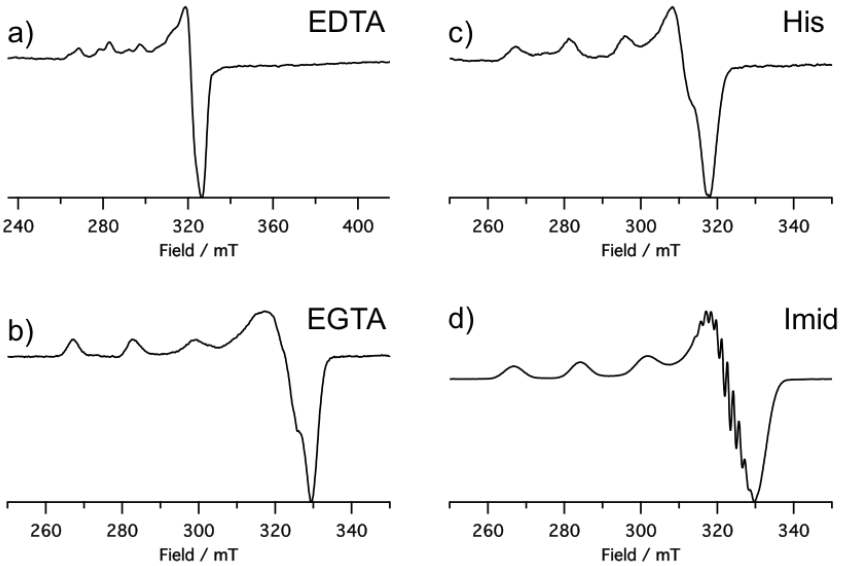

Figure 4.6: Frozen X-band CW spectra of four copper(II) compounds measured at 200 K with a microwave frequency of 9.32 GHz. The four ligands are EDTA (a), EGTA (b), histidine (c), and imidazole (d). The EDTA and histidine complexes were not background corrected.

Higher temperature measurements were taken for Cu-EDTA, Cu-His, and Cu-EGTA complexes. The Cu-Imid complex exhibits significant imidazole nitrogen ligand hyperfine coupling which is apparent in the perpendicular region of the spectrum in figure 4.6**d**. This so-called superhyperfine splitting is common in copper(II) complexes with nitrogenous ligands [68, 71]. To explicitly model the hyperfine splittings due to the ligand nitrogens, the spin Hamiltonian would include a nitrogen hyperfine term for each ligand and the size of the spin space would be too large to complete slow-motion simulations in a reasonable amount of time. It is possible that weak hyperfine splittings could be modeled using a postconvolution approach [67, 60], but that extra complexity in the model is not necessary for the investigation of the validity of the frequency-to-field approximation. Therefore, the Cu-Imid complex was not chosen as the model copper(II) system for further lineshape analysis.

X-band spectra of Cu-EDTA and Cu-His measured at various temperatures are shown in figure 4.7. The splitting of hyperfine peaks in the parallel regions of the frozen Cu-EDTA spectrum in figure 4.6**b** suggests that this compound exists as two distinct conformers in solution, each with a distinct A-tensor and possibly g-tensor as well. This splitting of hyperfine peaks is less apparent in the higher-temperature liquid solution Cu-EDTA spectra in figure 4.7**a**. However, simulation of the Cu-EDTA complex would require twice the number of parameters as a complex that only had one conformer, which would require twice the computational cost. Therefore, Cu-EDTA was not chosen for further analysis of the sweep method error.

The frozen Cu-His spectrum in figure 4.6**c** and the corresponding motional spectra in figure 4.7**b**, as well as the Cu-EGTA spectrum in figure 4.6**b**, all appear to consist of a single conformer and lack features that would suggest the need to simulate explicit interactions with ligand nuclei. Therefore, both the Cu-His complex and the Cu-EGTA complex were promising as model systems to investigate the motional regime in which there is significant frequency-to-field conversion error. However, the Cu-EGTA sample had better signal-to-noise ratio, so that complex was ultimately chosen for a complete temperature series measurement and lineshape analysis.

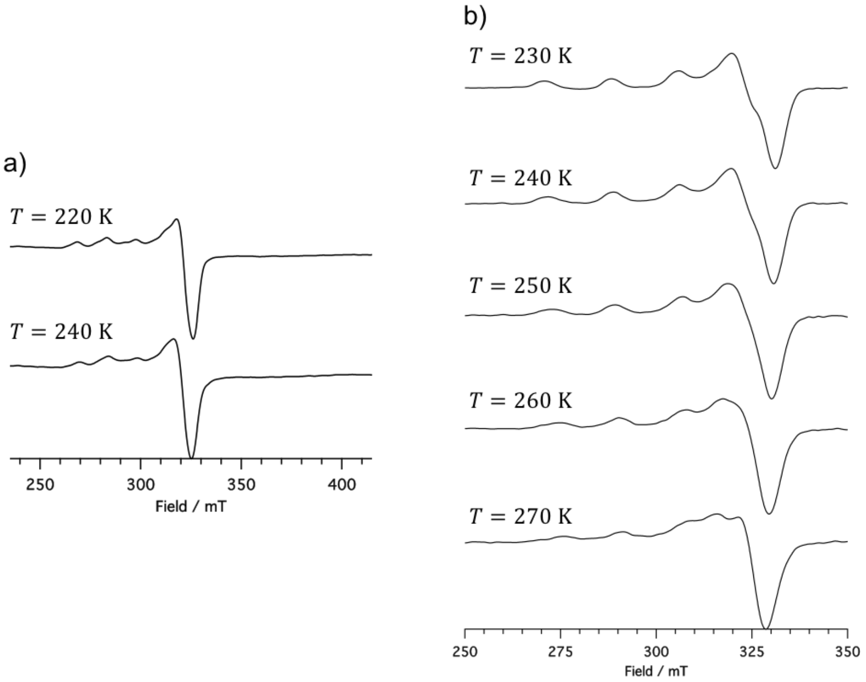

Figure 4.7: Motional spectra for the Cu-EDTA complex (a) and the Cu-His complex (b). Both compounds appear to consist of a single species without significant ligand hyperfine interactions.

4.4.1 Sample preparation

Cu-EDTA

The Cu-EDTA sample contained a 1 mM concentration of Cu-EDTA in 50:50 by volume glycerol:water solution. Copper(II) ions came from naturally abundant copper(II) sulfate pentahydrate salt and the EDTA ligand was purchased from a reputable supplier. The solvent was prepared by adding equal volumes of nanopure water and pure glycerol, then stirring at room temperature for 30 minutes. To the solvent, enough copper(II) sulfate pentahydrate and EDTA were added so that the concentration of copper(II) ions was 1 mM and EDTA was in excess of approximately 10:1 EDTA:copper(II) to ensure full complexation of copper(II) ions. The reaction mixture was brought to pH 12 by addition of sodium hydroxide, then stirred for 2.5 hours. Afterward, a small volume of the sample was transferred to a 1.5 mm inner diameter quartz EPR tube via capillary action. The remaining sample solution was stored in a dark -80° C freezer for future use. A second 1.5 mm inner diameter quartz EPR sample tube was filled with 50:50 glycerol:water solution without any copper(II) ions or EDTA to serve as a blank for background correction.

Cu-EGTA

The Cu-EGTA sample contained a 2 mM concentration of Cu-EGTA in 30:70 by volume glycerol:water solution. Copper(II) ions came from a 10 mM stock solution of aqueous naturally abundant copper(II) sulfate and the EGTA from a 100 mM stock solution of aqueous EGTA ligand, which was purchased from a reputable supplier. To ensure full complexation of the copper, a 20:1 EGTA:copper(II) solution was prepared by combining 0.2 mL of copper(II) sulfate stock, 0.4 mL of EGTA stock, 0.0667 mL of nanopure water, and 0.333 mL of MOPS buffer (pH 7.49) in 90% glycerol by volume. The solution was allowed to sit at room temperature for 3 hours before transferring a small volume into a 1.5 mm inner diameter quartz EPR tube for measurement. The remaining sample solution was stored in a dark -80° C freezer for future use. A blank was prepared by mixing 0.333 mL of MOPS buffer with 0.666 mL of nanopure water.

Cu-Histidine

The Cu-His sample contained a 1 mM concentration of Cu-His in 50:50 by volume glycerol:water solution. Copper(II) ions came from naturally abundant copper(II) sulfate pentahydrate salt and the histidine ligand was purchased from a reputable supplier. The solvent was prepared by adding equal volumes of nanopure water and pure glycerol, then stirring at room temperature for 30 minutes. To the solvent, enough copper(II) sulfate pentahydrate and histidine were added so that the concentration of copper(II) ions was 1 mM and histidine was in excess of approximately 60:1 histidine:copper(II) to ensure full complexation of the copper(II) ions. The reaction mixture was brought to pH 12 by addition of sodium hydroxide, then stirred at room temperature for 2.5 hours. Afterward, a small volume of the sample solution was transferred to a 1.5 mm inner diameter quartz EPR tube. The remaining solution was stored in a dark -80° C freezer. A blank sample was prepared as a 50:50 by volume glycerol:water solution.

Cu-Imidazole

The Cu-Imid sample contained a 1 mM concentration of Cu-Imid in 30:70 by volume glycerol:water solution. Copper(II) ions came from a 5 mM stock solution of naturally abundant copper(II) sulfate in deuterated water, and the imidazole from a 500 mM stock solution of aqueous imidazole ligand. To ensure full complexation of the copper(II) ions, a 100:1 imidazole:copper(II) solution was prepared by combining 0.8 mL of copper(II) sulfate stock, 0.8 mL of imidazole stock, 0.106 mL of nanopure water, and 0.133 mL of MOPS buffer (pH 7.49) in 90% glycerol by volume. The solution was allowed to sit for 3 hours at room temperature before transferring a small volume into a 1.5 mm inner diameter quartz EPR tube for measurement. The rest of the sample solution was stored in a dark -80° C freezer. A blank was prepared by mixing 0.133 mL of MOPS buffer with 0.366 mL of nanopure water.

4.5 Experimental parameters for X-band Cu-EGTA measurements

4.5.1 Determination of experimental microwave power

X-band CW spectra of Cu-EGTA were measured over a range of temperatures from 200 K (frozen) to room temperature at a microwave frequency of 9.32 GHz. To optimize signal-to-noise ratio and minimize experiment time, a series of power spectra and modulation amplitude spectra were measured. The power series spectra each consist of 10 scans recorded at 200 K with a modulation frequency of 100 kHz and modulation amplitude of 2 G. The microwave power ranges from 40 dB (0.0202 mW) to 5 dB (63.8 mW) in increments of 1 dB. The raw background-corrected spectra and the spectra scaled by the square root of the microwave power are shown in figure 4.8, whereas the corresponding power saturation curve constructed from this data is shown in figure 4.9. Some saturation appears to occur at microwave powers as low 0.25 mW, however the spectra recorded at very low microwave powers have poor signal-to-noise ratio, which causes the maximum intensities of those spectra to have a large variance. The inset of figure 4.9 is a zoomed-in plot of a segment of the power saturation curve that shows a fairly linear region between 1 to 4 mW of microwave power followed by a sharper decline in maximum intensity as the microwave power is increased.

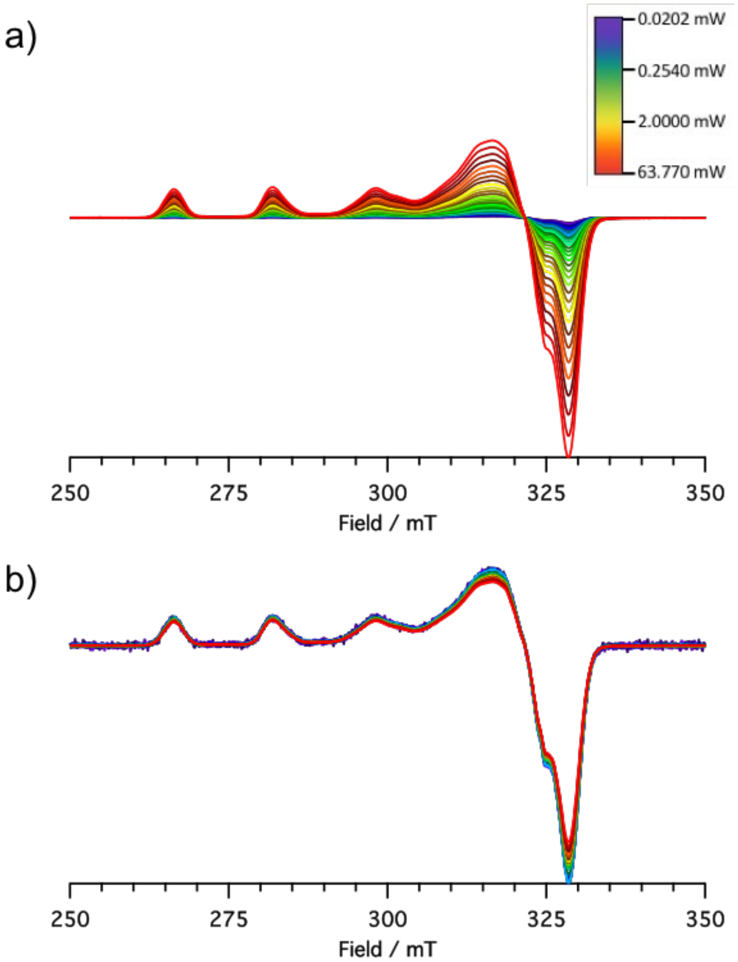

Figure 4.8: Power series of X-band Cu-EGTA spectra measured at 200 K with a microwave frequency of 9.32 GHz. The background-corrected unscaled data is shown in a) and the same spectra scaled by the square root of the microwave power under which they were measured are shown in b). The lineshape changes at higher power due to saturation.

Based on the power saturation results of figures 4.8 and 4.9, a microwave power of 2.02 mW (25 dB) was chosen for the temperature series lineshape measurements. At higher temperatures, saturation occurs at higher microwave powers because relaxation rates increase. The temperature series measurements were all at higher temperatures than the power saturation curve measurements. Therefore, even though the power saturation curve in figure 4.9 suggests there may be some minor saturation at 200 K with 2.02 mW of microwave power, the effects of saturation on the CW lineshape are likely insignificant at higher temperatures for this Cu-EGTA system.

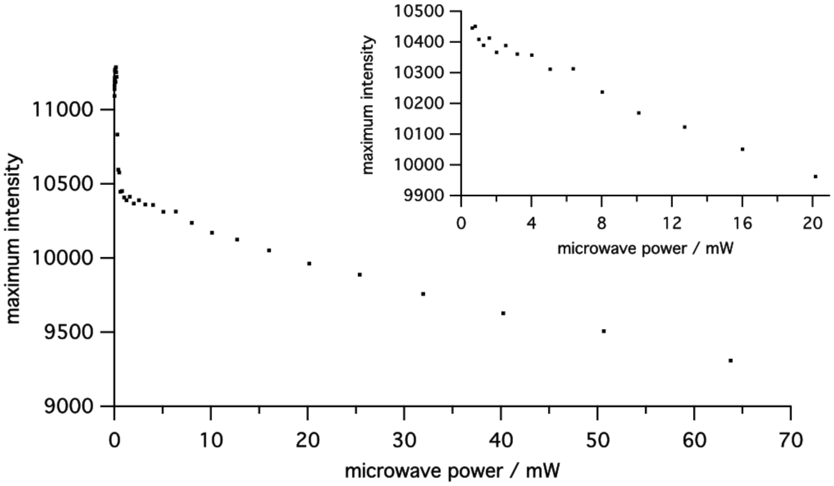

Figure 4.9: Power saturation curve constructed from the power series data in figure 4.8. Significant saturation occurs above 5 mW of microwave power. The inset is a zoomed-in view of the initial portion of the curve.

4.5.2 Determination of experimental modulation amplitude

A modulation amplitude series was also measured in order to choose a modulation amplitude that gave the greatest signal-to-noise ratio without distorting the Cu-EGTA CW lineshape. The modulation series spectra were measured over a range of modulation amplitudes from 2 G to 10 G in increments of 2 G, with all of them having a modulation frequency of 100 kHz. Each of the spectra were measured at 200 K with a microwave frequency of 9.32 GHz and a microwave power of 2.02 mW. The modulation amplitude series spectra are shown in figure 4.10.

The spectra in figure 4.10**a** are each an average of 10 scans and none of the spectra are scaled. The signal-to-noise ratio increases for larger modulation amplitudes. However, the segment of the perpendicular region of the spectra in figure 4.10**b** shows distortions in the lineshape at higher modulation amplitudes. The field of zero-crossing begins to shift to lower fields as the modulation amplitude increases. The zero-crossing fields of the 2 G, 4 G, and 6 G modulation amplitude spectra are nearly identical. Therefore a slightly conservative modulation amplitude of 5 G was chosen for the Cu-EGTA temperature series spectra.

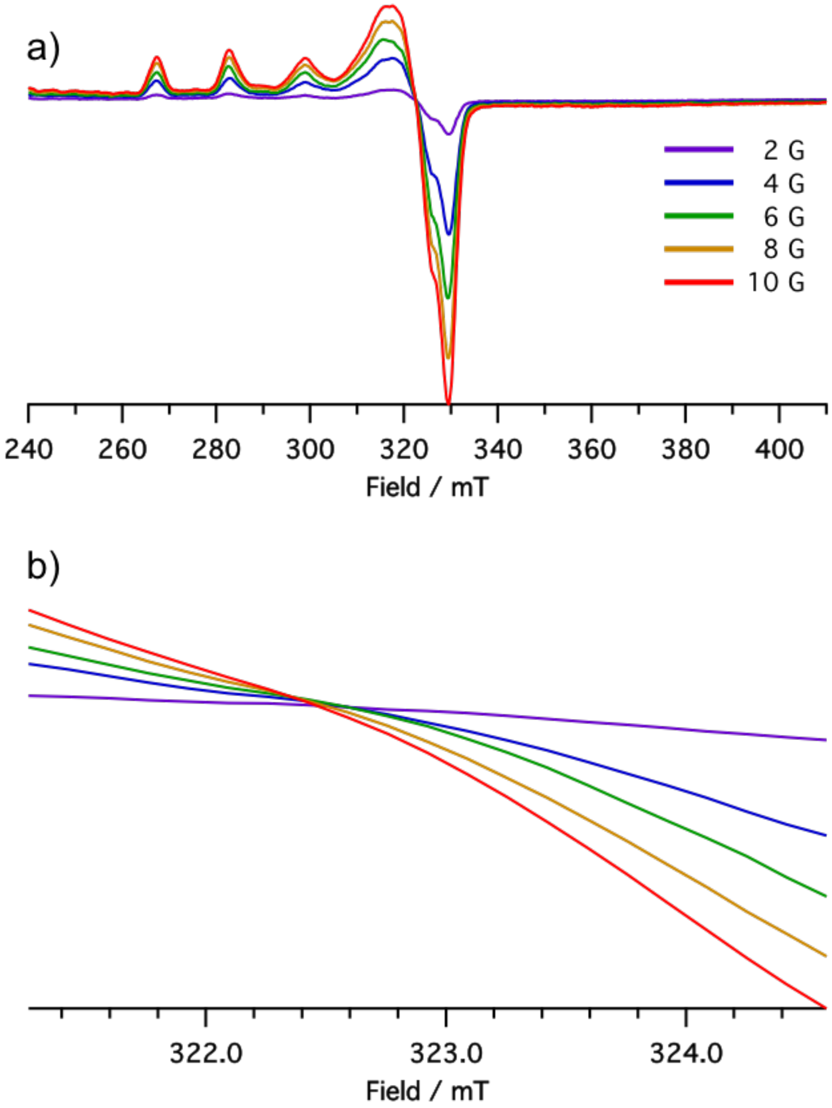

Figure 4.10: X-band Cu-EGTA spectra measured at 200 K over a range of modulation amplitudes are shown in panel a). A zoomed-in view of the zero-crossings of the perpendicular peak is shown in panel b).

4.6 Determination of Cu-EGTA simulation parameters

The spin Hamiltonian for Cu-EGTA is well-described by equation 4.1 because there are no discernible ligand interactions with the unpaired electron in the X-band lineshape. However, the Cu-EGTA sample was made with natural-abundance copper(II) sulfate, which consists of approximately 69.15% copper-63 and 30.85% copper-65. As mentioned in the introduction to this chapter, both copper-63 and copper-65 have a nuclear spin $I = 3/2$, but the nuclear magnetic moments of the isotopes differ because each isotope has a unique nuclear g-factor. Therefore, the natural-abundance Cu-EGTA sample contains two distinct systems each with its own spin Hamiltonian. The spin Hamiltonians for each isotope are

$$\begin{aligned} \hat{H}_{63} &= \mu_{\mathrm{B}} \boldsymbol{B} \cdot g \cdot \hat{\boldsymbol{S}} + \hat{\boldsymbol{S}} \cdot A_{63} \cdot \hat{\boldsymbol{I}} \\ \hat{H}_{65} &= \mu_{\mathrm{B}} \boldsymbol{B} \cdot g \cdot \hat{\boldsymbol{S}} + \hat{\boldsymbol{S}} \cdot A_{65} \cdot \hat{\boldsymbol{I}} \end{aligned} \tag{4.2}$$

where A_{63} and A_{65} are the hyperfine tensors corresponding to the copper-63 and copper-65 isotopes, respectively. These tensors are not the same because the different isotopic magnetic moments result in different strengths of the hyperfine interaction with the unpaired electron. The ratio of the nuclear g-factors for the two isotopes of copper is $g_{63}/g_{65} = 0.934$. The electron Zeeman term is the same in both Hamiltonians because that interaction is unaffected by the nuclear magnetic moments.

All subsequent simulations in this chapter use both of the spin Hamiltonians in equation 4.2 to fit the experimental Cu-EGTA data. Using both Hamiltonians, the overall simulated spectrum is

$$I_{\textit{Cu-EGTA}} = w_{63} I_{63} + w_{65} I_{65} \tag{4.3}$$

where $w_{63} = 0.6915$ and $w_{65} = 0.3085$ are the percent-natural-abundance weights of the two isotopes and I is the lineshape function, which may be either frequency-dependent or field-dependent. In practice, each fit amounts to a weighted sum of two simulations – one copper-63 simulation using hyperfine tensor A_{63} with weight w_{63} and one copper-65 simulation using hyperfine tensor A_{65} with weight w_{65}. The computational cost of the Cu-EGTA simulations would be cut in half if the sample were made from isotopically pure copper-63 or copper-65. However, isotopically pure copper is more expensive, of course.

4.6.1 Rigid-limit spectrum simulation

Using a microwave power of 2.02 mW with a modulation amplitude of 5 G and modulation frequency of 100 kHz, chosen as described in the previous section, a frozen X-band spectrum of Cu-EGTA was measured at 200 K and 9.32 GHz to fit the g-tensor and A-tensor values for subsequent use in fitting higher temperature motional spectra. The measured experimental spectrum and the best-fit simulation are shown in figure 4.11. The best-fit parameters that give the simulation in figure 4.11 are listed in table 4.1.

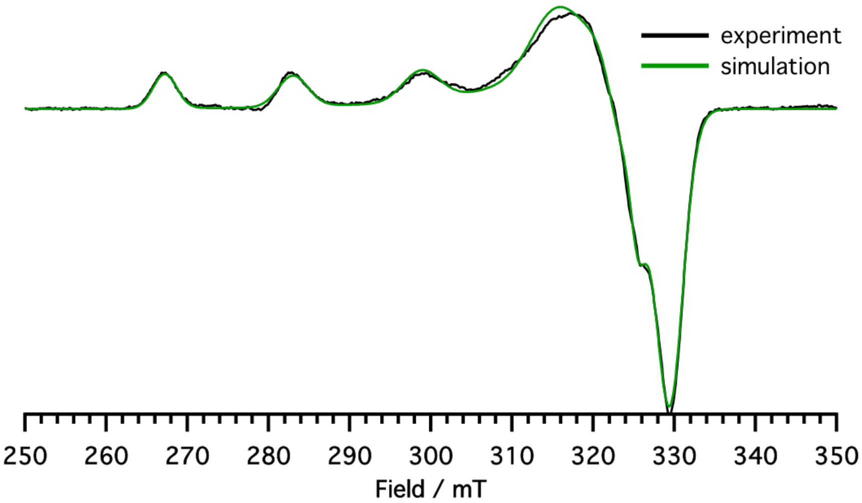

Figure 4.11: X-band frozen CW spectrum of Cu-EGTA in 30% glycerol solution measured at 200 K with a microwave frequency of 9.32 GHz. The g- and A-tensors are collinear and have the principle values given in table 4.1. Line broadening due to a distribution in Cu-EGTA geometries is simulated using g-strain and A-strain. Broadening due to unresolved hyperfine couplings is simulated as a 2.41 mT Gaussian convolution.

Table 4.1: Best-fit parameters for the frozen X-band Cu-EGTA spectrum shown in figure 4.11. The strains are Gaussian FWHM values that confer differential broadening due to a Gaussian distribution in the corresponding parameters within the sample. An additional 2.41 mT FWHM Gaussian inhomogeneous broadening was convolved over the entire simulated lineshape.

	g_x	g_y	g_z	A_x / MHz	A_y / MHz	A_z / MHz
principal value	2.0498	2.0781	2.2888	-40.4	-62.2	-496.0
strain	0	0.042	0.033	0	0	38.0

Cu-EGTA is nearly axial, with $g_x \approx g_y$ and $A_x \approx A_y$ in the perpendicular region of the spectrum, as is typical for copper(II) complexes. The compound is also highly anisotropic compared to organic radicals such as nitroxides, with g_z (or $g_{\|}$) much greater than g_x and g_y (or $g_{\perp}$). The same is true for the A-tensor. Given the strain of 0.042 in the y-component of the spectrum, there is likely a population of Cu-EGTA geometries that is truly axial in the g-tensor, although the best-fit parameters for frozen Cu-EGTA do not include any strain in the axial components of the A-tensor. Note that, at X-band, the axial region of the spectrum is not well resolved, so it is possible that other combinations of best-fit parameters in the axial components of the g- and A-tensors could also give good fits. However, the parameters in table 4.1 were obtained after trying many starting points for the best-fit optimization.

4.7 Fits to motional temperature series spectra

The rotational correlation time of an EPR sample is related to the viscosity of the sample. As viscosity increases, rotational correlation times become longer due to the hindered rotational ability of the paramagnetic molecules. Viscosity of the Cu-EGTA sample was varied between measurements by changing the temperature of the sample. The EPR sample tube was place in a SHQ cylindrical resonator, which was attached to a liquid-nitrogen flow line in order control the sample temperature. The temperature series spectra were measured from lowest to highest temperature, with temperature points at 250 K, 255 K, 260 K, 270 K, 280 K, 290 K, and 300 K. Between each measurement, the temperature was increased to the next temperature point and the sample was allowed to equilibrate to the new temperature for at least 10 minutes before taking the next measurement. An additional temperature point between 250 K and 260 K was chosen because changes in the lineshape of the spectrum were most sensitive to changes in temperature in the lower-temperature region of measurements. After measuring the Cu-EGTA spectra for all points in the temperature series, the same measurement procedure was repeated with a blank sample to be used for background subtraction of the data. The background-corrected temperature series data is shown in figure 4.12.

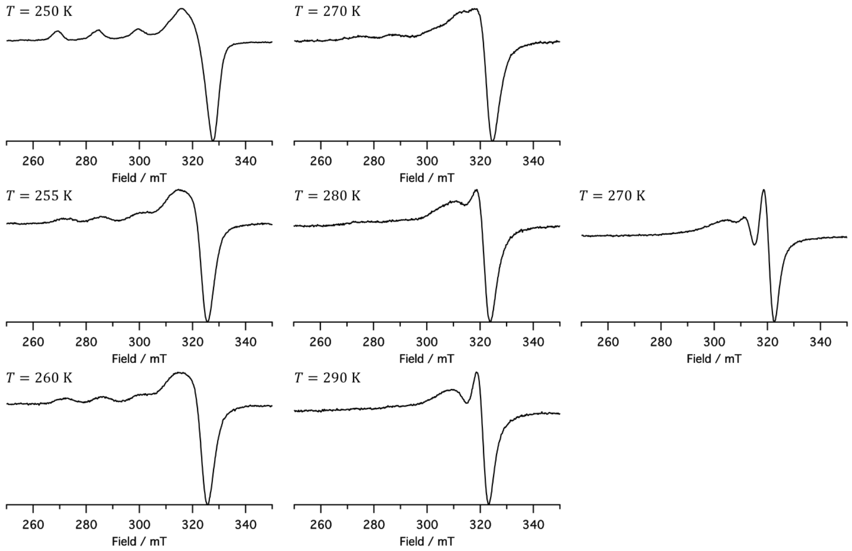

Figure 4.12: Temperature series CW X-band data for 1.0 mM CU-EGTA in 30% glycerol solution measured with a microwave frequency of 9.32 GHz.

The Cu-EGTA lineshape changes significantly with increasing temperature (i.e. decreasing viscosity). The lineshape of the 250 K spectrum in figure 4.12 is very similar to the frozen spectrum in figure 4.11. Up to 260 K, the copper hyperfine peaks in the parallel region of the spectrum are still apparent. Remnants of these peaks are still visible up to 280 K, but broaden out and begin to coalesce into a single peak near the perpendicular region of the 290 K and 300 K spectra. Even up to 300 K (approximately room temperature), rotational motion of the Cu-EGTA complex is not rapid enough for the sample to be in the isotropic motional limit where the g- and A-tensor anisotropy completely averages out. Measurements were not taken at temperatures higher than 300 K, so it is unknown at which temperature the Cu-EGTA lineshape for this aqueous glycerol sample would approach the isotropic limit, consisting of four evenly separated peaks similar to the simulation in figure 4.3.

Copper spin systems are similar to nitroxides and nitronyl nitroxides in that these systems all consist of a single unpaired electron ($S = 1/2$) interacting only with an external magnetic field (Zeeman interaction) and with magnetic nuclei within the molecule (hyperfine interaction). However, fitting spectra for copper systems presents some unique challenges that are absent in $S = 1/2$ organic radicals. In particular, simulations of copper systems are complicated by large g-anisotropy, g- and A-strain, and possible changes in g- and A-tensor principle values upon transition from a frozen to a liquid sample.

4.7.1 Modeling strain in the motional regime

Most EPR spectroscopy is performed on a sample that contains an ensemble of the molecule of interest (although single-molecule EPR has been performed and is still an active area of research [72, 73]). In a solution sample, such as the Cu-EGTA in glycerol:water solvent, the ensemble may consist of several molecular geometries due to processes such as interconversion between different stable conformations or slight conformational differences due to dissimilar solvent environments. Upon freezing, the sample then consists of a static distribution of conformational populations of paramagnetic molecules. Because g-tensor and A-tensor values depend on molecular structure, a frozen conformational ensemble has an ensemble of g- and A-values as well, even for molecules that have the same orientation within the external magnetic field. This distribution in tensor values is referred to as strain.

The effect of strain on EPR spectra is to broaden the linewidths, therefore strain is commonly a component of models used to fit transition metal EPR spectra [74, 68, 75]. Different components of the g- and A-tensors may have different amounts of strain, which causes the peaks associated with each component to broaden differently due to strain. For example, the A-strain values in table 4.1 from the fit of frozen Cu-EGTA suggest that a distribution in hyperfine tensor values contributes to the linewidths of the peaks in the parallel region of the spectrum in figure 4.11, but not to the linewidth of the large peak in the perpendicular region.

Distributions in g- and A-tensors vary depending on the type of compound. For example, any line broadening due to g- and A-strain in the relatively narrow spectra of organic radicals is negligible whereas broad copper spectra usually require some kind of strain model to obtain accurate fits. The strain model used to fit the frozen Cu-EGTA spectrum assumes a Gaussian distribution of g- and A-values with the principle values listed in table 4.1 being the maxima of the distributions and the strain values being the FWHM widths of the distributions. The true distributions are unknown, but the assumption of a normal distribution gives good fits to the data.

The general SLE solver described in chapter 2 does not include an implementation of any kind of strain model, so the linewidth parameters from the fit in figure 4.11 could not be directly used to fit to the motional data shown in figure 4.12. Even if the strain model used to fit the frozen spectrum could be used to fit the motional spectra, it is unknown whether the conformational distribution of the frozen sample is the same as that of the liquid sample.

It is also possible that the conformational distribution of the liquid sample changes with temperature. The simplest approach to model line broadening that is not due to rotational motion is to convolve the entire simulated lineshape with a Gaussian, as has been done in all of the simulations presented in this work. However, in addition to weak unresolved hyperfine splittings, the Gaussian convolutional broadening in Cu-EGTA has a component that is due to strain as well.

Figure 4.13 again shows the measured frozen Cu-EGTA spectrum, but with fits from two different broadening models: the strain model of the fit in figure 4.11 and a Gaussian convolution model. The Gaussian model fit convolutes the entire lineshape with a 5.1 mT FWHM Gaussian whereas the strain model is the same as that in the fit of figure 4.11. The strain model fits the data better than the Gaussian model because the Gaussian model broadens all of the peaks equally. However, the general shapes and positions of the peaks are accounted for in the Gaussian model and the broadening is fairly accurate for the high-field peaks. Therefore, the best-fit Gaussian convolutional broadening of 5.1 mT was used to to fit the motional spectra in figure 4.12 as a substitute for the strain model.

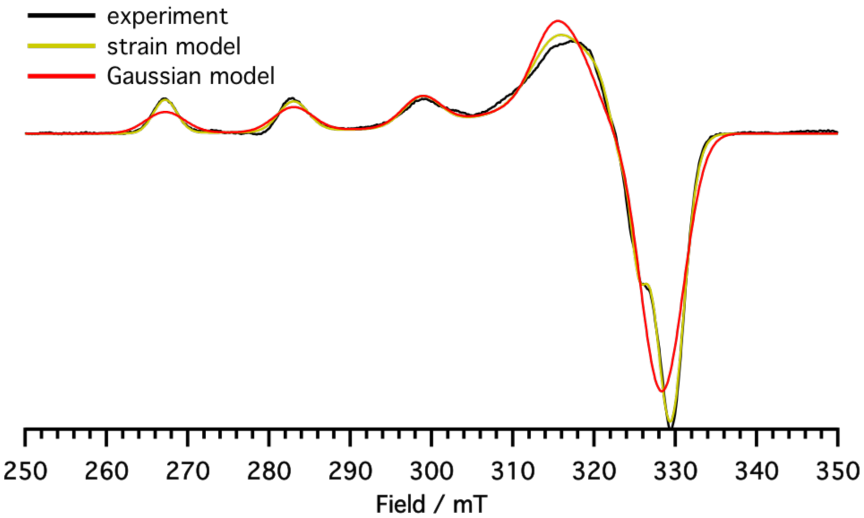

Figure 4.13: Two fits to the frozen X-band Cu-EGTA spectrum. The strain model fit is that same as that shown in figure 4.11. The Gaussian model fit convolutes the entire lineshape with a 5.1 mT FWHM Gaussian lineshape to capture broadening from various mechanisms that are not explicitly modeled.

4.7.2 Validity of rigid-limit parameters in the motional regime

Another complication in fitting slow-motion copper(II) spectra is that the principal values of the g- and A-tensors in a frozen sample may not be the same as in a liquid sample. Given that there is a distribution of tensor values, it is possible that the means of those distributions are environment-specific and therefore change in going from solid to liquid. Copper compounds have also been observed to exhibit freezing artifacts that may appear to distort g- and A-values upon freezing [76]. Freezing artifacts may be caused by aggregation of copper(II) complexes, which would cause dipolar interactions between Cu-EGTA molecules to affect the lineshape. The simulation models in this chapter all assume that none of the Cu-EGTA molecules are interacting with each other, so freezing artifacts could yield inaccurate fit parameters. However, at the sample concentration of 2 mM, it is unlikely that freezing artifacts have a significant affect on the observed Cu-EGTA frozen lineshape.

For the Cu-EGTA data in figure 4.12, deviations from the frozen g- and A-values were required to simulate good fits to the data. To illustrate this, figure 4.14 shows two simulations to fit the Cu-EGTA spectrum that was measured at 300 K: one using the frozen best-fit parameters and another that refits the g- and A-values. Both spectra have the same rotational correlation time $\tau_c = 0.138$ ns.

The large peak in the perpendicular region of the spectrum is shifted to a higher field in the frozen parameter fit. Adjusting the g- and A-values allows the SLE simulation to yield peaks at fields that correspond with the data. Forcing these values to be the same as the frozen simulation makes it impossible to obtain the correct peak position regardless of choice of τ_c, therefore the fits to the motional data were allowed to explore new spin Hamiltonian tensor values.

4.7.3 Comparison of sweep methods

The g- and A-tensors of copper systems are highly anisotropic compared to organic $S = 1/2$ systems such as nitroxides. For example, the spread in g-values ($\Delta g = |g_x - g_z|$) for the Cu-EGTA sample in figure 4.11 is $\Delta g = 0.2390$, while the spread for the nitronyl nitroxide in chapter 3 is $\Delta g = 0.0088$. The nitronyl nitroxide g-tensor is nearly isotropic compared to that of Cu-EGTA. The large g-anisotropy in copper systems can cause the frequency-dependent lineshape function of equation 2.39 to poorly approximate experimental lineshapes in the slow-motion regime.

To determine the motional regime in which the frequency-sweep approximation is invalid, the motional Cu-EGTA spectra in figure 4.12 were first fit with an explicit field-sweep model

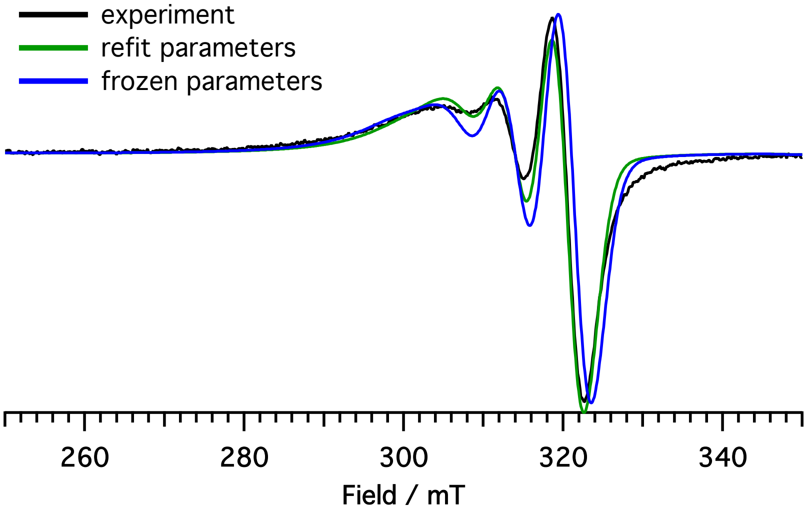

Figure 4.14: Comparison of best-fit simulations for the 300 K Cu-EGTA X-band spectrum measured at 9.32 GHz. Both simulations have a rotational correlation time $\tau_\mathrm{c} = 0.138$ ns and a residual Gaussian linewidth of 5.1 mT. The simulation in blue uses the g- and A-values from the 200 K frozen fit in figure 4.11. The simulation in green has the g- and A-values listed in table 4.2 that were refit for the liquid sample.

using the field-dependent lineshape function in equation 2.80. Then, using the best-fit parameters from the explicit field-sweep simulation, a frequency-to-field converted simulation that uses the frequency-dependent lineshape function of equation 2.39 was performed for each spectrum. The explicit field sweep simulations and the corresponding frequency-to-field converted simulations are shown in figure 4.15. The best-fit simulation parameters for each temperature are listed in table 4.2.

As expected, the rotational correlation times follow a trend of decreasing τ_c as temperature increases (i.e. viscosity decreases). Obtaining rotational correlation times using the general SLE solver is useful for a comparative study of Cu-EGTA viscosities, but the accuracies of the individual rotational correlation times in this study are uncertain because τ_c was varied along with the spin Hamiltonian tensor values. However, deviations from the frozen g- and A-values mostly affect the positions of peaks rather than the overall linewidths and lineshape. The deviations in g- and A-values from the frozen best-fit parameters do not follow any noticeably consistent pattern that correlates with sample temperature. The rotational correlation time is the only varied parameter that significantly affects the linewidths because the other linewidth parameter, the additional Gaussian convolutional broadening, was fixed

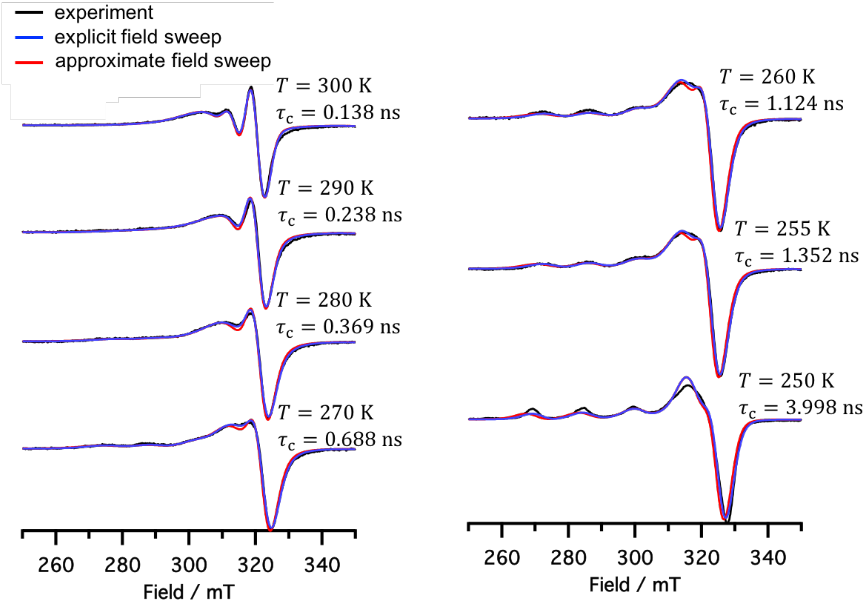

Figure 4.15: Cu-EGTA X-band temperature series SLE fits. The blue fits are from explicit field sweep simulations. The red fits use the frequency-to-field conversion approximation. The measurement temperatures and the best-fit rotational correlation times are given for each spectrum.

at 5.1 mT FWHM for each simulation.

Table 4.2: Best-fit parameters for the Cu-EGTA temperature series spectra using an explicit field sweep simulation model.

T / K	g_x	g_y	g_z	A_x / MHz	A_y / MHz	A_z / MHz	τ_c / ns
250	2.0750	2.0507	2.2920	-55.0	-35.0	-494.3	3.998
255	2.0580	2.0744	2.2884	-24.6	-51.0	-494.1	1.352
260	2.0636	2.0642	2.2900	-39.0	-39.7	-496.1	1.124
270	2.0680	2.0669	2.2912	-37.9	-34.7	-493.6	0.688
280	2.0500	2.0679	2.2963	-25.7	-41.4	-486.1	0.369
290	2.0500	2.0677	2.2941	-22.6	-26.4	-486.1	0.238
300	2.0662	2.0607	2.2838	-20.0	-20.0	-490.0	0.138

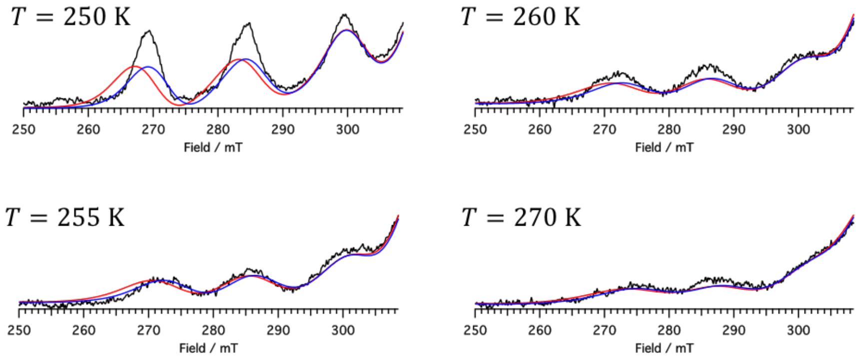

Figure 4.16: Zoomed-in view of the parallel region of the Cu-EGTA fits in figure 4.15 for the spectra measured between 250 K and 270 K. The error introduced by the approximate sweep method is significant at 250 K, but decreases up to 270 K where both simulation methods produce nearly identical lineshapes. The blue curves are the explicit field sweep fits and the red curves are the approximate field sweep fits.

The peak positions in the explicit field sweep simulations align well with the experimental data for spectra at every temperature, but the approximate frequency-to-field conversion sweep simulations have significant error in their peak positions up to 260 K. At 270 K and above (or $\tau_\mathrm{c} < 0.7$ ns), both methods yield nearly identical lineshapes. Figure 4.16 is a zoomed-in view of the parallel (or z) region of the spectra from 250 K to 270 K that shows the coalescence of sweep methods as the rotational correlation time decreases and the anisotropy of the frozen sample begins to average out. It appears that in the slow-motion regime, it is important to perform an explicit field sweep simulation for Cu-EGTA in order obtain valid spin Hamiltonian parameters.

4.8 Conclusions

Cu-EGTA is a good model spin system to study the validity of the frequency-to-field converted sweep approximation in the general SLE solver because this system has large g-anisotropy and is free of electron-electron interactions that could complicate the lineshape. The approximate sweep method was found to introduce significant error in the simulations of motional spectra in the slow-motion regime where $\tau_\mathrm{c} > 0.7$ ns for Cu-EGTA at X-band. Fits to the spectra in figure 4.15 using the approximate field sweep method would yield different g- and A-values than the explicit sweep method fits. However, there would be no way to know this from the simulation results if the user of the general SLE solver was not aware of the approximation.

At X-band, the perpendicular region of Cu-EGTA is not well resolved. The large high-field peak in all of the data presented in this chapter actually consists of all of the hyperfine peaks in the x- and y-regions as well as the highest-field parallel region hyperfine peak. This coalescence of many resonances into a single peak introduces some uncertainty in the best-fit parameters in the perpendicular region, which could be a reason why the spin Hamiltonian tensor values had to be refit at each temperature for the motional spectra. Additional studies of Cu-EGTA at higher fields and microwave frequencies could resolve some of the overlapping resonances and probably yield more accurate and consistent best-fit parameters.

Finally, the modeling of line broadening that is not due to rotational motion likely introduced additional uncertainty in the fit parameter sets. It could be beneficial to include a strain model in the general SLE or some other implementation that would allow for differential non-specific broadening across the whole spectrum.

Chapter 5

HIGH-SPIN SYSTEM: GADOLINIUM-DOTA

5.1 Introduction

Gadolinium(III) is a high-spin $S = 7/2$ EPR-active f^7 lanthanide metal ion with seven unpaired electrons. The $4f$ shell of gadolinium consists of seven f-orbitals. In the gadolinium(III) ion, each of the seven $4f$-orbitals holds one of the unpaired electrons such that all of the $4f$-orbitals are half-filled. This f^7 electronic structure of gadolinium(III) results in a spherically symmetric spatial distribution of the unpaired electrons even though the individual f-orbitals do not have spherical symmetry.

Gadolinium(III) has seen widespread commercial use in the medical industry for magnetic resonance imaging (MRI) as a contrast agent because it causes rapid relaxation of surrounding water molecules. Many different gadolinium(III) chelates have been synthesized and approved for medical usage because they have mostly been found to have low toxicity in doses commonly used for medical procedures [77, 78, 79, 80]. There is also growing interest in using gadolinium(III) compounds as spin labels in pulsed EPR experiments [81, 82, 83].

Because gadolinium(III) is used in medical procedures and scientific research, many studies have been done on the relaxation properties and EPR lineshapes of gadolinium(III) compounds in both solid and solution states [84, 85, 86, 87, 88]. Good models exist for simulating full gadolinium(III) solution spectra in the fast-motion regime [86, 89], but simulating slow-motion gadolinium(III) CW EPR lineshapes remains a challenge. Stochastic and molecular dynamics models have been used to simulate linewidths of the central transition in slow-motion gadolinium(III) spectra [33], but a general model to accurately simulate entire experimental lineshapes is still unavailable to the best of my knowledge at the time of this writing.

The validity of the general SLE solver, which was presented in chapter 2, for modeling slow-motion lineshapes of high-spin systems was studied by measuring a temperature series of spectra for a gadolinium(III) compound from frozen to room temperature. Changes in sample temperature change the sample viscosity, which changes the rate of rotational dynamics. The rotational correlation times can be used to fit the spectra at each temperature and evaluate the validity of the general SLE solver for studying slow-motion gadolinium(III) systems.

5.2 Gadolinium(III) spin system

Most gadolinium(III) compounds are well-described by the following spin Hamiltonian:

$$\hbar \hat{H} = \mu_{\mathrm{B}} \boldsymbol{B} \cdot g \cdot \hat{\boldsymbol{S}} + \hat{\boldsymbol{S}} \cdot D \cdot \hat{\boldsymbol{S}}. \tag{5.1}$$

The first term describes the usual electron Zeeman interaction and the second term describes the zero-field splitting (ZFS) interaction. Natural-abundance gadolinium is a mixture of many different isotopes, with six of those isotopes accounting for nearly 100% of natural-abundance gadolinium. Of those six isotopes, only two of them (gadolinium-155 and gadolinium-157) have nuclear spin. Both of the magnetic isotopes have a nuclear spin $I = 3/2$ and together the two isotopes account for about 30% of the total natural abundance gadolinium. However, a hyperfine term is not included in the spin Hamiltonian of equation 5.1 because the magnitude of the gadolinium hyperfine interaction is usually much less than the electron Zeeman and ZFS interactions, so the effect on the observed lineshape is merely a slight broadening of the linewidth. The nuclear Zeeman interaction is also negligible compared to the electron Zeeman and hyperfine interactions and so is neglected as well. If there are significant ligand interactions, those terms may be included also.

In equation 5.1, D is the ZFS tensor that was introduced in chapter 2. The D-tensor is traceless and is often parameterized by the axial and rhombic ZFS parameters D and E such that, in the frame that diagonalizes the D-tensor, the elements of D are

$$D = \begin{bmatrix} D_x & 0 & 0 \\ 0 & D_y & 0 \\ 0 & 0 & D_z \end{bmatrix} = \begin{bmatrix} -\frac{1}{3}D + E & 0 & 0 \\ 0 & -\frac{1}{3}D - E & 0 \\ 0 & 0 & \frac{2}{3}D \end{bmatrix}. \tag{5.2}$$

It is unfortunate that, by convention, the axial ZFS parameter D and ZFS-tensor D are designated by the same variable "D". To stick with convention, the two separate objects will be indicated by the same variable in this work as well. To avoid ambiguity, the object to which D refers will be stated explicitly when it is not clear from context.

Spin-state energy level diagrams like those in figures 3.2 and 4.1 are difficult to construct for high-spin $S = 7/2$ gadolinium(III) systems, but figure 5.1 shows a field-dependent energy level diagram for a simulated gadolinium(III) system with isotropic g-value of $g = 2$ and axial ZFS of 1000 MHz (i.e. $D = 1000$ MHz and $E = 0$). Note that, even in the absence of an external field (i.e. $B_0 = 0$), there is a lifting of degeneracy of the spin state energies. The m_S values in figure 5.1 only make sense as state labels for fields where the electron Zeeman splitting is much greater than the zero-field splitting.

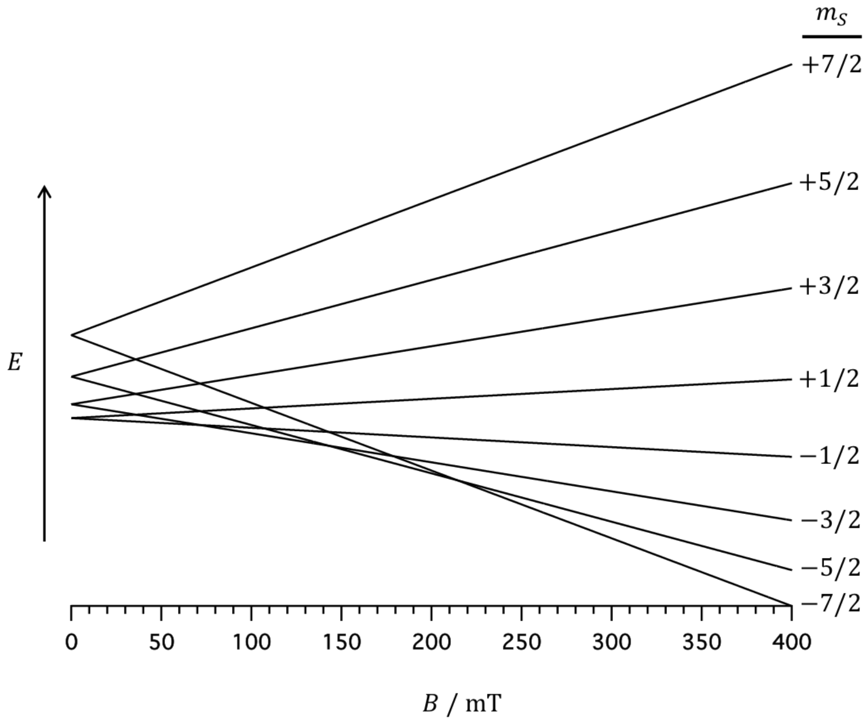

Figure 5.1: Simulated field-dependent energy level diagram of a single orientation of a $S = 7/2$ gadolinium(III) system with axial zero-field splitting and isotropic g-tensor. Theses splittings correspond to the external field oriented along the axis of axial symmetry. This system has isotropic $g = 2$ and axial ZFS $D = 1000$ MHz.

5.3 Lineshapes of gadolinium(III) compounds

5.3.1 Rigid limit

A set of rigid-limit simulations using the spin Hamiltonian of equation 5.1 is shown in figure 5.2 for a gadolinium(III) system with isotropic g-value $g = 2$ and axial ZFS parameter $D = 500$ MHz. The simulations in figures 5.2**c** and 5.2**d** include rhombic ZFS parameter

$E = 50$ MHz as well. All four simulations are convoluted with a 5 mT FWHM Gaussian to account for non-specific inhomogeneous line broadening.

According to the energy level diagram of figure 5.1, gadolinium(III) systems have seven allowed electronic spin-state transitions where $\Delta m_S = \pm 1$. Figures 5.2**b** and 5.2**d** show individual contributions to the spectra due those seven transitions. Experimental gadolinium(III) lineshapes may include additional contributions from formally forbidden double quantum transitions, but the simulations in figure 5.2 do not include those components.

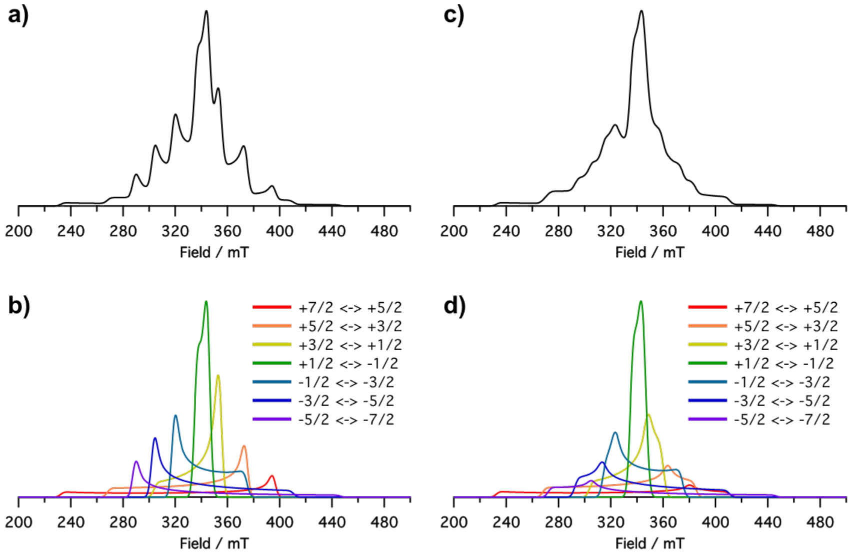

Figure 5.2: Zero-harmonic rigid-limit simulations for a gadolinium(III) system with isotropic $g = 2$, axial ZFS parameter $D = 500$ MHz, and rhombic ZFS parameter $E = 0$ (panels **a** and **b**) or $E = 50$ MHz (panels **c** and **d**). Panels **a** and **c** show the full lineshape as would be observed by experiment. Panels **b** and **d** show the components of the total lineshape that are due to each individual allowed transition $\Delta m_S = \pm 1$. All simulations are convoluted with a 5 mT FWHM Gaussian broadening.

Note that these rigid-limit simulations are displayed as integrated lineshapes, which is reminiscent of how the absorption spectra would appear. This was done in order to better illustrate how the complex lineshapes of figures 5.2**a** and 5.2**c** are due to the overlap of the individual components.

Simulations using parameters identical to those in the simulations of figures 5.2**a** and 5.2**c** are shown in figure 5.3, but as the experimentally familiar derivative lineshapes rather than absorption lineshapes. The derivative lineshapes are quite complex, even in the rigid limit.

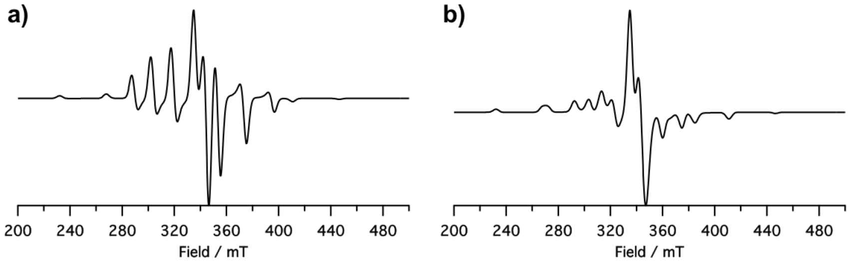

Figure 5.3: Derivative lineshapes of the simulations shown in figure 5.2. Panel **b** here corresponds to panel **c** in figure 5.2, whereas panel **a** corresponds to the same spectrum in both figures.

5.3.2 Isotropic limit

A simulation of the same gadolinium(III) system in figures 5.2 and 5.3 is shown in figure 5.4 for the isotropic limit. Indeed, the spectrum consists of a single line because the dipolar ZFS interaction has completely averaged out. In this case, the spin-state energies are evenly separated and therefore all seven allowed transitions occur at the same energy. For both the purely axial ZFS case ($E = 0$) and the rhombic case ($E = 50$ MHz), the isotropic lineshape is the same.

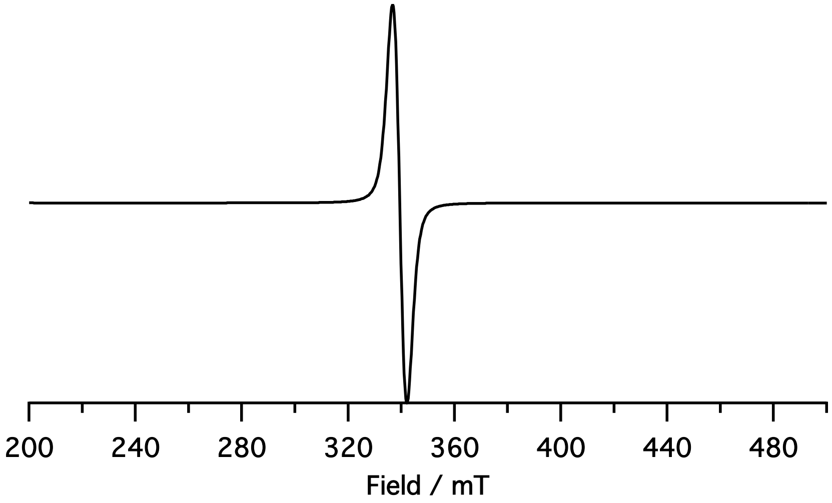

Figure 5.4: Isotropic-limit simulation of the same gadolinium(III) system shown in figures 5.2 and 5.3. The dipolar ZFS interaction has completely averaged out.

5.3.3 *Fast-motion and slow-motion regimes*

The isotropic lineshape in figure 5.4 is clearly different from the rigid limit lineshapes in figure 5.3. Figure 5.5 shows the evolution of the gadolinium(III) lineshape as the rate of rotational motion increases from the rigid limit to the isotropic limit (i.e. as τ_c decreases).

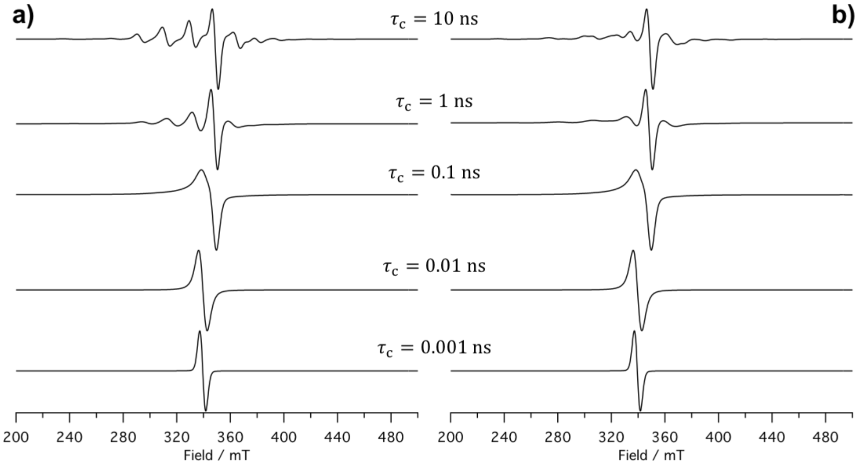

Figure 5.5: A series of SLE simulations over a range of rotational correlation times for the same gadolinium(III) system shown in figure 5.3. The spectra in **a** have fully axial ZFS ($E = 0$) and the spectra in **b** have a rhombic component ($E = 50$ MHz).

Down to $\tau_c = 1$ ns, the lineshapes appear to be in the slow-motion regime. Even at the longest rotational correlation time of 10 ns, there are noticeable differences in the lineshapes compared to the rigid limit simulations. In particular, the side peaks on either side of the central transition have begun to broaden out, more so on the high-field side of the spectra. At $\tau_c = 1$ ns, the peaks due to the non-central transitions still have appreciable intensities.

At $\tau_c = 0.1$ ns, the lineshape is in the fast-motion regime. The rotational motion is rapid enough that most of the ZFS interaction has averaged out, but the rotational motion is still somewhat coupled to the spin-state energies. By $\tau_c = 0.01$ ns, both spectra consist of a single peak as in the isotropic limit.

5.3.4 *Distribution of ZFS parameters*

The simulated spectra presented in this chapter so far are all for systems with a single ZFS D-tensor. In reality, the D-tensor values are highly dependent on molecular geometry and solvent environment [88], so a solution sample consists of a distribution of D-tensors that corresponds to a distribution of molecular environments and configurations. The exact nature of a ZFS distribution for any given sample is difficult to determine. Several methods have been developed to model ZFS distributions, but most gadolinium(III) data analysis has assumed Gaussian distributions (with mixed success) [90, 91]. The problem is further complicated by the fact that theoretical first-principles quantum chemistry calculations of ZFS values for metallic systems are generally inaccurate, although this is an active area of research [92, 93, 94, 95].

Figure 5.6 shows a set of rigid-limit simulations to illustrate the effect that a distribution of D-tensor values has on the overall lineshape compared to a system with a single D-tensor. The top simulation is for a system with a Gaussian distribution of purely axial D-tensors with the maximum D-value of the distribution being $D = 500$ MHz and the FWHM width of the distribution being $\sigma = 300$ MHz. The other simulations show lineshapes for systems with a single D-tensor. All of the simulations have isotropic $g = 2$ and are convoluted with a 5 mT FWHM Gaussian broadening.

The distribution lineshape is markedly distinct from the single-D-value lineshapes, as are the single-D-value lineshapes from each other. The large distribution of D-values results in significant broadening of all peaks in the spectrum, particularly the non-central transition peaks. Distributions in ZFS values must be taken into account to make sense of most solution spectra of gadolinium(III) compounds.

5.4 Determination of measurement parameters

For the purposes of this study, a compound with the following properties was sought: relatively small ZFS, mostly axial ZFS, and already well-characterized. A small ZFS was desired so that it would be practical to measure the entire lineshape. Larger splittings broaden the spectral width, which increases measurement time to capture the whole spectrum or can even result in resonance fields that are greater than the maximum field that the X-band magnet could produce. Axial ZFS splitting was desired for simplicity, as a system with $E = 0$ has fewer parameters to fit. Finally, a compound that has already been well-studied by the EPR community was desired so that there would be a benchmark with which to compare the slow-motion data, as fitting entire slow-motion lineshapes for gadolinium(III) compounds is a problem that has not been solved in general.

There are a multitude of gadolinium(III) chelates that are available for purchase or that can be synthesized [78], but Gd-DOTA (DOTA = 1,4,7,10-tetraazacyclododecane-1,4,7,10-tetraacetic acid) was chosen for the temperature series measurement in this study because

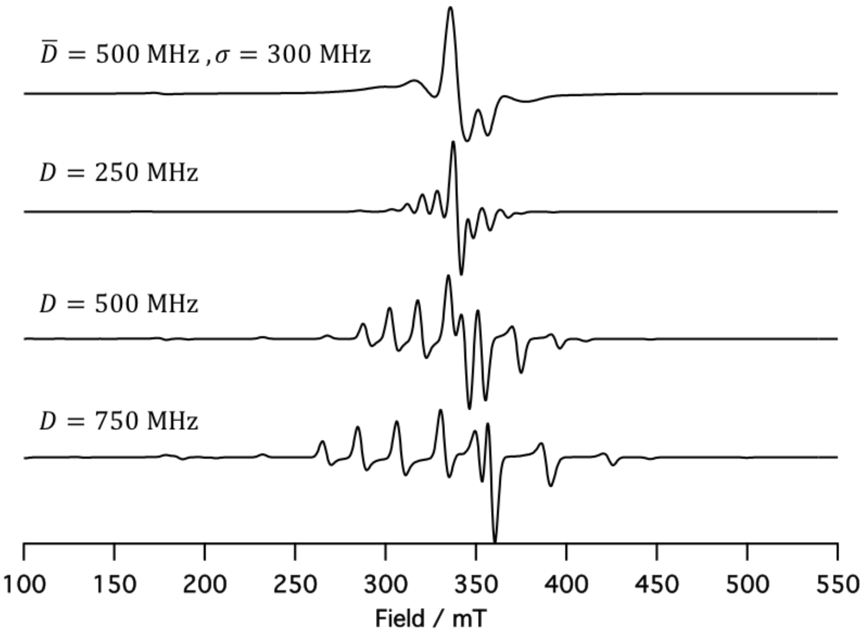

Figure 5.6: A series of rigid-limit simulations for a gadolinium(III) system with isotropic $g = 2$ and various axial ZFS values. The top simulation is for a sample with a Gaussian distribution of D-values with a mean value of 500 MHz and width of 300 MHz. The other simulations show how distinct different components of the distribution lineshape can be. All simulations are also convoluted with a 5 mT FWHM Gaussian broadening to increase the linewidths.

it mostly meets the criteria listed above. Literature on EPR studies of solution Gd-DOTA report ZFS D-values in the 600s of MHz and E-values in the 100s of MHz, with large D- and E-distribution widths [96, 97, 88]. Variations in reported values are likely due to differences in solution composition. Many metallic spin systems have ZFS on the order of GHz, so 600 MHz is a relatively small magnitude for the ZFS interaction. A representation of the Gd-DOTA chelate is shown in figure 5.7.

5.4.1 Sample preparation

Synthesis

Solid $GdCl_3$ and DOTA powders were purchased separately from a reputable supplier. Gd-DOTA was made by dissolving DOTA and $GdCl_3$ in nanopure water in a 10:1 molar ratio

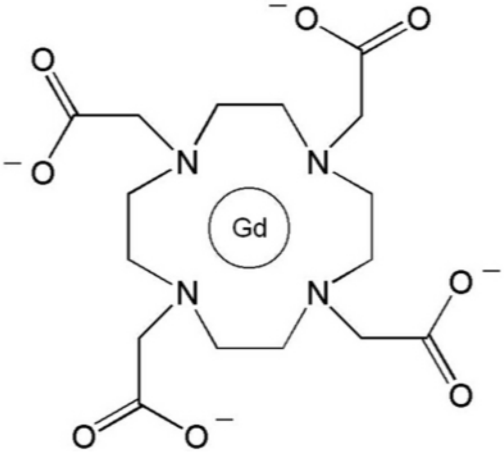

Figure 5.7: Cartoon representation of Gd-DOTA. The gadolinium(III) ion is eight-coordinate, with seven positions thought to be coordinated to oxygen and nitrogen from DOTA and the eighth position to a water molecule in aqueous solution.

of DOTA:$GdCl_3$ in order to ensure full complexation of gadolinium(III) ion. The aqueous solution was allowed to stir at room temperature for several hours. From this stock solution of Gd-DOTA, 40% by volume glycerol aqueous solutions of varying concentration in Gd-DOTA were made for measurement. Samples were prepared by transferring the Gd-DOTA solutions to 1.5 mm inner diameter quartz EPR tubes. All solutions were stored in a dark -80° C freezer for future use.

Concentration

Higher concentrations of Gd-DOTA produce larger EPR signals, but if the concentration is too high then the spin magnetic moments on separate Gd-DOTA molecules may interact and lead to dipolar broadening, which is not modeled in the slow-motion simulations. In order to measure spectra with good signal-to-noise ratios but no dipolar interactions, a concentration series was made to determine if dipolar broadening would occur.

Studies on $GdCl_3$ suggest that dipolar broadening is negligible below a concentration of 2.0 mM [98]. Because similar studies were not found for Gd-DOTA, a more conservative concentration series of 0.5 mM, 1.0 mM and 1.5 mM was produced for measurement. Normalized X-band measurements for each concentration are shown in figure 5.8.

The signal-to-noise ratio improves as the concentration increases. There are slight differences

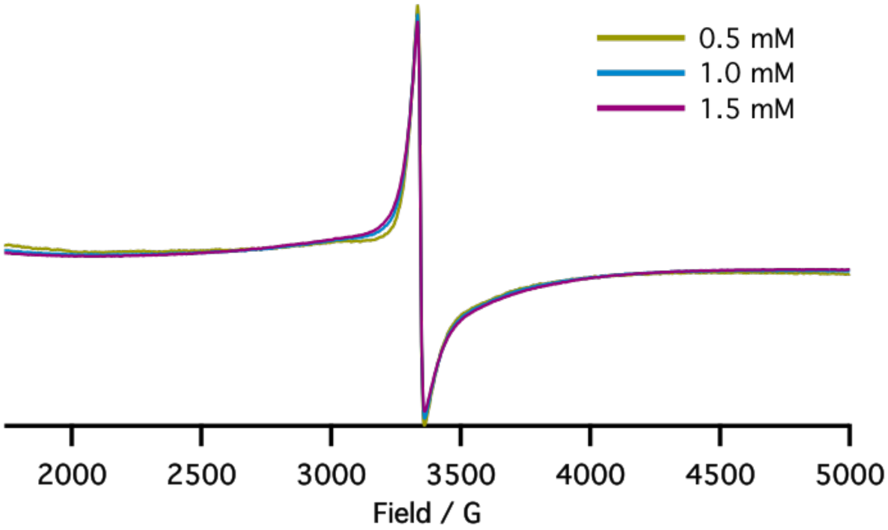

Figure 5.8: Frozen X-band CW EPR spectra measured for Gd-DOTA in 40% glycerol solution at 150 K with a microwave frequency of 9.32 GHz. The spectra are normalized to all have the same total intensity. There appears to be no significant dipolar broadening even up to 1.5 mM, but the signal-to-noise ratio is best for for 1.5 mM sample. The spectra are not background corrected.

in the lineshapes for each concentration. In particular, there appears to be minor broadening in the baseline region on the low-field side of the central transition peak. However, the baselines of each concentration spectrum are not equivalent, as evidenced by the baseline mismatch below 2000 G. Therefore, it is unlikely that the apparent broadening is actually due to dipolar coupling between Gd-DOTA molecules, as such an interaction would affect more of the lineshape. The signal-to-noise ratio increases with Gd-DOTA concentration, so a concentration of 1.5 mM Gd-DOTA was chosen for subsequent experimental measurements.

Microwave power

Signal intensity is affected by the incoming B_1 microwave field power. Ideally, a microwave power that maximizes signal intensity without saturating the sample is desired. When saturation occurs, the lineshape is affected in ways that are not accounted for in the model of the general SLE solver. To determine a suitable microwave power for the temperature series measurements, a power series was measured at temperatures of 150 K and 293 K, and with a modulation amplitude of 5 G.

Figure 5.9 shows the power saturation curves for Gd-DOTA at both 150 K and 293 K. At 150 K, the sample is frozen and saturation occurs at lower powers than the room temperature sample. To be sure that there is no saturation, a microwave power in the linear region of the curves in figure 5.9 must be chosen. According to the power saturation curves, significant saturation occurs at microwave powers just above 2 mW in the 150 K sample, while there appears to be no saturation in the room temperature sample even up to 7 mW of microwave power. To be conservative, a microwave power of 2.02 mW was used in all subsequent temperature series measurements.

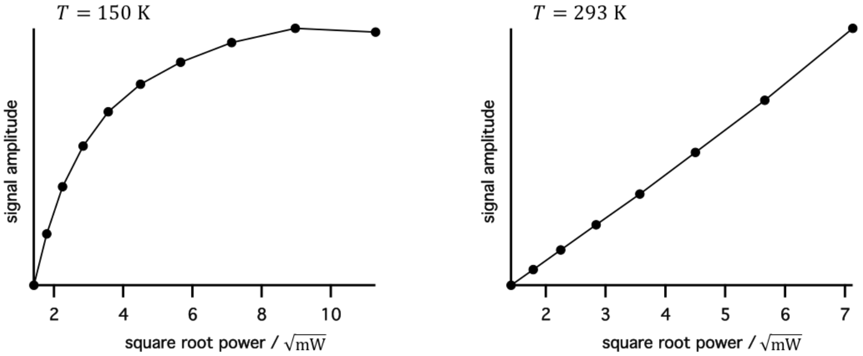

Figure 5.9: Power saturation curves for 1.5 mM Gd-DOTA at X-band. At 150 K, significant saturation begins to occur above 2 mW of microwave power. At room temperature, there appears to be no saturation even up to 7 mW of microwave power.

Modulation amplitude

Another experimental parameter that affects signal intensity is the external field modulation amplitude. Higher modulation amplitudes increase the signal intensity, but if the modulation amplitude is too high then certain features of the lineshape may be distorted or lost altogether.

A series of X-band Gd-DOTA spectra were measured from a range of 2 G to 15 G modulation amplitudes with a microwave frequency of 9.32 GHz. All spectra in the series were measured at 150 K and 2.02 mW of microwave power. The spectra at 2 G, 10 G, and 15 G modulation amplitudes are shown in figure 5.10.

Figure 5.10**a** illustrates how the modulation amplitude can increase the EPR signal. For the same number of scans, the 10 G and 15 G spectra are far more intense than the 2 G spectrum. Figure 5.10**b** shows all three spectra normalized to have equal intensity so that

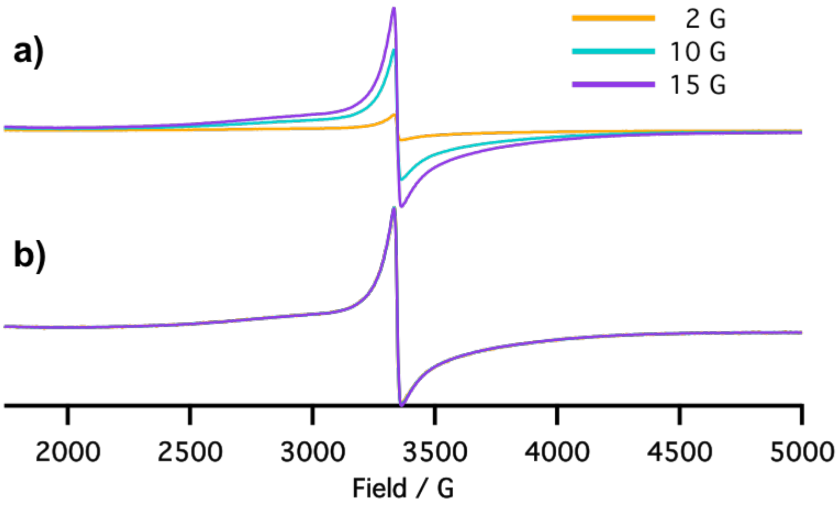

Figure 5.10: Frozen X-band Gd-DOTA spectra measured with three different modulation amplitudes. The raw data is shown in **a** and the normalized data is shown in **b**. The normalized spectra are nearly identical.

any distortions that may occur at higher modulation amplitudes are easier to observe. The normalized spectra appear to be identical, which suggests that even up to 15 G modulation amplitude the X-band Gd-DOTA lineshape is not distorted. Because a modulation amplitude series was not measured at temperatures above 150 K, a conservative modulation amplitude of 8 G was chosen for the temperature series measurements.

5.5 Gd-DOTA frozen data

In order to fit the motional Gd-DOTA spectra to determine the temperature-dependence of the rotational correlation time, the spin Hamiltonian tensor values must be determined from frozen spectra in which the lineshape is not affected by molecular dynamics. In the case of Gd-DOTA, which is described by the spin Hamiltonian in equation 5.1, the parameters to determine from the frozen spectrum are the g-tensor and ZFS D-tensor values.

A frozen X-band spectrum of Gd-DOTA was measured at 200 K with a microwave frequency of 9.32 GHz using the experimental parameters outlined above. The background-corrected 200 K spectrum is shown in figure 5.11. The central transition at around 350 mT is prominent, but features due to the other transitions are almost completely broadened out, save for the broad feature on the low-field side of the central transition, at about 250 mT.

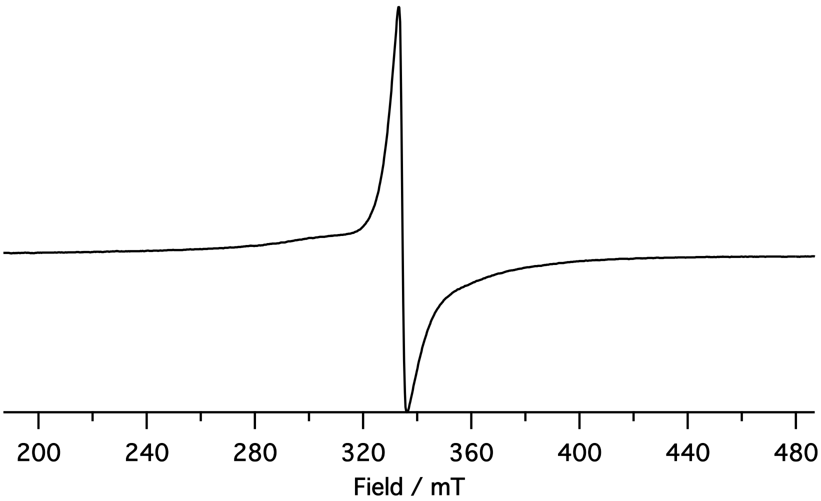

Figure 5.11: Frozen X-band spectrum of 1.5 mM Gd-DOTA in 40% glycerol solution measured at 200 K with a microwave frequency of 9.32 GHz.

The g-tensor for gadolinium(III) compounds is isotropic due to the spherically symmetric spatial distribution of the seven half-filled gadolinium(III) $4f$-orbitals. Because the sample has a distribution of D-tensors, it is difficult to precisely determine the g-factor of Gd-DOTA from just a frozen X-band spectrum alone because the ZFS affects peak positions. Therefore, a g-value of $g = 1.992$ was assumed for Gd-DOTA in this study based on previously reported literature values for this gadolinium(III) chelate [90].

5.5.1 D and E distributions

Unfortunately, determining the distribution of ZFS values in the Gd-DOTA sample is not straightforward. A Gaussian distribution could be assumed, but such a distribution is based more on a fondness and familiarity of the normal distribution rather than good physical evidence that such a distribution makes sense for Gd-DOTA in aqueous glycerol, or for any other system with a distribution of ZFS values for that matter.

Rather than assume any particular distribution, a model-free distribution was constructed from the data using a method similar to that presented for ZFS distributions in iron(III) compounds [91]. The method is a constrained linear least-squares fit of simulated spectra to the frozen experimental data in figure 5.11 according to the following equation:

$$C\vec{w} = \vec{s}. \tag{5.3}$$

In equation 5.3, C is a matrix in which each column is a simulated Gd-DOTA spectrum that corresponds to a particular D- and E-value, $\vec{s}$ is the experimental data, and $\vec{w}$ is a vector of weights that best fit the data in $\vec{s}$ using the simulated spectra in C. The set of weights in $\vec{w}$ define the distribution. The only constraint on the weights is that they be nonnegative. In this manner, no prior knowledge or assumption about the distribution is required to fit the data, other than the range of D- and E-values that are chosen to construct C.

The matrix C of simulated rigid-limit Gd-DOTA spectra was constructed by computing spectra with axial ZFS D-values ranging from 12 MHz to 1800 MHz in 12 MHz increments. For each D-value, spectra with E-values ranging from 0 to $D/3$ were computed. To reduce computational cost and data storage, each simulated spectrum has its own Gaussian D-distribution centered at the D-value of the simulation with a width of 36 MHz.

5.5.2 Rigid-limit fit

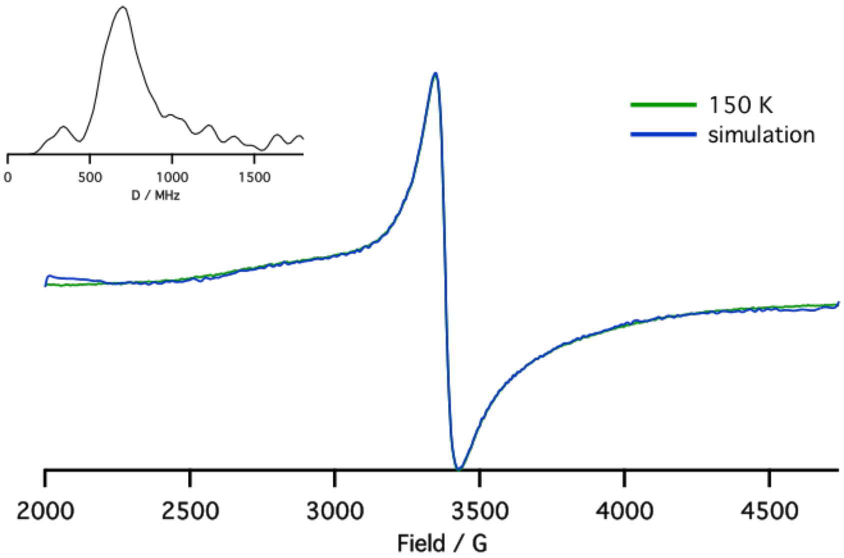

Figure 5.12: Model-free constrained linear least-squares fit to frozen Gd-DOTA data. The inset shows the distribution of axial ZFS D-values determined from the least-squares fit. The data measured at 150 K is shown in green and the fit is shown in blue.

The ZFS distribution fit is shown in figure 5.12 along with the distribution of axial ZFS D-values determined according to equation 5.3. The fit is quite good except for at the ends of the spectrum, which is probably due to convolution artifacts. The D-value distribution is not Gaussian, but the main feature of the distribution would probably be well approximated by a Gaussian function. The maximum of the distribution is just over 600 MHz, which agrees with other published values of the ZFS in Gd-DOTA. There is also significant population of ZFS that is much greater than 600 MHz according to this model-free distribution. The distribution in figure 5.12 fits the frozen data well, but it is unknown if the liquid solution is well-described by the same distribution or if the distribution in the liquid sample is temperature-dependent.

5.6 Temperature series measurements

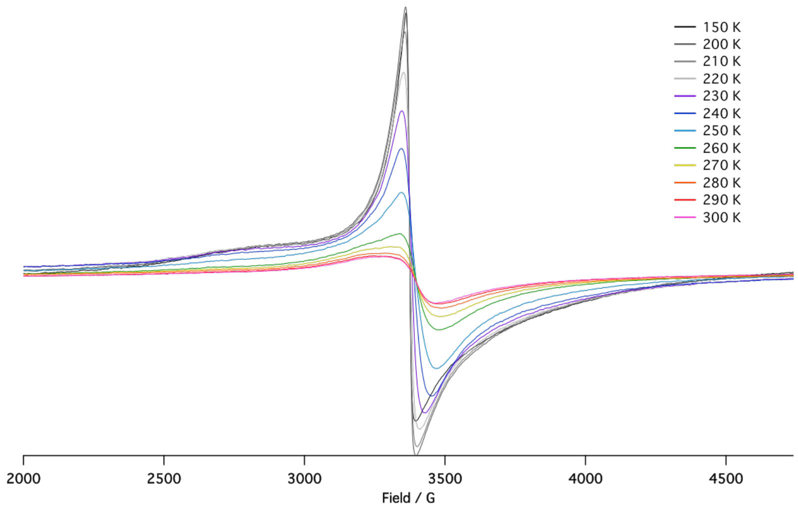

Figure 5.13: Temperature series X-band measurements of 1.5 mM Gd-DOTA in 40% glycerol, measured at 9.32 GHz microwave frequency. The grey temperatures correspond to spectra of the frozen sample and the colored temperatures correspond to spectra of the sample in the liquid state. All spectra are background-corrected and scaled only according to the number of scans.

To determine the effect that changes in rotational dynamics have on the lineshape of Gd-DOTA, one sample was measured over a range of temperatures from 150 K to 300 K. For each temperature at which the sample was in the liquid state, the experimental spectrum would be fit using the general SLE solver with isotropic $g = 1.992$ and the ZFS distribution determined from the frozen spectrum in figure 5.12. The unscaled temperature series data is shown in figure 5.13.

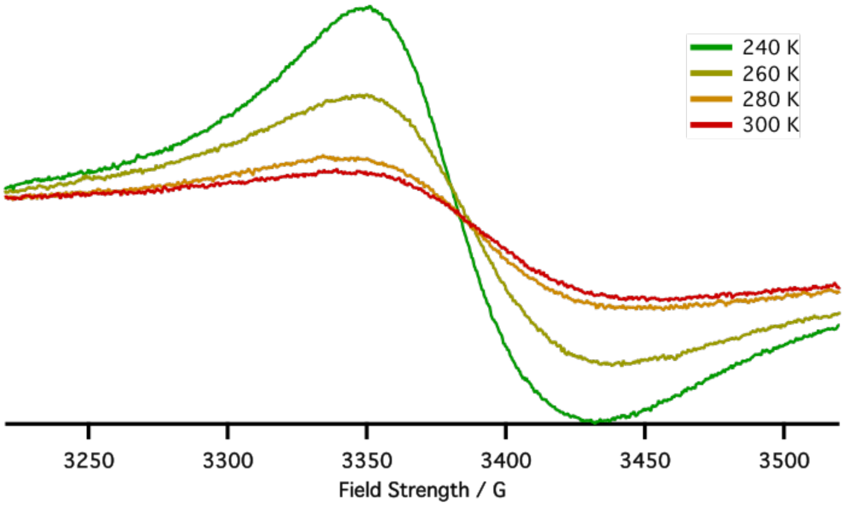

Figure 5.14: Zoomed-in view of the central transition peaks of selected temperatures from the spectra in figure 5.13. The peak broadens and shifts to higher fields with increasing temperature. The change in lineshape from 280 K to 300 K is relatively minor, which suggests that the higher-temperature spectra may be approaching the isotropic limit.

As expected, the intensities decrease as the temperature increases, which makes it difficult to observe lineshape differences among the spectra in the unscaled plots. A zoomed-in view of the central transition of some of the motional spectra are shown in figure 5.14. As the temperature increases from 240 K to 300 K, the position of the central transition appears to shift toward higher fields. Assuming that the ZFS distribution and g-value does not change with temperature, then the lineshift could be due to changes in the rotational correlation time. The 280 K and 300 K lineshapes are very similar, which suggests that the sample is approaching the isotropic limit at room temperature. The lower temperature spectra at 260 K and 240 K are probably representative of the X-band slow-motion lineshape.

5.6.1 Attempted motional fits

To fit the motional Gd-DOTA spectra, the ZFS distribution determined by equation 5.3 for the frozen 150 K spectrum was assumed to be valid for the liquid state sample at all temperatures. Unfortunately, the motional fits are very poor. An example is shown in figure 5.15 for the presumably slow-motion spectrum measured at 240 K.

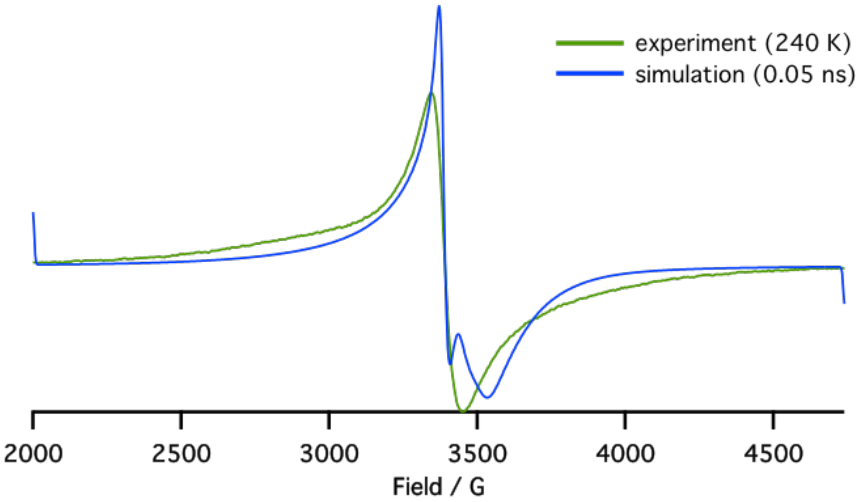

Figure 5.15: Slow-motion fit of the experimental 240 K Gd-DOTA X-band spectrum. The ZFS value distribution used for the fit is the same as the distribution that was determined for the experimental frozen 150 K spectrum. The rotational correlation time for the fit is $\tau_c = 0.05$ ns.

The central transition of the fit is far too narrow and has too much resolved structure compared to the data. The simulated spectrum also lacks the broad intensity on either side of the central transition that is present in the experimental spectrum. Additional Gaussian convolutional broadening could be introduced to the simulation, but in that case the data could be well-fit using a wide array of pairs of Gaussian linewidth and τ_c parameters, which would render the determination of the actual τ_c impossible.

5.7 Conclusions

Although the general SLE solver can be used to simulate spectra of high-spin systems with the correct features for the spin Hamiltonian in equation 5.1, the actual Gd-DOTA sample has bulk properties (i.e. conformational and ZFS distributions) that are not directly accounted for in the general SLE solver as outlined in chapter 2. Modeling of the ZFS distribution must somehow be combined with the SLE model of rotational diffusion. It is also likely that there are other dynamic processes besides rotation that contribute to the Gd-DOTA motional lineshape, such as conformational changes [33]. The general SLE solver would need to be expanded to include dynamic processes other than rotation.

BIBLIOGRAPHY

[1] E. K. Zavoisky. Paramagnetic relaxation of liquid solutions for perpendicular fields. *J. Phys.*, 9:211–216, 1944.

[2] E. K. Zavoisky. Paramagnetic absorption in some salts in perpendicular magnetic fields. *J. Phys.*, 10:170–173, 1945.

[3] M. M. Roessler and E. Salvadori. Principles and applications of EPR spectroscopy in the chemical sciences. *Chem. Soc. Rev.*, 47:2534–2553, 2018.

[4] S. Kempe, H. Metz, and K. Mader. Application of electron paramagnetic resonance (EPR) spectroscopy and imaging in drug delivery research - chances and challenges. *Eur. J. Pharm. Biopharm.*, 74:55–66, 2010.

[5] I. D. Sahu, R. M. McCarrick, and G. A. Lorigan. An advanced approach to the evaluation of the spin-rotational term for a nitronyl nitroxide in fluid solution. *Biochemistry*, 52:5967–5984, 2013.

[6] J. Niklas and O. G. Poluektov. Charge transfer processes in opv materials as revealed by EPR spectroscopy. *Adv. Energy Mater.*, 7, 2017.

[7] M. Ikeya. Electron spin resonance (ESR) microscopy in materials science. *Annu. Rev. Mater. Sci.*, 21:45–63, 1991.

[8] L. D. Bogomolova, V. A. Zhachkin, and T. K. Pavlushkina. Use of electron paramagnetic resonance for investigating glasses and raw materials (review). *Glass. Ceram.*, 72:117–122, 2015.

[9] S. K. Misra. Quantum computing/quantum information processing in view of electron magnetic/electron paramagnetic resonance technique/spectroscopy. *Biol. Magn. Reson.*, 31:1–23, 2016.

[10] H. Matsuoka and O. Schiemann. Molecular spins in biological systems. *Biol. Magn. Reson.*, 31:51–77, 2016.

[11] S. Yamamoto, S. Nakazawa, K. Sugisaki, K. Sato, K. Toyota, D. Shiomi, and T. Takeji. Adiabatic quantum computing on molecular spin quantum computers. *Biol. Magn. Reson.*, 31:79–118, 2016.

[12] P. J. Mohr, D. B. Newell, and B. N. Taylor. The 2014 codata recommended values of the fundamental physical constants (web version 7.2).

[13] J. A. Weil and J. R. Bolton. *Electron Paramagnetic Resonance: Elementary Theory and Practical Applications.* John Wiley Sons, Inc., Hoboken, New Jersey, 2007.

[14] A. Lund, M. Shiotani, and S. Shimada. *Principles and Applications of ESR Spectroscopy.* Springer, 2011.

[15] F. Neese. Spin-hamiltonian parameters from first principle calculations: Theory and application. *Biol. Magn. Reson.*, 28, 2009.

[16] S. Stoll and D. Goldfarb. EPR interactions - nuclear quadrupole couplings. *eMagRes*, 6:495–510, 2017.

[17] A. G. Redfield. On the theory of relaxation processes. *IBM Journal*, 1:19–31, 1957.

[18] R. Kubo. Statistical-mechanical theory of irreversible processes. I. *J. Phys. Soc. Jpn.*, 12:570–586, 1957.

[19] R. Kubo. A stochastic theory of line shape. *Adv. Chem. Phys.*, 15:101–127, 1969.

[20] J. H. Freed. *Spin Labeling: Theory and Applications.* Academic Press: New York, 1976.

[21] D. J. Schneider and J. H. Freed. Spin relaxation and motional dynamics. *Adv. Chem. Phys.*, 73:387–527, 1989.

[22] D. J. Schneider and J. H. Freed. Calculating slow motional magnetic resonance spectra: A user's guide. *Biol. Magn. Reson.*, 8:1–76, 1989.

[23] H. Steinhoff and W. L. Hubbell. Calculation of paramagnetic resonance spectra from brownian dynamics trajectories: Application to nitroxide side chains in proteins. *Biophys. J.*, 71:2201–2212, 1996.

[24] P. Håkansson, P. O. Westlund, E. Lindahl, and O. Edholm. A direct simulation of EPR slow-motion spectra of spin labelled phospholipids in liquid crystalline bilayers based on a molecular dynamics simulation of the lipid dynamics. *Phys. Chem. Chem. Phys.*, 3:5311–5319, 2001.

[25] G. Moro and J. H. Freed. Calculation of ESR spectra and related Fokker-Planck forms by the use of the Lanczos algorithm. *J. Chem. Phys.*, 74:3757–3773, 1981.

[26] J. H. Freed, G. V. Bruno, and C. F. Polnaszek. Electron spin resonance line shapes and saturation in the slow motional region. *J. Phys. Chem.*, 75:3385–3399, 1971.

[27] E. Meirovitch, D. Igner, E. Igner, G. Moro, and J. H. Freed. Electron-spin relaxation and ordering in smectic and supercooled nematic liquid crystals. *J. Chem. Phys.*, 77:3915–3938, 1982.

[28] M. Zerbetto, A. Polimeno, and V. Barone. Simulation of electron spin resonance

spectroscopy in diverse environments: An integrated approach. *Comp. Phys. Comm.*, 180:2680–2697, 2009.

[29] H. J. Hogben, M. Krzystyniak, G. T. P. Charnock, P. J. Hore, and I. Kuprov. Spinach - a software library for simulation of spin dynamics in large systems. *J. Magn. Reson.*, 208:179–194, 2011.

[30] J. R. Norris and S. I. Weissman. Studies of rotational diffusion through the electron-electron dipolar interaction. *J. Phys. Chem.*, 73:3119–3124, 1969.

[31] F. B. Bramwell. ESR studies of phosphorescent corannulene; evidence for pseudorotation. *J. Chem. Phys.*, 52:5656–5661, 1970.

[32] A. Blank and H. Levanon. Triplet line shape simulation in continuous wave electron paramagnetic resonance experiments. *Concepts Magn. Reson.*, 25A:18–39, 2005.

[33] A. Borel, R. B. Clarkson, and R. L. Belford. Stochastic Liouville equation treatment of the electron paramagnetic resonance line shape of an s-state ion in solution. *J. Chem. Phys.*, 126:054510, 2007.

[34] S. Stoll and A. Schweiger. Easyspin: Simulating cw ESR spectra. *Biol. Magn. Reson.*, 27:299–321, 2007.

[35] L. D. Favro. *Fluctuation Phenomena in Solids*, chapter Rotational Brownian Motion, pages 79–101. Academic Press: New York, 1965.

[36] R. Tarroni and C. Zannoni. On the rotational diffusion of asymmetric molecules in liquid crystals. *J. Chem. Phys.*, 95:4550–4564, 1991.

[37] K. A. Earle, D. E. Budil, and J. H. Freed. 250-GHz EPR of nitroxides in the slow-motional regime: Models of rotational diffusion. *J. Phys. Chem.*, 97:13289–13297, 1993.

[38] G. Moro and J. H. Freed. Efficient computation of magnetic resonance spectra and related correlation functions from stochastic Liouville equations. *J. Phys. Chem.*, 84:2837–2840, 1980.

[39] C. F. Polnaszek, G. V. Bruno, and J. H. Freed. ESR line shapes in the slow-motional region: Anisotropic liquids. *J. Chem. Phys.*, 58:3185–3199, 1973.

[40] A. V. Bogdanov and A. K. Vorobiev. Orientation order and rotation mobility of nitroxide biradicals determined by quantitative simulation of EPR spectra. *Phys. Chem. Chem. Phys.*, 18:31144–31153, 2016.

[41] S. K. Misra. Simulation of slow-motion CW EPR spectrum using stochastic Liouville equation for an electron spin coupled to two nuclei with arbitrary spins: Matrix elements of the Liouville superoperator. *J. Magn. Reson.*, 189:59–77, 2007.

[42] L. J. Edwards, D. V. Savostyanov, A. A. Nevzorov, M. Concistre, G. Pileio, and I. Kuprov. Grid-free powder averages: On the applications of the Fokker-Planck equation to solid state NMR. *J. Magn. Reson.*, 235:121–129, 2013.

[43] R. N. Zare. *Angular momentum: understanding spatial aspects in chemistry and physics.* Wiley, 1998.

[44] A. R. Edmonds. *Angular Momentum in Quantum Mechanics.* Princeton University Press, 1996.

[45] S. Lee, D. E. Budil, and J. H. Freed. Theory of two-dimensional Fourier transform electron spin resonance for ordered and viscous fluids. *J. Chem. Phys.*, 101:5529–5558, 1994.

[46] A. Polimeno and J. H. Freed. Slow motional ESR in complex fluids: The slowly relaxing local structure model of solvent cage effects. *J. Phys. Chem.*, 99:10995–11006, 1995.

[47] R. Kubo and K. Tomita. A general theory of magnetic resonance. *J. Phys. Soc. Jpn.*, 9:888–919, 1954.

[48] K. A. Earle and D. E. Budil. Calculating slow-motion ESR spectra of spin-labeled polymers. pages 53–84, 2006.

[49] K. V. Vasavada, D. J. Schneider, and J. H. Freed. Calculation of ESR spectra and related Fokker-Planck forms by the use of the Lanczos algorithm. II. criteria for truncation of basis sets and recursive steps utilizing conjugate gradients. *J. Chem. Phys.*, 86:647–661, 1987.

[50] J. R. Biller, V. M. Meyer, H. Elajoili, G. M. Rosen, and S. S. Eaton. Frequency dependence of electron spin relaxation times in aqueous solution for a nitronyl nitroxide radical and perdeuterated-tempone between 250 MHz and 34 GHz. *J. Magn. Reson.*, 225:52–57, 2012.

[51] J. R. Biller, H. Elajaili, V. Meyer, G. M. Rosen, and S. S. Eaton. Electron spin-lattice relaxation mechanisms of rapidly-tumbling nitroxide radicals. *J. Magn. Reson.*, 236:47–56, 2013.

[52] J. H. Osiecki and E. F. Ullman. Studies of free radicals. I. α-nitronyl nitroxides, a new class of stable radicals. *J. Am. Chem. Soc.*, 90:1078–1079, 1968.

[53] D. G. B. Boocock, R. Darcy, and E. F. Ullman. Studies of free radicals. II. chemical properties of nitronylnitroxides. a unique radical anion. *J. Am. Chem. Soc.*, 90:5945–5946, 1968.

[54] D. G. B. Boocock and E. F. Ullman. Studies of free radicals. III. a 1,3-dioxy-2-imidazolidone zwitterion and its stable nitronyl nitroxide radical anion. *J. Am. Chem. Soc.*, 90:6873–6874, 1968.

[55] R. W. Kreilick, J. Becher, and E. F. Ullman. Electron spin resonance studies of nitronylnitroxide radicals with asymmetric centers. *J. Am. Chem. Soc.*, 91:5121–5124, 1969.

[56] E. F. Ullman, J. H. Osiecki, D. G. B. Boocock, and R. Darcy. Studies of stable free radicals. x. nitronyl nitroxide monoradicals and biradicals as possible small molecule spin labels. *J. Am. Chem. Soc.*, 94:7049–7059, 1972.

[57] A. Collauto, A. Barbon, and M. Brustolon. First determination of the spin relaxation properties of a nitronyl nitroxide in solution by electron spin echoes at X-band: A comparison with tempone. *J. Magn. Reson.*, 223:180–186, 2012.

[58] A. Collauto, M. Zerbetto, M. Brustolon, A. Polimeno, A. Caneschi, and D. Gatteschi. Interpretation of cw-ESR spectra of p-methyl-thio-phenyl-nitronyl nitroxide in a nematic liquid crystalline phase. *Phys. Chem. Chem. Phys.*, 14:3200–3207, 2012.

[59] A. Collauto, M. Mannini, L. Sorace, A. Barbon, M. Brustolon, and D. Gatteschi. A slow relaxing species for molecular spin devices; EPR characterization of static and dynamic magnetic properties of a nitronyl nitroxide radical. *J. Mater. Chem.*, 22:22272–22281, 2012.

[60] A. Collauto, A. Barbon, M. Zerbetto, and M. Brustolon. An advanced approach to the evaluation of the spin-rotational term for a nitronyl nitroxide in fluid solution. *Mol. Phys.*, 111:2933–2941, 2013.

[61] M. J. Frisch, G. W. Trucks, H. B. Schlegel, G. E. Scuseria, M. A. Robb, J. R. Cheeseman, G. Scalmani, V. Barone, B. Mennucci, G. A. Petersson, H. Nakatsuji, M. Caricato, X. Li, H. P. Hratchian, A. F. Izmaylov, J. Bloino, G. Zheng, J. L. Sonnenberg, M. Hada, M. Ehara, K. Toyota, R. Fukuda, J. Hasegawa, M. Ishida, T. Nakajima, Y. Honda, O. Kitao, H. Nakai, T. Vreven, J. A. Montgomery, Jr., J. E. Peralta, F. Ogliaro, M. Bearpark, J. J. Heyd, E. Brothers, K. N. Kudin, V. N. Staroverov, R. Kobayashi, J. Normand, K. Raghavachari, A. Rendell, J. C. Burant, S. S. Iyengar, J. Tomasi, M. Cossi, N. Rega, J. M. Millam, M. Klene, J. E. Knox, J. B. Cross, V. Bakken, C. Adamo, J. Jaramillo, R. Gomperts, R. E. Stratmann, O. Yazyev, A. J. Austin, R. Cammi, C. Pomelli, J. W. Ochterski, R. L. Martin, K. Morokuma, V. G. Zakrzewski, G. A. Voth, P. Salvador, J. J. Dannenberg, S. Dapprich, A. D. Daniels, Ö. Farkas, J. B. Foresman, J. V. Ortiz, J. Cioslowski, and D. J. Fox. Gaussian09 Revision D.01, 2009. Gaussian Inc. Wallingford CT.

[62] F. Neese. The ORCA program system. *Wiley Interdisciplinary Reviews: Computational Molecular Science*, 2(1):73–78, 2012.

[63] L. B. Volodarsky. *Imidazoline Nitroxides: Volume I. Synthesis and Properties.* CRC Press, Boca Raton, 1988.

[64] E. I. Solomon, M. J. Baldwin, and M. D. Lowery. Electronic structures of active sites in copper proteins: Contributions to reactivity. *Chem. Rev.*, 92:521–542, 1992.

[65] E. I. Solomon, R. K. Szilagyi, S. D. George, and L. Basumallick. Electronic structures of metal sites in proteins and models: Contributions to function in blue copper proteins. *Chem. Rev.*, 104:419–458, 2004.

[66] R. Pogni, G. D. Lunga, and R. Basosi. Multi-microwave frequency EPR in the structural characterization of copper(II) dipeptide complexes. *J. Am. Chem. Soc.*, 115:1546–1550, 1993.

[67] G. D. Lunga, R. Pogni, and R. Basosi. Computer simulation of EPR spectra in the slow-motion region for copper complexes with nitrogen ligands. *J. Phys. Chem.*, 98:3937–3942, 1994.

[68] J. S. Hyde and W. Froncisz. The role of microwave frequnecy in EPR spectroscopy of copper complexes. *Ann. Rev. Biophys. Bioeng.*, 11:391–417, 1982.

[69] G. D. Lunga, M. Pezzato, M. C. Baratto, R. Pogni, and R. Basosi. A new program based on stochastic Liouville equation for the analysis of superhyperfine interaction in CW-ESR spectroscopy. *J. Magn. Reson.*, 167:71–77, 2003.

[70] R. Pogni, E. Busi, G. D. Lunga, and R. Basosi. Complex rotational dynamics of the Cu(II)-bleomycin system in mobile and viscous media. *Ann. N. Y. Acad. Sci.*, 879:276–279, 1999.

[71] J. S. Hyde, B. Bennet, E. D. Walter, G. L. Millhauser, J. W. Sidabras, and W. E. Antholine. EPR of Cu^{2+} prion protein constructs at 2 GHz using the $g_\perp$ region to characterize nitrogen ligation. *Biophys. J.*, 96:3354–3362, 2009.

[72] J. Köhler, A. C. J. Brouwer, E. J. J. Groenen, and J. Schmidt. Single molecule electron paramagnetic resonance spectroscopy: Hyperfine splitting owing to a single nucleus. *Science*, 268:1457–1460, 1995.

[73] F. Shi, Q. Zhang, P. Wang, H. Sun, J. Wang, X. Rong, M. Chen, C. Ju, F. Reinhard, H. Chen, J. Wrachtrup, J. Wang, and J. Du. Single-protein spin resonance spectroscopy under ambient conditions. *Science*, 347:1135–1138, 2015.

[74] C. More, J. P. Gayda, and P. Bertrand. Simulations of the g-strain broadening of low-spin hemoprotein EPR spectra based on the t_{2g} hole model. *J. Magn. Reson.*, 90:486–499, 1969.

[75] D. O. Hearshen, W. R. Hagen, R. H. Sands, H. J. Grande, H. L. Crespi, I. C. Gunsalus, and W. R. Dunham. An analysis of g strain in the EPR of two [2Fe-2S] ferredoxins. evidence for a protein rigidity model. *J. Magn. Reson.*, 69:440–459, 1986.

[76] Jr. J. S. Leigh and G. H. Reed. Electronic paramagnetic resonance studies in frozen

aqueous solutions. Elimination of freezing artifacts. *J. Phys. Chem.*, 75:1202–1204, 1971.

[77] R. B. Lauffer. Paramagnetic metal complexes as water relaxation agents for NMR imaging: theory and design. *Chem. Rev.*, 87:901–927, 1987.

[78] P. Caravan, J. J. Ellison, T. J. McMurry, and R. B. Lauffer. Gadolinium(III) chelates as MRI contrast agents: Structure, dynamics, and applications. *Chem. Rev.*, 99:2293–2352, 1999.

[79] M. Rogosnitzky and S. Branch. Gadolinium-based contrast agent toxicity: a review of known and proposed mechanisms. *BioMetals*, 29:365–376, 2016.

[80] H. Kim, G. H. Lee, and Y. Chang. Gadolinium as an MRI contrast agent. *Future Med. Chem.*, 10, 2018.

[81] H. Yagi, D. Banerjee, B. Graham, T. Huber, D. Goldfarb, and G. Otting. Gadolinium tagging for high-precision measurements of 6 nm distances in protein assemblies by EPR. *J. Am. Chem. Soc.*, 133:10418–10421, 2011.

[82] D. Goldfarb. Gd^{3+} spin labeling for distance measurements by pulse EPR spectroscopy. *Phys. Chem. Chem. Phys.*, 16:9685–9699, 2014.

[83] A. M. Raitsimring, C. Gunanathan, A. Potapov, I. Efremenko, J. M. L. Martin, D. Milstein, and D. Goldfarb. Gd^{3+} complexes as potential spin labels for high field pulsed EPR distance measurements. *J. Am. Chem. Soc.*, 129:14138–14139, 2007.

[84] A. Hudson and J. W. E. Lewis. Electron spin relaxation of ^8S ions in solution. *J. Chem. Soc. Faraday Trans.*, 66:1297–1301, 1970.

[85] A. Borel, É. Tóth, L. Helm, A. Jánossy, and A. E. Merbach. EPR on aqueous Gd^{3+} complexes and a new analysis method considering both line widths and shifts. *Phys. Chem. Chem. Phys.*, 2:1311–1317, 2000.

[86] S. Rast, A. Borel, L. Helm, E. Belorizky, P. H. Fries, and A. E. Merbach. EPR spectroscopy of MRI-related Gd(III) complexes: Simultaneous analysis of multiple frequency and temperature spectra, including static and transient crystal field effects. *J. Am. Chem. Soc.*, 123:2637–2644, 2001.

[87] A. Borel, H. Kang, C. Gateau, M. Mazzanti, R. B. Clarkson, and R. L. Belford. Variable temperature and EPR frequency study of two aqueous Gd(III) complexes with unprecedented sharp lines. *J. Phys. Chem. A*, 110:12434–12438, 2006.

[88] M. Benmelouka, J. V. Tol, A. Borel, S. Nellutla, M. Port, L. Helm, L. Brunel, and A. E. Merbach. Multiple-frequency and variable-temperature EPR study of gadolinioum(III) complexes with polyaminocarboxylates: Analysis and comparison of the magnetically dilute powder and the frozen-solution spectra. *Helv. Chim. Acta*, 92:2173–2185, 2009.

[89] S. Rast, P. H. Fries, E. Belorizky, A. Borel, L. Helm, and A. E. Merbach. A general approach to the electronic spin relaxation of Gd(III) complexes in solutions. Monte Carlo simulations beyond the Redfield limit. *J. Chem. Phys.*, 115:7554–7563, 2001.

[90] A. M. Raitsimring, A. V. Astashkin, O. G. Poluektov, and P. Caravan. High-field pulsed EPR and endor of Gd^{3+} complexes in glassy solutions. *Appl. Magn. Reson.*, 28:281–295, 2005.

[91] M. Azarkh and E. J. J. Groenen. Simulation of multi-frequency EPR spectra for a distribution of the zero-field splitting. *J. Magn. Reson.*, 255:106–113, 2015.

[92] A. Borel, L. Helm, and C. A. E. Daul. Hybrid ligand-field theory/quantum chemical calculation of the fine structure and ZFS in lanthanide(III) complexes. *Chem. Phys. Lett.*, 383:584–591, 2004.

[93] D. Ganyushin and F. Neese. First-principles calculations of zero-field splitting parameters. *J. Chem. Phys.*, 125:024103, 2006.

[94] C. Duboc, D. Ganyushin, K. Sivalingham, M. Collomb, and F. Neese. Systematic theoretical study of the zero-field splitting in coordination complexes of Mn(III). density functional theory versus multireference wave function approaches. *J. Phys. Chem. A*, 114:10750–10758, 2010.

[95] F. Senn, L. Helm, A. Borel, and C. A. Daul. Electronic fine structure calculation of $[Gd(DOTA)(H_2O)]^-$ using LF-DFT: The zero field splitting. *C. R. Chimie*, 15:250–254, 2012.

[96] D. Thonon, V. Jacques, and J. F. Desreux. A gadolinium triacetic monoamide DOTA derivative with a methanethiosulfonate anchor group. Relaxivity properties and conjugation with albumin and thiolated particles. *Contrast Media Mol. Imaging*, 2:24–34, 2007.

[97] L. Garbuio, K. Zimmermann, D. Häussinger, and M. Yulikov. Gd(III) complexes for electron-electron dipolar spectroscopy: Effects of deuteration, pH and zero field splitting. *J. Magn. Reson.*, 259:163–173, 2015.

[98] D. T. Edwards, Z. Ma, T. J. Meade, D. Goldfarb, and M. S. Sherwin. Extending the distance range accessed with continuous wave EPR with Gd^{3+} spin probes at high magnetic fields. *Phys. Chem. Chem. Phys.*, 15:11313–11326, 2013.

[99] G. Binsch. The direct method for calculating high-resolution nuclear magnetic resonance spectra. *Mol. Phys.*, 15:469–478, 1968.

[100] G. Binsch. Unified theory of exchange effects on nuclear magnetic resonance line shapes. *J. Am. Chem. Soc.*, 91:1304–1309, 1969.

Appendix A

MATRIX ELEMENTS OF THE SLE MATRIX IN THE K-SYMMETRIZED BASIS

A.1 Introduction

Simulating a slow-motion CW EPR spectrum using the stochastic Liouville equation (SLE) ultimately amounts to solving the following matrix equation:

$$I(\omega) = \langle v|\,[-(\mathrm{i}\hat{\hat{H}} + \omega\hat{\hat{1}} + \hat{\hat{\Gamma}})]^{-1}\,|v\rangle \tag{A.1}$$

where $v = \hat{S}_x P_{\mathrm{eq}}^{1/2}$ is the "starting vector", $\hat{\hat{H}}$ is the Hamiltonian superoperator, ω is the frequency of the incoming B_1 microwave magnetic field, $\hat{\hat{\Gamma}}$ is the rotational diffusion superoperator, and $\hat{\hat{1}}$ is the identity superoperator. All operators and vectors in equation A.1 are in Liouville space. The SLE matrix is:

$$-(\mathrm{i}\hat{\hat{H}} + \omega\hat{\hat{1}} + \hat{\hat{\Gamma}}). \tag{A.2}$$

In order to solve equation A.1, the SLE matrix of equation A.2 must either be diagonalized or inverted, but the matrix is quite large for most systems of interest. This is the bottleneck for simulating slow-motion EPR spectra. The Lanczos tridiagonalization method decreases the cost of this calculation immensely, but the algorithm requires that the SLE matrix be complex symmetric.

In the direct product basis introduced in chapter 2, the matrix representation of $\hat{\hat{H}}$ is Hermitian and $\hat{\hat{\Gamma}}$ is real symmetric in the absence of an orienting potential. The matrix $\omega\hat{\hat{1}}$ is diagonal and so has no effect on the symmetry of the SLE matrix. However, the matrix $-\mathrm{i}\hat{\hat{H}}$ is anti-Hermitian and, upon addition of $\hat{\hat{\Gamma}}$, the SLE matrix is neither Hermitian nor symmetric.

A.1.1 K-symmetrized basis

The K-symmetrized basis transforms $\hat{\hat{H}}$ into a real symmetric matrix, which causes the SLE matrix to become a complex symmetric matrix that is suitable for the Lanczos algorithm. The K-symmetrized basis states are related to the Wigner $|LMK\rangle$ basis states via the following transformation [27, 21, 22, 37, 45, 46]:

$$|LMKj^K\rangle = \frac{\sqrt{j^K}}{\sqrt{2(1+\delta_{K,0})}}[|LMK\rangle + j^K(-1)^{L+K}|LM\bar{K}\rangle] \tag{A.3}$$

where K is restricted to be nonnegative in the K-symmetrized basis, $\bar{K}$ is the negative of K, and $j^K = \pm1$ according to the following conditions:

$$\begin{aligned} K = 0 &\rightarrow j^K = (-1)^L \\ K > 0 &\rightarrow j^K = \pm1. \end{aligned} \tag{A.4}$$

For each $|LMK\rangle$ with $K > 0$, there are two different states corresponding to the positive and negative j^K values:

$$\begin{aligned} |LMK+\rangle &= \frac{1}{\sqrt{2}}[|LMK\rangle + (-1)^{L+K}|LM\bar{K}\rangle] \\ |LMK-\rangle &= \frac{\mathrm{i}}{\sqrt{2}}[|LMK\rangle - (-1)^{L+K}|LM\bar{K}\rangle] \end{aligned} \tag{A.5}$$

A.1.2 Hamiltonian elements in the $|LMK\rangle$ basis

The elements of the Hamiltonian in the new K-symmetrized basis can be calculated in terms of the matrix elements in the original $|LMK\rangle$ basis. The Hamiltonian consists of "spin blocks" formed as the sum of products of the rank-0, rank-1 (usually negligible), and rank-2 components of $\langle L_1M_1K_1|\hat{\hat{H}}|L_2M_2K_2\rangle$ with the rank-0, rank-1, and rank-2 rotational basis operators (RBOs) respectively. In general, each "spin block" is

$$\begin{aligned}\langle L_1 M_1 K_1|\, H\,|L_2 M_2 K_2\rangle &= (-1)^{K_1-M_1}\sqrt{(2L_1+1)(2L_2+1)} \\ &\times \Bigg[Q^0_{\Delta M,\Delta K}\begin{pmatrix} L_1 & 0 & L_2 \\ -M_1 & M_1-M_2 & M_2\end{pmatrix}\begin{pmatrix} L_1 & 0 & L_2 \\ -K_1 & K_1-K_2 & K_2\end{pmatrix} \\ &+ Q^2_{\Delta M,\Delta K}\begin{pmatrix} L_1 & 2 & L_2 \\ -M_1 & M_1-M_2 & M_2\end{pmatrix}\begin{pmatrix} L_1 & 2 & L_2 \\ -K_1 & K_1-K_2 & K_2\end{pmatrix}\Bigg] \\ &= (-1)^{K_1-M_1}\sqrt{(2L_1+1)(2L_2+1)} \\ &\times \sum_l (-1)^l Q^l_{\Delta M,\Delta K}\begin{pmatrix} L_1 & l & L_2 \\ -M_1 & M_1-M_2 & M_2\end{pmatrix}\begin{pmatrix} L_1 & l & L_2 \\ -K_1 & K_1-K_2 & K_2\end{pmatrix}\end{aligned} \tag{A.6}$$

where $\Delta M = M_1 - M_2$ and $\Delta K = K_1 - K_2$. Note that the Hamiltonian H and the RBOs Q are operators, but the hats are omitted here to simplify notation. For the sake of brevity, from here on out the following abbreviations will be used:

$$\begin{aligned} N_L &= \sqrt{(2L_1+1)(2L_2+1)} \\ N_{M_l} &= (-1)^l \begin{pmatrix} L_1 & l & L_2 \\ -M_1 & M_1-M_2 & M_2\end{pmatrix} \\ Q^l_{K_1-K_2} &= Q^l_{\Delta M,\Delta K}. \end{aligned} \tag{A.7}$$

The shorthand notation for Q is used because the $\Delta M = M_1 - M_2$ index is invariant to the K and j^K values.

A.2 K-symmetrized Hamiltonian matrix elements

In general, the K-symmetrized Hamiltonian matrix elements are

$$\begin{aligned}\langle L_1 M_1 K_1 j_1^K|\, H\,|L_2 M_2 K_2 j_2^K\rangle &= \frac{(\sqrt{j_1^K})^\star\sqrt{j_2^K}}{2\sqrt{(1+\delta_{K_1,0})(1+\delta_{K_2,0})}} \\ &\times \big[\, \langle L_1 M_1 K_1|\, H\,|L_2 M_2 K_2\rangle \\ &+ j_2^K(-1)^{L_2+K_2}\langle L_1 M_1 K_1|\, H\,|L_2 M_2 \bar{K}_2\rangle \\ &+ j_1^K(-1)^{L_1+K_1}\langle L_1 M_1 \bar{K}_1|\, H\,|L_2 M_2 K_2\rangle \\ &+ j_1^K j_2^K(-1)^{L_1+L_2+K_1+K_2}\langle L_1 M_1 \bar{K}_1|\, H\,|L_2 M_2 \bar{K}_2\rangle\,\big]\end{aligned} \tag{A.8}$$

where the asterisk denotes the complex conjugate of $\sqrt{j_1^K}$ because j_1^K is in the bra. However, j_1^K itself is always real because it can only assume the values $+1$ and -1.

The right-hand-side of equation A.8 is derived by substituting equation A.3 into the the basis states. It is important to keep in mind that K is restricted to always be nonnegative, so negative values of K are represented by $\bar{K}$. With this in mind, the K-symmetrized matrix elements can be expanded in terms of the original basis as follows:

$$
\begin{aligned}
\langle L_1 M_1 K_1 j_1^K | \, H \, | L_2 M_2 K_2 j_2^K \rangle = {} & \frac{(\sqrt{j_1^K})^\star \sqrt{j_2^K}}{2\sqrt{(1+\delta_{K_1,0})(1+\delta_{K_2,0})}} N_L \\
& \times \sum_l N_{M_l} \Bigg[(-1)^{K_1-M_1} \begin{pmatrix} L_1 & l & L_2 \\ -K_1 & K_1-K_2 & K_2 \end{pmatrix} Q^l_{K_1-K_2} \\
& + j_2^K (-1)^{L_2+K_2+K_1-M_1} \begin{pmatrix} L_1 & l & L_2 \\ -K_1 & K_1-\bar{K}_2 & \bar{K}_2 \end{pmatrix} Q^l_{K_1-\bar{K}_2} \\
& + j_1^K (-1)^{L_1-M_1} \begin{pmatrix} L_1 & l & L_2 \\ -\bar{K}_1 & \bar{K}_1-K_2 & K_2 \end{pmatrix} Q^l_{\bar{K}_1-K_2} \\
& + j_1^K j_2^K (-1)^{L_1+L_2+K_2-M_1} \begin{pmatrix} L_1 & l & L_2 \\ -\bar{K}_1 & \bar{K}_1-\bar{K}_2 & \bar{K}_2 \end{pmatrix} Q^l_{\bar{K}_1-\bar{K}_2} \Bigg].
\end{aligned}
\tag{A.9}
$$

Equation A.9 can be rewritten in terms of strictly nonnegative K as

$$
\begin{aligned}
\langle L_1 M_1 K_1 j_1^K | \, H \, | L_2 M_2 K_2 j_2^K \rangle = {} & \frac{(\sqrt{j_1^K})^\star \sqrt{j_2^K}}{2\sqrt{(1+\delta_{K_1,0})(1+\delta_{K_2,0})}} N_L \\
& \times \sum_l N_{M_l} \Bigg[(-1)^{K_1-M_1} \begin{pmatrix} L_1 & l & L_2 \\ -K_1 & K_1-K_2 & K_2 \end{pmatrix} Q^l_{K_1-K_2} \\
& + j_2^K (-1)^{L_2+K_2+K_1-M_1} \begin{pmatrix} L_1 & l & L_2 \\ -K_1 & K_1+K_2 & -K_2 \end{pmatrix} Q^l_{K_1+K_2} \\
& + j_1^K (-1)^{L_1-M_1} \begin{pmatrix} L_1 & l & L_2 \\ K_1 & -K_1-K_2 & K_2 \end{pmatrix} Q^l_{-K_1-K_2} \\
& + j_1^K j_2^K (-1)^{L_1+L_2+K_2-M_1} \begin{pmatrix} L_1 & l & L_2 \\ K_1 & -K_1+K_2 & -K_2 \end{pmatrix} Q^l_{-K_1+K_2} \Bigg].
\end{aligned}
\tag{A.10}
$$

Using the following property of $3j$-symbols:

$$\begin{pmatrix} j_1 & j_2 & j_3 \\ m_1 & m_2 & m_3 \end{pmatrix} = (-1)^{j_1+j_2+j_3} \begin{pmatrix} j_1 & j_2 & j_3 \\ -m_1 & -m_2 & -m_3 \end{pmatrix} \tag{A.11}$$

and using the fact that l is always even, equation A.10 can be condensed into:

$$\begin{aligned} \langle L_1 M_1 K_1 j_1^K | \, H \, | L_2 M_2 K_2 j_2^K \rangle = & \frac{(\sqrt{j_1^K})^\star \sqrt{j_2^K}}{2\sqrt{(1+\delta_{K_1,0})(1+\delta_{K_2,0})}} N_L \\ & \times \sum_l N_{M_l} \Bigg[\left((-1)^{K_1-M_1} Q^l_{K_1-K_2} + j_1^K j_2^K (-1)^{K_2-M_1} Q^l_{-K_1+K_2} \right) \\ & \times \begin{pmatrix} L_1 & l & L_2 \\ -K_1 & K_1-K_2 & K_2 \end{pmatrix} \\ & + \left(j_1^K (-1)^{L_2-M_1} Q^l_{-K_1-K_2} + j_2^K (-1)^{L_2+K_1+K_2-M_1} Q^l_{K_1+K_2} \right) \\ & \times \begin{pmatrix} L_1 & l & L_2 \\ -K_1 & K_1+K_2 & -K_2 \end{pmatrix} \Bigg]. \end{aligned} \tag{A.12}$$

A.2.1 Rank-0 components

For the purpose of clarity in computer implementation, it is convenient to differentiate between the rank-0, rank-1, and rank-2 terms in the sum over RBO ranks. Each term can be computed separately and then summed to give the overall Hamiltonian, so there is no problem in doing this. Due to the triangle rule, the rank-0 term can have nonzero $3j$-symbols only if the following conditions are satisfied:

$$\begin{aligned} L_1 &= L_2 = L \\ M_1 &= M_2 = M \\ K_1 &= K_2 = K. \end{aligned} \tag{A.13}$$

Given the constraints of equations A.13, equation A.12 simplifies to:

$$\begin{aligned}\langle LMKj_1^K|\, H\, |LMKj_2^K\rangle^{(0)} =& \frac{1}{2(1+\delta_{K,0})} N_L N_{M_0} \\ &\times \Bigg[(-1)^{K-M} Q_0^0 \big(1\ +\ j_1^K j_2^K\big) \begin{pmatrix} L & 0 & L \\ -K & 0 & K \end{pmatrix} \\ &+ (-1)^{L-M} \big(j_1^K Q_{-2K}^0\ +\ j_2^K Q_{2K}^0\big) \begin{pmatrix} L & 0 & L \\ -K & 2K & -K \end{pmatrix} \Bigg].\end{aligned} \tag{A.14}$$

Rank-0 elements: $K = 0$

Due to the constraints of equation A.13, the second term in the square brackets of equation A.14 can have a nonzero $3j$-symbol only if $K = 0$, in which case equation A.14 becomes

$$\begin{aligned}\langle LM0j^K|\, H\, |LM0j^K\rangle =& \frac{1}{2} N_L N_{M_0} Q_0^0 \Big[(-1)^M\ +\ (-1)^{L+M} j^K \Big] \begin{pmatrix} L & 0 & L \\ 0 & 0 & 0 \end{pmatrix} \\ =& \frac{1}{2\sqrt{2L+1}} N_L N_{M_0} Q_0^0 \Big[(-1)^{L-M}\ +\ (-1)^M j^K \Big]\end{aligned} \tag{A.15}$$

where the fact that $j_1^K = j_2^K = j^K$ has been used because the parity of L is the same in both the bra and ket states. The following property of $3j$-symbols was used to arrive at the final result of equation A.15:

$$\begin{pmatrix} j & 0 & j \\ -m & 0 & m \end{pmatrix} = \begin{pmatrix} j & j & 0 \\ m & -m & 0 \end{pmatrix} = (-1)^{j-m} \frac{1}{\sqrt{2j+1}}. \tag{A.16}$$

Regardless of the parity of L, equation A.15 simplifies to

$$\begin{aligned}\langle LM0j^K|\, H\, |LM0j^K\rangle =& N_L N_{M_0} (-1)^M Q_0^0 \begin{pmatrix} L & 0 & L \\ 0 & 0 & 0 \end{pmatrix} \\ =& \frac{1}{\sqrt{2L+1}} N_L N_{M_0} (-1)^{L+M} Q_0^0.\end{aligned} \tag{A.17}$$

Rank-0 elements: $K > 0$

If K is nonzero, then equation A.14 becomes

$$\begin{aligned} \langle LMKj_1^K | \, H \, | LMKj_2^K \rangle &= \frac{1}{2} N_L N_{M_0} (-1)^{K-M} Q_0^0 \big(1 + j_1^K j_2^K\big) \begin{pmatrix} L & 0 & L \\ -K & 0 & K \end{pmatrix} \\ &= \frac{1}{2\sqrt{2L+1}} N_L N_{M_0} (-1)^{L-M} Q_0^0 \big(1 + j_1^K j_2^K\big) \end{aligned} \tag{A.18}$$

where property A.16 has been used because of the structure of the $3j$-symbol in equation A.18. There are now four subcases, each corresponding to a particular combination of j_1^K and j_2^K values. The two antisymmetric cases in which $j_1^K = -j_2^K$ simply result in zero elements of the Hamiltonian:

$$\langle LMK+ | \, H \, | LMK- \rangle = \langle LMK- | \, H \, | LMK+ \rangle = 0. \tag{A.19}$$

The two symmetric elements in which $j_1^K = j_2^K$ are

$$\begin{aligned} \langle LMK+ | \, H \, | LMK+ \rangle &= \langle LMK- | \, H \, | LMK- \rangle \\ &= N_L N_{M_0} (-1)^{K-M} Q_0^0 \begin{pmatrix} L & 0 & L \\ -K & 0 & K \end{pmatrix} \\ &= \frac{1}{\sqrt{2L+1}} N_L N_{M_0} (-1)^{L-M} Q_0^0. \end{aligned} \tag{A.20}$$

If $K = 0$ is substituted into equation A.20, then equation A.20 becomes identical to equation A.18. Therefore, equation A.20 can be used to compute all of the nonzero rank-0 elements of the Hamiltonian in the K-symmetrized basis.

A.2.2 Rank-1 components

Rank-1 components do not contribute to any spin Hamiltonian terms and therefore explicit equations for the rank-1 terms of the Hamiltonian matrix elements in the K-symmetrized basis will not be derived here.

A.2.3 Rank-2 components

According to equation A.12, the rank-2 components of the spin Hamiltonian matrix elements are

$$
\begin{aligned}
\langle L_1 M_1 K_1 j_1^K | \, H \, | L_2 M_2 K_2 j_2^K \rangle^{(2)} = {} & \frac{(\sqrt{j_1^K})^\star \sqrt{j_2^K}}{2\sqrt{(1+\delta_{K_1,0})(1+\delta_{K_2,0})}} N_L N_{M_2} \\
& \times \Bigg[\bigg((-1)^{K_1-M_1} Q^2_{K_1-K_2} \, + \, j_1^K j_2^K (-1)^{K_2-M_1} Q^2_{-K_1+K_2} \bigg) \\
& \times \begin{pmatrix} L_1 & 2 & L_2 \\ -K_1 & K_1-K_2 & K_2 \end{pmatrix} \\
& + \bigg(j_1^K (-1)^{L_2-M_1} Q^2_{-K_1-K_2} \, + \, j_2^K (-1)^{L_2+K_1+K_2-M_1} Q^2_{K_1+K_2} \bigg) \\
& \times \begin{pmatrix} L_1 & 2 & L_2 \\ -K_1 & K_1+K_2 & -K_2 \end{pmatrix} \Bigg].
\end{aligned}
\tag{A.21}
$$

In this case, the triangle rule ensures that the $3j$-symbols can be nonzero only if $|K_1 - K_2| \leq 2$ is true. Because of the triangle rule, the only possible nonzero elements of the rank-2 components are those in which K_1 and K_2 adhere to

$$K_1 - 2 \leq K_2 \leq K_1 + 2 \tag{A.22}$$

within the bounds of allowed K_2 values of course (i.e. K_2 cannot be less than zero or greater than L). Within the constraint of equation A.22, the $3j$-symbol of the first term in equation A.21 is ensured to always be nonzero. However, recalling that the K-values are constrained to be nonnegative, the $3j$-symbol of the second term in equation A.21 can be nonzero only under the following circumstance:

$$K_1 + K_2 \leq 2. \tag{A.23}$$

The constraint of equation A.23 can only be satisfied under the following conditions:

$$\begin{aligned} K_1 &= 0 \text{ and } K_2 = 0 \\ K_1 &= 0 \text{ and } K_2 = 1 \\ K_1 &= 0 \text{ and } K_2 = 2 \\ K_1 &= 1 \text{ and } K_2 = 0 \\ K_1 &= 1 \text{ and } K_2 = 1 \\ K_1 &= 2 \text{ and } K_2 = 0 \end{aligned} \tag{A.24}$$

Assuming that one of the conditions of equation A.24 is met, then equation A.21 may be simplified according to each condition.

Rank-2 elements: $K_1 = K_2 = 0$

The simplest case is when $K_1 = K_2 = 0$, which results in

$$\begin{aligned} \langle L_1 M_1 0 j_1^K |\, H \,| L_2 M_2 0 j_2^K \rangle = {} & \frac{(\sqrt{j_1^K})^\star \sqrt{j_2^K}}{4} N_L N_{M_2} \\ & \times Q_0^2 \left[(-1)^{-M_1} \big(1 + j_1^K j_2^K\big) + (-1)^{L_2 - M_1} \big(j_1^K + j_2^K\big) \right] \begin{pmatrix} L_1 & 2 & L_2 \\ 0 & 0 & 0 \end{pmatrix}. \end{aligned} \tag{A.25}$$

The $K_1 = K_2 = 0$ case in equation A.25 is further divided into four subcases corresponding to the four possible combinations of the parities of L_1 and L_2: two symmetric cases and two antisymmetric cases. The matrix elements for the symmetric case in which both L_1 and L_2 are even are

$$\langle L_1 M_1 0+ |\, H \,| L_2 M_2 0+ \rangle = N_L N_{M_2} (-1)^{-M_1} Q_0^2 \begin{pmatrix} L_1 & 2 & L_2 \\ 0 & 0 & 0 \end{pmatrix}. \tag{A.26}$$

For the symmetric case in which both L_1 and L_2 are odd, the matrix elements are

$$\langle L_1 M_1 0- |\, H \,| L_2 M_2 0- \rangle = \frac{1}{2} N_L N_{M_2} Q_0^2 \left[(-1)^{-M_1} - (-1)^{L_2 - M_1} \right] \begin{pmatrix} L_1 & 2 & L_2 \\ 0 & 0 & 0 \end{pmatrix}. \tag{A.27}$$

From equation A.25, it is easy to see that both of the antisymmetric cases in which the parities of L_1 and L_2 differ are simply zero:

$$\langle L_1 M_1 0+|\, H\, |L_2 M_2 0-\rangle = \langle L_1 M_1 0-|\, H\, |L_2 M_2 0+\rangle = 0. \tag{A.28}$$

According to equations A.26, A.27, and A.28, all of the rank-2 terms for which $K_1 = K_2 = 0$ are real.

Rank-2 elements: $K_1 = 0\ ,\ K_2 > 0$

There are two cases in which only one of the two K-values is zero. In the case where $K_1 = 0$ and $K_2 > 0$, the matrix elements are

$$\begin{aligned}\langle L_1 M_1 0 j_1^K|\, H\, |L_2 M_2 K_2 j_2^K\rangle = {} & \frac{(\sqrt{j_1^K})^{\star}\sqrt{j_2^K}}{2\sqrt{2}} N_L N_{M_2} \\ & \times \Bigg[Q^2_{K_2}\Big\{ j_1^K j_2^K (-1)^{K_2-M_1} + j_2^K (-1)^{L_1+K_2-M_1} \Big\} \\ & + Q^2_{-K_2}\Big\{ (-1)^{-M_1} + j_1^K (-1)^{L_1-M_1} \Big\} \Bigg] \begin{pmatrix} L_1 & 2 & L_2 \\ 0 & -K_2 & K_2 \end{pmatrix}\end{aligned} \tag{A.29}$$

where the $3j$-symbol property of equation A.11 was used to derive the result of equation A.29. Recall that due to the condition in equation A.22, all rank-2 terms are necessarily zero if $K_2 > 2$ is true. Assuming $K_2 < 0$, equation A.29 can be divided into four subcases corresponding to the combinations of the parity of L_1 and the j_2^K values.

In the symmetric case where L_1 is even and $j_2^K = 1$, the rank-2 elements are

$$\langle L_1 M_1 0+|\, H\, |L_2 M_2 K_2+\rangle = \frac{1}{\sqrt{2}} N_L N_{M_2} \left[(-1)^{K_2-M_1} Q^2_{K_2} + (-1)^{-M_1} Q^2_{-K_2} \right] \begin{pmatrix} L_1 & 2 & L_2 \\ 0 & -K_2 & K_2 \end{pmatrix}. \tag{A.30}$$

For the other symmetric case in which L_1 is odd and $j_2^K = -1$, the elements are:

$$\begin{aligned}\langle L_1 M_1 0- |\, H \,| L_2 M_2 K_2 - \rangle = {} & \frac{1}{2\sqrt{2}} N_L N_{M_2} \Bigg[Q^2_{K_2} \Big\{ (-1)^{K_2 - M_1} - (-1)^{L_1 + K_2 - M_1} \Big\} \\ & + Q^2_{-K_2} \Big\{ (-1)^{-M_1} - (-1)^{L_1 - M_1} \Big\} \Bigg] \begin{pmatrix} L_1 & 2 & L_2 \\ 0 & -K_2 & K_2 \end{pmatrix} .\end{aligned} \tag{A.31}$$

For the antisymmetric case in which when L_1 is even and $j^K_2 = -1$, the elements are

$$\langle L_1 M_1 0+ |\, H \,| L_2 M_2 K_2 - \rangle = \frac{\mathrm{i}}{\sqrt{2}} N_L N_{M_2} \Big[-(-1)^{K_2 - M_1} Q^2_{K_2} + (-1)^{-M_1} Q^2_{-K_2} \Big] \begin{pmatrix} L_1 & 2 & L_2 \\ 0 & -K_2 & K_2 \end{pmatrix} . \tag{A.32}$$

For the other antisymmetric case, in which L_1 is odd and $j^K_2 = 1$, the matrix elements are

$$\begin{aligned}\langle L_1 M_1 0- |\, H \,| L_2 M_2 K_2 + \rangle = {} & -\frac{\mathrm{i}}{2\sqrt{2}} N_L N_{M_2} \Bigg[Q^2_{K_2} \Big\{ -(-1)^{K_2 - M_1} + (-1)^{L_1 + K_2 - M_1} \Big\} \\ & + Q^2_{-K_2} \Big\{ (-1)^{-M_1} - (-1)^{L_1 - M_1} \Big\} \Bigg] \begin{pmatrix} L_1 & 2 & L_2 \\ 0 & -K_2 & K_2 \end{pmatrix} .\end{aligned} \tag{A.33}$$

Rank-2 elements: $K_1 > 0$, $K_2 = 0$

The case in which $K_1 > 0$ and $K_2 = 0$ is different from the above case in which $K_1 = 0$ and $K_2 > 0$ because of the complex conjugate of j^K_1. In general, the rank-2 elements for the case in which $K_1 > 0$ and $K_2 = 0$ are

$$\begin{aligned}\langle L_1 M_1 K_1 j^K_1 |\, H \,| L_2 M_2 0 j^K_2 \rangle = {} & \frac{(\sqrt{j^K_1})^\star \sqrt{j^K_2}}{2\sqrt{2}} N_L N_{M_2} \\ & \times \Bigg[Q^2_{K_1} \Big\{ (-1)^{K_1 - M_1} + j^K_2 (-1)^{L_2 + K_1 - M_1} \Big\} \\ & + Q^2_{-K_1} \Big\{ j^K_1 j^K_2 (-1)^{-M_1} + j^K_1 (-1)^{L_2 - M_1} \Big\} \Bigg] \begin{pmatrix} L_1 & 2 & L_2 \\ -K_1 & K_1 & 0 \end{pmatrix} .\end{aligned} \tag{A.34}$$

Of course, the matrix element in equation A.34 is always zero if $K_1 > 2$, otherwise there are once again four subcases of equation A.34. Assuming $K_1 < 2$, the elements for the symmetric case in which L_2 is even and $j_1^K = 1$ are

$$\langle L_1 M_1 K_1 + | \, H \, | L_2 M_2 0 + \rangle = \frac{1}{\sqrt{2}} N_L N_{M_2} \left[(-1)^{K_1 - M_1} Q^2_{K_1} \; + \; (-1)^{-M_1} Q^2_{-K_1} \right] \begin{pmatrix} L_1 & 2 & L_2 \\ -K_1 & K_1 & 0 \end{pmatrix} . \tag{A.35}$$

For the other symmetric case, in which L_2 is odd and $j_1^K = -1$, the matrix elements are

$$\begin{aligned} \langle L_1 M_1 K_1 - | \, H \, | L_2 M_2 0 - \rangle = \frac{1}{2\sqrt{2}} N_L N_{M_2} \Bigg[& Q^2_{K_1} \Big\{ (-1)^{K_1 - M_1} \; - \; (-1)^{L_2 + K_1 - M_1} \Big\} \\ & + Q^2_{-K_1} \Big\{ (-1)^{-M_1} \; - \; (-1)^{L_2 - M_1} \Big\} \Bigg] \begin{pmatrix} L_1 & 2 & L_2 \\ -K_1 & K_1 & 0 \end{pmatrix} . \end{aligned} \tag{A.36}$$

The matrix elements for the antisymmetric case corresponding to L_2 odd and $j_1^K = 1$ are

$$\begin{aligned} \langle L_1 M_1 K_1 + | \, H \, | L_2 M_2 0 - \rangle = \frac{\mathrm{i}}{2\sqrt{2}} N_L N_{M_2} \Bigg[& Q^2_{K_1} \Bigg\{ (-1)^{K_1 - M_1} \; - \; (-1)^{L_2 + K_1 - M_1} \Bigg\} \\ & + Q^2_{-K_1} \Bigg\{ - (-1)^{-M_1} \; + \; (-1)^{L_2 - M_1} \Bigg\} \Bigg] \begin{pmatrix} L_1 & 2 & L_2 \\ -K_1 & K_1 & 0 \end{pmatrix} . \end{aligned} \tag{A.37}$$

Finally, the elements for the other antisymmetric case corresponding to L_2 even and $j_1^K = -1$ are

$$\langle L_1 M_1 K_1 - | \, H \, | L_2 M_2 0 + \rangle = -\frac{\mathrm{i}}{\sqrt{2}} N_L N_{M_2} \left[(-1)^{K_1 - M_1} Q^2_{K_1} - (-1)^{-M_1} Q^2_{-K_1} \right] \begin{pmatrix} L_1 & 2 & L_2 \\ -K_1 & K_1 & 0 \end{pmatrix} . \tag{A.38}$$

Rank-2 elements: $K_1 > 0 \; , \; K_2 > 0$

The final case for equation A.21 is that in which both $K_1 > 0$ and $K_2 > 0$ is true. The expression for the rank-2 terms of the Hamiltonian elements in this case is

$$\begin{aligned}\langle L_1 M_1 K_1 j_1^K |\, H \,| L_2 M_2 K_2 j_2^K \rangle = & \frac{(\sqrt{j_1^K})^\star \sqrt{j_2^K}}{2} N_L N_{M_2} \\ & \times \Bigg[\Bigg((-1)^{K_1 - M_1} Q^2_{K_1 - K_2} + j_1^K j_2^K (-1)^{K_2 - M_1} Q^2_{-K_1 + K_2} \Bigg) \\ & \times \begin{pmatrix} L_1 & 2 & L_2 \\ -K_1 & K_1 - K_2 & K_2 \end{pmatrix} \\ & + \Bigg(j_1^K (-1)^{L_2 - M_1} Q^2_{-K_1 - K_2} + j_2^K (-1)^{L_2 + K_1 + K_2 - M_1} Q^2_{K_1 + K_2} \Bigg) \\ & \times \begin{pmatrix} L_1 & 2 & L_2 \\ -K_1 & K_1 + K_2 & -K_2 \end{pmatrix} \Bigg] .\end{aligned} \tag{A.39}$$

Given the nonzero condition of equation A.22, the only possible condition that can yield a nonzero $3j$-symbol for the second term in square brackets in equation A.39 is when $K_1 = K_2 = 1$ is true. Assuming this condition is met, then the matrix elements for $K_1 > 0$ and $K_2 > 0$ are

$$\begin{aligned}\langle L_1 M_1 1 j_1^K |\, H \,| L_2 M_2 1 j_2^K \rangle = & \frac{(\sqrt{j_1^K})^\star \sqrt{j_2^K}}{2} N_L N_{M_2} \Bigg[(-1)^{1 - M_1} Q^2_0 \big(1 + j_1^K j_2^K\big) \begin{pmatrix} L_1 & 2 & L_2 \\ -1 & 0 & 1 \end{pmatrix} \\ & + (-1)^{L_2 - M_1} \big(j_1^K Q^2_{-2} + j_2^K Q^2_2 \big) \begin{pmatrix} L_1 & 2 & L_2 \\ -1 & 2 & -1 \end{pmatrix} \Bigg] .\end{aligned} \tag{A.40}$$

Again, there are four subcases corresponding to the four possible combinations of j_1^K and j_2^K values. In this case, however, the parities of L_1 and L_2 are no longer correlated with the j_1^K and j_2^K values. For the symmetric case in which $j_1^K = j_2^K = 1$, the matrix elements are

$$\begin{aligned}\langle L_1 M_1 1+ |\, H \,| L_2 M_2 1+ \rangle = & \frac{1}{2} N_L N_{M_2} \Bigg[2(-1)^{1 - M_1} Q^2_0 \begin{pmatrix} L_1 & 2 & L_2 \\ -1 & 0 & 1 \end{pmatrix} \\ & + (-1)^{L_2 - M_1} \big(Q^2_{-2} + Q^2_2 \big) \begin{pmatrix} L_1 & 2 & L_2 \\ -1 & 2 & -1 \end{pmatrix} \Bigg] .\end{aligned} \tag{A.41}$$

For the other symmetric case, in which $j_1^K = j_2^K = -1$, the matrix elements are

$$\begin{aligned}\langle L_1 M_1 1- | \, H \, | L_2 M_2 1- \rangle = {} & \frac{1}{2} N_L N_{M_2} \Bigg[2(-1)^{1-M_1} Q_0^2 \begin{pmatrix} L_1 & 2 & L_2 \\ -1 & 0 & 1 \end{pmatrix} \\ & - (-1)^{L_2-M_1} \big(Q_{-2}^2 + Q_2^2 \big) \begin{pmatrix} L_1 & 2 & L_2 \\ -1 & 2 & -1 \end{pmatrix} \Bigg]. \end{aligned} \tag{A.42}$$

For the antisymmetric case, in which $j_1^K = 1$ and $j_2^K = -1$, the elements are

$$\langle L_1 M_1 1+ | \, H \, | L_2 M_2 1- \rangle = \frac{\mathrm{i}}{2} N_L N_{M_2} \left[(-1)^{L_2-M_1} \big(Q_{-2}^2 - Q_2^2 \big) \begin{pmatrix} L_1 & 2 & L_2 \\ -1 & 2 & -1 \end{pmatrix} \right]. \tag{A.43}$$

And finally, the matrix elements for the other antisymmetric case, in which $j_1^K = -1$ and $j_2^K = 1$, are

$$\langle L_1 M_1 1- | \, H \, | L_2 M_2 1+ \rangle = -\frac{\mathrm{i}}{2} N_L N_{M_2} \left[(-1)^{L_2-M_1} \big(- Q_{-2}^2 + Q_2^2 \big) \begin{pmatrix} L_1 & 2 & L_2 \\ -1 & 2 & -1 \end{pmatrix} \right]. \tag{A.44}$$

Finally, there is the case for equation A.39 in which $K_1 + K_2 > 2$. When this condition is true, the second term in square brackets in equation A.39 is necessarily zero, giving the following general expression for the rank-2 component of the Hamiltonian matrix elements elements:

$$\begin{aligned}\langle L_1 M_1 K_1 j_1^K | \, H \, | L_2 M_2 K_2 j_2^K \rangle = {} & \frac{(\sqrt{j_1^K})^\star \sqrt{j_2^K}}{2} N_L N_{M_2} \\ & \times \Bigg[\bigg((-1)^{K_1-M_1} Q_{K_1-K_2}^2 + j_1^K j_2^K (-1)^{K_2-M_1} Q_{-K_1+K_2}^2 \bigg) \\ & \times \begin{pmatrix} L_1 & 2 & L_2 \\ -K_1 & K_1 - K_2 & K_2 \end{pmatrix} \Bigg]. \end{aligned} \tag{A.45}$$

Once again, there are four subcases, each corresponding to one of the possible combinations of j^K values. Both symmetric cases ($j_1^K = j_2^K = 1$ and $j_1^K = j_2^K = -1$) are equivalent and have the following matrix elements:

$$\begin{aligned}\langle L_1 M_1 K_1 + |\, H \,| L_2 M_2 K_2 + \rangle &= \langle L_1 M_1 K_1 - |\, H \,| L_2 M_2 K_2 - \rangle \\ &= \frac{1}{2} N_L N_{M_2} \Bigg[\Bigg((-1)^{K_1 - M_1} Q^2_{K_1 - K_2} \,+\, (-1)^{K_2 - M_1} Q^2_{-K_1 + K_2} \Bigg) \\ &\times \begin{pmatrix} L_1 & 2 & L_2 \\ -K_1 & K_1 - K_2 & K_2 \end{pmatrix} \Bigg]. \end{aligned} \tag{A.46}$$

For the antisymmetric case, in which $j_1^K = 1$ and $j_2^K = -1$, the matrix elements are

$$\begin{aligned}\langle L_1 M_1 K_1 + |\, H \,| L_2 M_2 K_2 - \rangle &= \frac{\mathrm{i}}{2} N_L N_{M_2} \\ &\times \Bigg[\Bigg((-1)^{K_1 - M_1} Q^2_{K_1 - K_2} \,-\, (-1)^{K_2 - M_1} Q^2_{-K_1 + K_2} \Bigg) \\ &\times \begin{pmatrix} L_1 & 2 & L_2 \\ -K_1 & K_1 - K_2 & K_2 \end{pmatrix} \Bigg]. \end{aligned} \tag{A.47}$$

Finally, the other antisymmetric case, in which $j_1^K = -1$ and $j_2^K = 1$, is

$$\begin{aligned}\langle L_1 M_1 K_1 - |\, H \,| L_2 M_2 K_2 + \rangle &= -\frac{\mathrm{i}}{2} N_L N_{M_2} \\ &\times \Bigg[\Bigg((-1)^{K_1 - M_1} Q^2_{K_1 - K_2} \,-\, (-1)^{K_2 - M_1} Q^2_{-K_1 + K_2} \Bigg) \\ &\times \begin{pmatrix} L_1 & 2 & L_2 \\ -K_1 & K_1 - K_2 & K_2 \end{pmatrix} \Bigg] \end{aligned} \tag{A.48}$$

which is simply the complex conjugate of the antisymmetric case in equation A.47.

A.3 K-symmetrized starting vector matrix elements

The general expression matrix elements of the spatial component of the starting vector from equation 2.79 in the K-symmetrized basis are

$$\langle LMKj^K|P_{\mathrm{eq}}^{1/2}\rangle = \frac{(\sqrt{j^K})^*}{\sqrt{2(1+\delta_{K,0})}}\left[\langle LMK|P_{\mathrm{eq}}^{1/2}\rangle + j^K(-1)^{L+K}\,\langle LM\bar{K}|P_{\mathrm{eq}}^{1/2}\rangle\right] \tag{A.49}$$

where P_{eq} is the potential-dependent equilibrium orientational distribution introduced in chapter 2. Substituting the matrix element expressions from equation 2.79 into equation A.49 above gives the elements of the starting vector in the K-symmetrized basis:

$$\frac{\sqrt{2L+1}(\sqrt{j^K})^*}{4\pi\sqrt{1+\delta_{K,0}}}\int \mathrm{d}\boldsymbol{\Omega}\,\left[(D^L_{MK})^* + j^K(-1)^{L+K}\left(D^L_{M\bar{K}}\right)^*\right]P_{\mathrm{eq}}^{1/2}. \tag{A.50}$$

In general, there are no analytical solutions to equation A.50 and therefore the integrals must be determined numerically.

Appendix B

THE LANCZOS METHOD

B.1 Introduction

The Lanczos algorithm has been well-reported by Schneider and Freed [21, 22]. This appendix is meant to be a supplement to the original work on the Lanczos algorithm, with the hope that certain details are made clearer herein.

The simulation of slow-motion EPR spectra from the Stochastic Liouville Equation (SLE) requires the solution of the following matrix equation:

$$I(\omega) = \langle v| \left[-\mathrm{i}H + \mathit{\Gamma} - \mathrm{i}\omega 1\right]^{-1} |v\rangle \tag{B.1}$$

where $I(\omega)$ is the frequency-dependent spectral lineshape function of equation 2.39, v is the starting vector, ω is the angular frequency of the incoming microwave B_1 magnetic field, H is the matrix representation of the Hamiltonian superoperator, $\mathit{\Gamma}$ is the matrix representation of the rotational diffusion superoperator, and 1 is the identity matrix. H, $\mathit{\Gamma}$, and 1 are all Liouville-space superoperators. The SLE matrix is

$$-(\mathrm{i}H + \mathit{\Gamma} + \mathrm{i}\omega 1) = A - \mathrm{i}\omega 1 \tag{B.2}$$

where the portion of the SLE matrix that is independent of the incoming B_1 microwave field has been represented as $A = -(\mathrm{i}H + \mathit{\Gamma})$ for convenience in focusing on the important aspects of the Lanczos algorithm. According to appendix A, the SLE matrix may always be chosen to be complex symmetric by representing the matrix in the K-symmetrized basis. In general, A is also sparse and has a well-defined block structure. All of these properties make the Lanczos algorithm quite suitable for finding the eigenvalues and eigenvectors of A in a quick and efficient manner. Essentially, the Lanczos algorithm is a numerical method that solves the matrix equation

$$\begin{aligned} v^{\mathrm{T}} A^{-1} v &= v^{\mathrm{T}} y \\ A y &= v \end{aligned} \tag{B.3}$$

which replaces the computationally intensive problem of matrix inversion or diagonalization with the easier problem of determining y by solving a system of linear equations.

B.2 The Lanczos algorithm

B.2.1 Krylov subspaces

If A is complex symmetric, as it may always be chosen to be (in the absence of a general orienting potential), the Lanczos algorithm computes a complex symmetric tridiagonal matrix T that is similar to A, given A itself and some starting vector v as input. Suppose that $A \in \mathbb{C}^{N\times N}$, and that $v \in \mathbb{C}^{N\times 1}$ is normalized. A set of Krylov vectors $\{k_m\} \in \mathbb{C}^{N\times 1}$ $(1 \le m \le N)$ may then be constructed via the repeated transformation of v by A:

$$\begin{aligned} k_1 &= v \\ k_2 &= A k_1 = A v \\ k_3 &= A k_2 = A^2 v \\ &\vdots \\ k_m &= A k_{m-1} = A^{m-1} v. \end{aligned} \tag{B.4}$$

These Krylov vectors span an m-dimensional Krylov subspace. The dimension of the Krylov space grows as subsequent Krylov vectors are added to the set $\{k_m\}$. It is usually the case that the dimension of the Krylov subspace that is sufficient to accurately approximate y is much lower than the dimension of the eigenspace of A. In other words:

$$m \ll N. \tag{B.5}$$

The property of Krylov methods in equation B.5 greatly reduces the effective size of the SLE matrix problem.

B.2.2 Gram-Schmidt orthogonalization

The Lanczos algorithm creates an orthonormal basis of Lanczos vectors $\{q_m\}$ for the Krylov subspace by performing a Gram-Schmidt orthogonalization on each additional Krylov vector that is introduced to the set $\{k_m\}$. This is done by expressing each new q_m as a proper linear combination of all previous orthonormal Krylov basis vectors as well as the new Krylov vector formed upon the last transformation by A. In general, the newest member of the set $\{q_m\}$ can be expressed as

$$q_{m+1} = c_{m+1} A q_m + \sum_{i=1}^{m} c_i q_i \tag{B.6}$$

where the coefficients c are determined by constraining the set $\{q_m\}$ to be orthonormal.

B.2.3 Constructing the Lanczos vectors

This section examines the steps of the Lanczos algorithm in some detail. The first Lanczos vector in the set $\{q_m\}$ is simply the normalized starting vector:

$$q_1 = k_1 = v. \tag{B.7}$$

By constraining the next Lanczos vector to be both orthogonal to q_1 and normalized, the next Lanczos vector is constructed by transforming q_1 with A:

$$q_2 = c_2^{(2)} A q_1 + c_1^{(2)} q_1 = (c_2^{(2)} A + c_1^{(2)} 1) q_1 \tag{B.8}$$

where 1 is the identity matrix. The coefficients $c^{(2)}$ are determined by requiring q_2 to be orthonormal to q_1. The (2)-superscript denotes that these coefficients apply to the construction of q_2 only. The coefficient $c_1^{(2)}$ can be solved for by multiplying equation B.8 by q_1^{T} on the left. Because q_1 and q_2 are orthogonal, the first coefficient is

$$c_1^{(2)} = -c_2^{(2)} q_1^{\mathrm{T}} A q_1. \tag{B.9}$$

Substituting equation B.9 back into equation B.8 gives q_2:

$$q_2 = c_2^{(2)} (A - q_1^{\mathrm{T}} A q_1 1) q_1. \tag{B.10}$$

The second coefficient $c_2^{(2)}$ can now be solved for by multiplying equation B.8 by q_2^{T} on the left:

$$c_2^{(2)} = (q_2^{\mathrm{T}} A q_1)^{-1} = (q_1^{\mathrm{T}} A q_2)^{-1} = \|(A - q_1^{\mathrm{T}} A q_1 1) q_1\|^{-1}. \tag{B.11}$$

The second equality in equation B.11 holds due to the complex symmetric structure of A and the third equality comes from the fact that $c_2^{(2)}$ must be such that q_2 is normalized. Note that although $c_2^{(2)} = (q_1^{\mathrm{T}} A q_2)^{-1}$ is true, the coefficient cannot be determined in that manner because it would require prior knowledge of q_2, which is unknown. Therefore, $c_2^{(2)}$ must be calculated using the third equality in equation B.11.

From hereon, for the sake of brevity and to coincide with the notation of Schneider and Freed [21, 22], the following notation will be used:

$$\begin{aligned} \alpha_1 &= q_1^{\mathrm{T}} A q_1 \\ \beta_1 &= q_1^{\mathrm{T}} A q_2 = (c_2^{(2)})^{-1}. \end{aligned} \tag{B.12}$$

Note that α and β are scalars. Using the notation of equation B.12, q_2 of equation B.10 can be expressed more compactly as

$$\beta_1 q_2 = (A - \alpha_1 1) q_1. \tag{B.13}$$

The next member of the Lanczos basis can now be constructed as a linear combination of the previous two vectors and the vector resulting from the transformation of q_2 by A:

$$q_3 = c_3^{(3)} A q_2 + c_2^{(3)} q_2 + c_1^{(3)} q_1. \tag{B.14}$$

The coefficients $c_1^{(3)}$ and $c_2^{(3)}$ are determined by the left multiplication of equation B.14 by the transposes of q_1 and q_2 in turn:

$$\begin{aligned} c_1^{(3)} &= -\, c_3^{(3)} q_1^{\mathrm{T}} A q_2 \\ c_2^{(3)} &= -\, c_3^{(3)} q_2^{\mathrm{T}} A q_2. \end{aligned} \tag{B.15}$$

Once again, q_3 can be determined in terms of $c_3^{(3)}$ by substitution of $c_1^{(3)}$ and $c_2^{(3)}$ into equation B.14:

$$q_3 = c_3^{(3)} \left[\, (A - q_2^{\mathrm{T}} A q_2 1) q_2 - (q_1^{\mathrm{T}} A q_2) q_1 \,\right]. \tag{B.16}$$

The third coefficient of the third Lanczos vector $c_3^{(3)}$ can be determined by left multiplication of equation B.14 by q_3^{T} along with the fact that $c_3^{(3)}$ must be such that q_3 is normalized:

$$c_3^{(3)} = (q_2^{\mathrm{T}} A q_3)^{-1} = \|(A - q_2^{\mathrm{T}} A q_2 1) q_2 - (q_1^{\mathrm{T}} A q_2) q_1\|^{-1}. \tag{B.17}$$

Using the compact notation of equation B.12, equation B.16 can be rewritten as

$$\beta_2 q_3 = (A - \alpha_2 1) q_2 - \beta_1 q_1 \tag{B.18}$$

where the following notation has been used:

$$\begin{aligned} \alpha_2 &= q_2^{\mathrm{T}} A q_2 \\ \beta_2 &= q_2^{\mathrm{T}} A q_3 = c_3^{(3)^{-1}}. \end{aligned} \tag{B.19}$$

B.2.4 Three-term recursion relation

The next step is to construct the fourth Krylov basis vector, which will illustrate one of the reasons that the Lanczos algorithm is so powerful for solving the SLE lineshape function of matrix equation B.1 - the following three-term recursion relation:

$$\beta_m q_{m+1} = (A - \alpha_m 1) q_m - \beta_{m-1} q_{m-1}. \tag{B.20}$$

Once again, the construction of q_4 begins by expressing the vector as a linear combination of the vector Aq_3 and all of the previous Lanczos vectors:

$$q_4 = c_4^{(4)} A q_3 + c_3^{(4)} q_3 + c_2^{(4)} q_2 + c_1^{(4)} q_1. \tag{B.21}$$

As before, the first three coefficients in equation B.21 can be determined by left-multiplication with the transposes of each previous Lanczos vector:

$$\begin{aligned} c_1^{(4)} &= -\,c_4^{(4)} q_1^{\mathrm{T}} A q_3 \\ c_2^{(4)} &= -\,c_4^{(4)} q_2^{\mathrm{T}} A q_3 \\ c_3^{(4)} &= -\,c_4^{(4)} q_3^{\mathrm{T}} A q_3. \end{aligned} \tag{B.22}$$

Substitution of these coefficients into equation B.21 yields

$$q_4 = c_4^{(4)} \big[\, (A - q_3^{\mathrm{T}} A q_3 1) q_3 - (q_2^{\mathrm{T}} A q_3) q_2 - (q_1^{\mathrm{T}} A q_3) q_1 \,\big]. \tag{B.23}$$

In analogy to equations B.12 and B.19, α_3 and β_3 are expressed as

$$\begin{aligned} \alpha_3 &= q_3^{\mathrm{T}} A q_3 \\ \beta_3 &= q_3^{\mathrm{T}} A q_4 = c_4^{(3)^{-1}}. \end{aligned} \tag{B.24}$$

But what about the $q_1^{\mathrm{T}} A q_3$ factor in the q_1 term of equation B.27? Examining this factor by expanding $q_1^{\mathrm{T}} A$ according to equation B.13 gives

$$q_1^{\mathrm{T}} A = \beta_1 q_2^{\mathrm{T}} + \alpha_1 q_1^{\mathrm{T}} \tag{B.25}$$

where the fact that A is symmetric ($A = A^{\mathrm{T}}$) has been used. Substitution of equation B.25 into the factor $q_1^{\mathrm{T}} A q_3$ yields

$$q_1^{\mathrm{T}} A q_3 = \beta_1 q_2^{\mathrm{T}} q_3 + \alpha_1 q_1^{\mathrm{T}} q_3 = 0. \tag{B.26}$$

Therefore, equation B.21 reduces to:

$$q_4 = c_4^{(4)} \big[\, (A - \alpha_3 1) q_3 - \beta_2 q_2 \,\big]. \tag{B.27}$$

Equation B.27 is a three-term recursion relationship. Due to this recursion relation, only information from the previous two iterations of the Lanczos algorithm are required in order to construct the next vector. For example, in the case of equation B.27, only q_2 and q_3 are needed to calculate q_4. The fact that the general recursion relation in equation B.20 is true may be verified for yourself by following the steps herein.

Following the same process as above, the coefficient $c_4^{(4)}$ may now be solved for:

$$c_4^{(4)} = (q_3^{\mathrm{T}} A q_4)^{-1} = \|(A - \alpha_3 1) q_3 - \beta_2 q_2\|^{-1}. \tag{B.28}$$

Finally, q_4 may be constructed using the definition of $\beta_3 = c_4^{(4)^{-1}}$:

$$\beta_3 q_4 = (A - \alpha_3 1) q_3 - \beta_2 q_2. \tag{B.29}$$

Equation B.29 has the exact same form as the general three-term recursion relation of equation B.20.

B.2.5 Construction of the tridiagonal matrix

Once the elements of the complex symmetric matrix A are known and a starting vector v has been chosen, a set of Lanczos vectors $\{q_m\}$ can be constructed until the Krylov space spanned by those vectors is sufficient to solve the lineshape function in equation B.1 given a specified convergence criterion.

Now assume that the set $\{q_m\}$ consists of m Lanczos vectors with $m < N$, where N is the dimension of A. Then after the final iteration of the three-term recursion relation in equation B.20, these m Lanczos vectors form the columns of a transformation matrix $Q_m \in \mathbb{C}^{N\times m}$ that tridiagonalizes A into a complex symmetric tridiagonal matrix $T_m \in \mathbb{C}^{m\times m}$ via

$$T_m = Q_m^{\mathrm{T}} A Q_m. \tag{B.30}$$

The diagonal elements of T_m are simply the α coefficients that were determined during the Lanczos iterations and the off-diagonal elements are the β coefficients. The structure of T_m is as such:

$$\begin{bmatrix} \alpha_1 & \beta_1 & 0 & \dots & 0 & 0 \\ \beta_1 & \alpha_2 & \beta_2 & 0 & \vdots & 0 \\ 0 & \beta_2 & \alpha_3 & \ddots & 0 & \vdots \\ \vdots & 0 & \ddots & \ddots & \beta_{m-2} & 0 \\ 0 & \dots & 0 & \beta_{m-2} & \alpha_{m-1} & \beta_{m-1} \\ 0 & 0 & \dots & 0 & \beta_{m-1} & \alpha_m \end{bmatrix} \tag{B.31}$$

The transformation matrix Q_m is not unitary because A is not Hermitian, but Q_m does satisfy the following relations:

$$\begin{aligned} I &= Q_m^{\mathrm{T}} Q_m \\ I &= Q_m^{-1} Q_m^{\mathrm{T}\text{-}} \\ Q_m &= Q_m^{\mathrm{T}\text{-}} \\ Q_m^{\mathrm{T}} &= Q_m^{-1} \end{aligned} \tag{B.32}$$

where $Q_m^{\mathrm{T}\text{-}}$ is the inverse of the transpose of Q_m. Therefore, the spectral lineshape function of equation B.1 may be expressed as

$$\begin{aligned} I(\omega) &= v^{\mathrm{T}} Q_m Q_m^{\mathrm{T}} [A - \mathrm{i}\omega 1]^{-1} Q_m Q_m^{\mathrm{T}} v \\ &= (v^{\mathrm{T}} Q_m)[Q_m^{\mathrm{T}} A Q_m - \mathrm{i}\omega 1_m]^{-1} (Q_m^{\mathrm{T}} v) \\ &= v_m'^{\mathrm{T}} [T_m - \mathrm{i}\omega 1_m]^{-1} v_m' \end{aligned} \tag{B.33}$$

where v_m' is the vector formed by the transformation of v by Q_m^{T}. Using property B.32 of Q_m, it can be proven that equation B.33 is true:

$$\begin{aligned} Q_m^{\mathrm{T}} [A - \mathrm{i}\omega 1]^{-1} Q_m &= [T_m - \mathrm{i}\omega 1_m]^{-1} \\ Q_m^{-1} [A - \mathrm{i}\omega 1] Q_m^{\mathrm{T}\text{-}} &= [T_m - \mathrm{i}\omega 1_m] \\ Q_m^{\mathrm{T}} [A - \mathrm{i}\omega 1] Q_m &= [T_m - \mathrm{i}\omega 1_m] \\ [T_m - \mathrm{i}\omega 1_m] &= [T_m - \mathrm{i}\omega 1_m]. \end{aligned} \tag{B.34}$$

Equation B.33 shows that the size of the problem has been greatly reduced, provided that $m \ll N$, which is one of the benefits of the Lanczos algorithm. At this point, T_m could be diagonalized quite quickly because T_m is tridiagonal and symmetric. This diagonalization would then give the matrix Λ, which contains the eigenvalues of T_m on its diagonal:

$$U^{\mathrm{T}} T U = \Lambda. \tag{B.35}$$

The m-subscript in equation B.35 has been omitted because U and Λ are always $m \times m$ matrices formed upon convergence of the Lanczos algorithm after m iterations. Because U

also shares property B.32, the same reasoning used in equation B.34 can be used to express equation B.33 in terms of Λ:

$$\begin{aligned} I(\omega) &= v'^{\mathrm{T}} U U^{\mathrm{T}} [T - \mathrm{i}\omega 1]^{-1} U U^{\mathrm{T}} v' \\ &= (v'^{\mathrm{T}} U)[U^{\mathrm{T}} T U - \mathrm{i}\omega 1]^{-1} (U^{\mathrm{T}} v') \\ &= u^{\mathrm{T}} [\Lambda - \mathrm{i}\omega 1]^{-1} u \end{aligned} \tag{B.36}$$

where $u^{\mathrm{T}} = U^{\mathrm{T}} v'$ is the m-dimensional transformed starting vector. The matrix in square brackets on the last line in equation B.36 is diagonal and can be expressed as [99, 100]:

$$D = \Lambda - \mathrm{i}\omega 1. \tag{B.37}$$

The problem of computing the spectral lineshape function over a range of ω by matrix inversion is now trivial because D is diagonal. The resulting matrix equation after the Lanczos algorithm is

$$I(\omega) = u^{\mathrm{T}} D u \tag{B.38}$$

which, for each ω, is simply the following sum of scalars:

$$I(\omega) = \sum_{i=1}^{m} \frac{u_i^2}{\Lambda_i - \mathrm{i}\omega}. \tag{B.39}$$

The simulated lineshape can finally be obtained by plotting the imaginary part of $I(\omega)$ over the range of ω values.